UNIVERSITEIT·STELLENBOSCH·UNIVERSITY
jou kennisvennoot • your knowledge partner

Attitude Determination and Control System of a Nanosatellite

by

Johannes Schoonwinkel

Thesis presented at the University of Stellenbosch in partial fulfilment of the requirements for the degree of

Master of Science in Engineering

Department of Electrical Engineering
University of Stellenbosch
Private Bag X1, 7602 Matieland, South Africa

Study leader: Prof W.H. Steyn

October 2007

Declaration

I, the undersigned, hereby declare that the work contained in this thesis is my own original work and that I have not previously in its entirety or in part submitted it at any university for a degree.

Signature: .....
J. Schoonwinkel

Date: .....

Abstract

The aim of this project was to design and test a partial attitude determination and control system for a nanosatellite. The reaction wheel system was designed and tested as an actuator for the nanosatellite. This reaction wheel system consists of four reaction wheels mounted in a tetrahedral formation. A rate sensor system was also designed and its viability for this space application was examined. The rate sensor system consists of 3 orthogonally mounted planes, each with three rate sensors mounted on it. Hardware-in-the-loop tests were used along with an air bearing experimentational setup, which created near frictionless circumstances, to prove the effectiveness of the designed reaction wheel setup. The results following from this project were the following: The reaction wheel system proved to be an adequate actuator for this nanosatellite application and the rate sensor system which was analysed proved to be inadequate for a nanosatellite application.

Samevatting

Die doel van hierdie projek was om ’n gedeeltelike orientasie beheer stelsel vir ’n nanosatelliet te ontwerp en te toets. Die reaksiewiel stelsel is ontwerp en getoets as ’n aktueerder vir die nanosatelliet. Die reaksiewiel stelsel bestaan uit vier reaksiewiele wat in ’n tetrahedrale formasie monteer is. ’n Rotasie tempo sensor sisteem is ook ontwerp en die bruikbaarheid daarvan vir hierdie ruimtetoepassing is ondersoek. Die rotasie tempo sensor sisteem bestaan uit drie ortogonaal gemonteerde vlakke wat elk drie rotasie tempo sensore bevat. Hardeware-in-die-lus toetse is saam met ’n luglaer eksperimentele opstelling gebruik, wat semi-wrywingslose toestande skep, om die effektiwiteit van die reaksiewiel stelsel te bewys. Die resultate wat uit hierdie projek gevolg het was die volgende: Die reaksiewiel stelsel sal as ’n baie effektiewe aktueerder vir hierdie nanosatelliet toepassing gebruik kan word en die rotasie tempo sensor stelsel wat analiseer is, is ongeskik bevind vir die nanosatelliet toepassing.

Acknowledgements

I would like to thank the following people:

- Prof Steyn for your guidance and excellent advice throughout the project
- Emile Rossouw, Izak Marais, Leo Herselman, Keith Brown, Helgard van Rensburg, Gerrit Kruger, Henk Marais, Carlo Botha, John Wilson, Steven Kriel, Niel Muller, Christiaan Brand and Hendrik Meiring for your inputs and help when it was needed most
- Suné de Klerk for your wonderful support and encouragement
- My family for bringing me this far

Contents

List of Figures

List of Tables

List of Abbreviations and Symbols

Abbreviations

ADCS	Attitude Determination and Control System
ARW	Angle random walk
AtoD	Analog to digital converter
AVAR	Allan variance
BLDC	Brushless direct current
CAN	Controller area network
CMOS	Complementary metal-oxide-semiconductor
COG	Centre of geometry
COM	Centre of mass
DC	Direct current
DCM	Direct Cosine Matrix
DtoA	Digital to analog converter
ECEF	Earth Centered Earth Fixed
ECI	Earth Centered Inertial
ESL	Electronic Systems Laboratory

HIL	Hardware-in-the-Loop
I^2C	Inter integrated circuit
JTAG	Joint test action group
LEO	Low Earth Orbit
MEMS	Microelectromechanical systems
MOI	Moment of inertia
MOSFET	metal oxide semiconductor field effect transistor
NORAD	North American Aerospace Defence Command
PCA	Programmable counter array
PCB	Printed circuit board
PD	Proportional derivative
PI	Proportional integral
PID	Proportional integral derivative
PSD	Power spectral density
PWM	Pulse width modulation
RC	Resistor capacitor
RMS	Root mean square
RRW	Rate random walk
SPI	Serial peripheral interface bus
SUNSAT	Stellenbosch University satellite
TLE	Two-line Elements
TVAR	Time variance
UART	Universal asynchronous receiver/transmiter

Symbols

Chapter 2:

$\mathbf{q_e}$	Quaternion error
$\mathbf{q_c}$	Commanded quaternion
$\mathbf{q}$	Current attitude quaternion
$\mathbf{u}$	Control input torque vector
$\boldsymbol{\omega}_{\mathbf{B}}^{\mathbf{I}}$	Inertially referenced body angular velocity vector
$\boldsymbol{\omega}_{\mathbf{B}}^{\mathbf{O}}$	Orbit referenced body angular velocity vector
$\mathbf{I}$	Inertia matrix
U_{max_i}	Maximum control torque possible for axis i
K_P	Proportional gain
K_D	Derivative gain
ζ	Damping ratio
ω_n	Linear control bandwidth
L_i	Attitue-error feedback saturation limit for axis i
a_i	Maximum control acceleration about axis i
$\omega_{i\,\max}$	Maximum specified slew rate about axis i
h_x	Angular momentum about x axis
h_y	Angular momentum about y axis
h_z	Angular momentum about z axis
h_i	Angular momentum about the rotation axis of wheel i
γ	The complimentary angle of the angle between the vertical axis and the angular momentum vector of reaction wheels 2, 3 and 4

η A quater of the angle between the angular momentum vectors of reaction wheels 2 and 3, 3 and 4 or 4 and 2 as seen from above

Chapter 3:

m Predicted mass of the satellite

R Predicted radius of the satellite

h Predicted height of the satellite

$N_{command}$ Torque command sent to the BLDC controller

ω_{err} Angular velocity error

K_1 Integrator gain 1 (equal to K_P)

K_2 Integrator gain 1 (equal to $K_P a$)

a Position of the zero for wheel speed controller

$\mathbf{B}$ Magnetic field of the earth

$\mathbf{H}$ Reaction wheel angular momentum vector

$\mathbf{M}$ Torque vector exerted by magnetic torquers

k Magnetic controller gain

Chapter 4:

t_{PULSE} BLDC controller Tacho output pulse width

R_{PUL} Resistor value determining the Tacho output pulse width

C_{PUL} Capacitor value determining the Tacho output pulse width

R_{sense} BLDC controller current sensing resistor

I_{peak} Peak current delivered to the BLDC motor

P_R Maximum power dissipated in the R_{sense} resistor

$\mathbf{A}$ Rate sensor (orthogonality) decoupling matrix

Y_{cr} Average true roll angle of rotation (for four tests)

Y_{cp}	Average true pitch angle of rotation (for four tests)
Y_{cy}	Average true yaw angle of rotation (for four tests)
Y_{mr}	Average rate sensor measured roll angle of rotation (for four tests)
Y_{mp}	Average rate sensor measured pitch angle of rotation (for four tests)
Y_{my}	Average rate sensor measured yaw angle of rotation (for four tests)
$\sigma_{\bar{x}}^2(T)$	Time variance
$\sigma_A^2(T)$	Allan variance
$y(k)$	average value of a block (bin) of data
$x(k)$	Data points spaced by T_s
T_s	Rate sensor sample time
T	the bin size (in seconds) into which the data is devided
n	the bin size (in number of samples) into which the data is devided
N	Number of complete bins which fit into the data
$S(f)$	Power spectral density
$S_{ARW}(f)$	Angle random walk power spectral density
$\sigma_{ARW}(T)$	Angle random walk Allan Deviation
$S_{RRW}(f)$	Rate random walk power spectral density
$\sigma_{RRW}(T)$	Rate random walk Allan Deviation

Chapter 5:

G_{OL}	Current loop (open loop) transfer function
K_{OL}	Current loop (open loop) gain
T_s	Speed loop sample time
G_{PI}	PI speed loop controller transfer function

Chapter 6:

T_g	Gravity gradient disturbance torque
μ	Gravity constant of the earth
R	Orbit radius (from centre of earth)
θ	Maximum deviation of the z-axis from the local vertical
y	Rate sensor output
b	Rate sensor bias from random walk process
ω_b	RRW component noise
$\mathbf{Q}$	RRW covariance matrix
v	ARW component noise
$\mathbf{R}$	ARW covariance matrix
ω	True angular rate

Chapter 7:

P_O	Solar cell array output power
$P_{intensity}$	Power intensity of sunlight
$A_{solarpanel}$	Solar panel area
P_{sa}	Power generated by solar array during sunlight
P_e	Power requirement during eclipse
P_d	Power requirement during sunlight
T_e	Eclipse time of orbit
T_d	Sunlit time of orbit
X_e	Efficiency of solar panel supply path
X_d	Efficiency of battery supply path

Appendix A:

P_{max}	Maximum power consumed by motor
$V_{a_{max}}$	Maximum armature voltage
$I_{a_{max}}$	Maximum armature current
I_{NL}	No load current of motor
N_{const}	Torque constant of motor
N_{max}	Maximum torque requirement
$V_{Ra_{max}}$	Maximum voltage over armature resistance
$\Omega_{terminal}$	Terminal resistance of motor
$E_{0_{max}}$	Maximum back EMF
ω_{const}	Speed constant of motor
ω_{max}	Maximum rotational speed requirement

Chapter 1

Introduction

The attitude determination and control system (ADCS) is the subsystem of a satellite which is responsible for stabilizing and orientating the satellite in the desired direction. It takes external disturbance torques into account and compensates accordingly which means that the satellite will be 3-axis stabilized. This is done by using a set of different sensors to measure the attitude of the satellite with respect to a fixed coordinate system. The orientation of the satellite is then changed or maintained by using the actuators of the satellite.

1.1 Aims and Objectives

The aim of this masters project is to design and test a subset of the full ADCS, sensors and actuators, of a nanosatellite. The challenge in designing such a subsystem for a nanosatellite is that all parts of the system must be as small, light and power efficient as possible. The first aim of the project was to simulate the reaction wheel system along with the model of a nanosatellite. The second aim was to design and build a tetrahedral reaction wheel system for a nanosatellite which will enable 3-axis stabilization of the satellite. This included designing the driving electronics for the four reaction wheels, the four rotors and the mounting structure. The third aim of the project was to design and build a rate sensor system for a nanosatellite. The final aim was to test these subsystems on an air bearing in a hardware-in-the-loop (HIL) simulation. This means that a part of the simulation (in this case the reaction wheel) was replaced with the actual physical component to test the hardware as if

it was in the real system. A control system was also designed to prove that the reaction wheel system can be used along with the rate sensor system, in an air bearing setup, to control the attitude of the setup along one free axis of rotation.

1.1.1 Mission Objectives

The nanosatellite to be designed will be launched together with a mother satellite, which will most probably be an earth observation satellite. The nanosatellite will have a CMOS camera sensor as main payload and will be used to take images and video data of the mother satellite. These images will be used to monitor the mother satellite and provide visual images for the following possible processes or error scenarios of the mother satellite: The deployment of solar panels or a boom with a tipmass, satellite detumbling or external mechanical problems. This nanosatellite will also once more demonstrate formation flying, 3-axis stabilized flight and orbit rendezvous of two satellites with different drag characteristics. One of the main objectives of this mission is also to educate masters students at the University of Stellenbosch in the field of Space Engineering.

1.2 Background

In the past much research has been done on the subsystems of microsatellites at the University of Stellenbosch. The Electrical and Electronical department hosts the Electronic Systems Laboratory (ESL) where South Africa's first satellite, SUNSAT-1 (Stellenbosch University Satellite) was built from 1991 to 1999. Currently masters students at Stellenbosch University are doing research on various subsystems of a nanosatellite. This project will also contribute to the bigger aim of developing a nanosatellite at the University of Stellenbosch.

The reason why the project of building a nanosatellite is done in an university environment, is due to the fact that it can be done in a relatively short period of time and the costs associated with developing and launching a nanosatellite are relatively small. Builing a nanosatellite provides the extra challenge of minimizing all the subsystems of a satellite while providing the same functionality.

Previous reaction wheels were built at the ESL by Laurentius Joubert (for Sunsat) and Xandri Farr. These reaction wheels are much too big and too heavy for a nanosatellite, therefore a smaller reaction wheel system was needed which will meet the torque, weight and size requirements of a nanosatellite. Therefore this project focuses exclusively on the ADCS of a nanosatellite. A tetrahedral reaction wheel system was therefore designed to make the total system even more compact.

Redundancy is an important part of any space mission. In this project it is therefore also necessary to make provision for the possibility of a reaction wheel failure in space. An extra reaction wheel is therefore added to the system to provide continual 3-axis controllability even when one of the four reaction wheels fails. The tetrahedral form of the reaction wheel structure was chosen, because in this configuration the nett angular momentum is zero when all four wheels are rotating at the same angular velocity. This makes the control of the system simpler due to the fact that the reaction wheels will be used at a constant offset wheel speed.

1.3 Document Layout

In Chapter 2 the theory behind the design decisions will be explained. The control algorithms which were tested in simulation will be explained. Chapter 3 will discuss the simulation of the nanosatellite ADCS. First the reaction wheel will be simulated together with the satellite dynamics and then the implementation of momentum dumping will be discussed. The design decisions made will be motivated in Chapter 4. Some of the detail design of the reaction wheel system and the rate sensor system will be discussed in this chapter. The simulation and practical results will be shown in Chapter 5. These results include the following topics: The HIL simulation, the experimental air bearing setup and the rate sensor system. Lastly in Chapter 6 the conclusions of this project will be presented and recommendations for further studies will be given.

Chapter 2

Theory

Design decisions can only be made on the basis of the underlying theory. This chapter describes the theory which was needed to complete this project.

2.1 Space Mission Geometry

When designing an ADCS for a nanosatellite it is important to know where and how this satellite will be used. This includes the specific orbit the satellite will be launched into, for example the inclination and altitude of the orbit. The specifications set for the ADCS will be based on the background theory of space mission geometry which will be explained in this section.

2.1.1 Coordinate Systems

The roll, pitch and yaw angles (Figure 2.1) can be used to define the transition between the spacecraft-fixed coordinate system (Figure 2.2) and the orbit reference frame (Figure 2.3). The roll axis is the rotation around the spacecraft direction of velocity. The pitch axis is the rotation around the negative orbit normal direction. Lastly the yaw-axis is the rotation around the nadir direction.

The spacecraft-fixed coordinate system is used as the common reference frame for all on-board sensors and actuators and it is fixed to the center of mass (COM) of the satellite. Its axis will be chosen such that certain features of the satellite are orientated along one axis of the spacecraft-fixed coordinate system. Since the nanosatellite will have a camera as main payload, it would

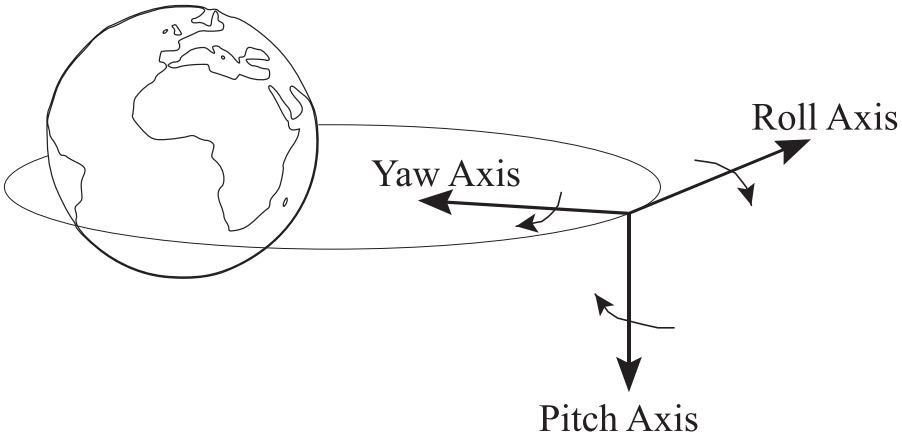

Figure 2.1: Roll Pitch Yaw

be natural for one axis to be in the direction of the camera lens. Along with the other two axes it should constitute a Cartesian coordinate system.

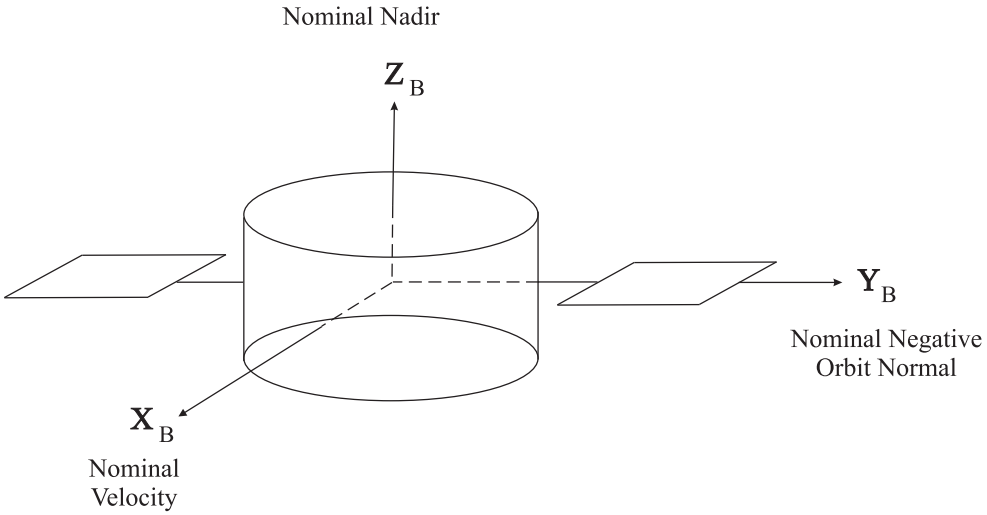

Figure 2.2: Spacecraft Fixed Coordinate System

The orbit reference frame defines the coordinate system for the spacecraft-fixed reference frame using the orbital elements. It is a spacecraft centered coordinate system and it is used to calculate the attitude of the satellite relative to the earth. The z-axis of the orbit reference frame is always in the nadir direction. The x-axis points in the satellite velocity direction and the y-axis

points in the negative orbit normal direction, as seen in Figure 2.3.

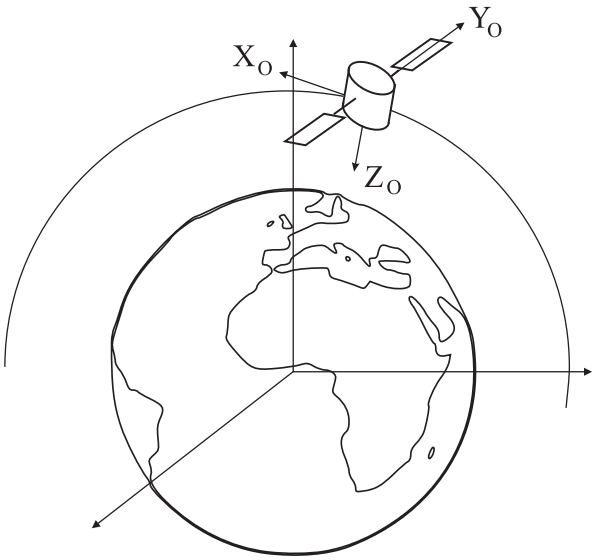

Figure 2.3: Orbit Reference Frame

The earth centered earth fixed (ECEF) reference frame is a right orthogonal coordinate system and as the name states, its origin is at the center of the earth. The z-axis is in the direction of the north pole, the x-axis is in the direction of intersection between the equatorial plane (0 degrees latitude) and the Greenwich meridian (0 degrees longitude) and the y-axis is the cross product between the z- and x-axis.

Lastly the earth centered inertial (ECI) reference frame is used for orbit simulation purposes as it is also the basis for the physical laws which hold in space. To be able to use Newton's laws for modeling a spacecraft in space, an inertial coordinate system is needed as reference. The coordinate system is fixed with respect to the direction of the vernal equinox and its origin is also at the center of the earth, as is the case with the ECEF reference frame.

2.1.2 Orbit parameters

The orbit of the nanosatellite will depend on the orbit of the mother satellite with which it will be launched. Assuming that the mother satellite will be

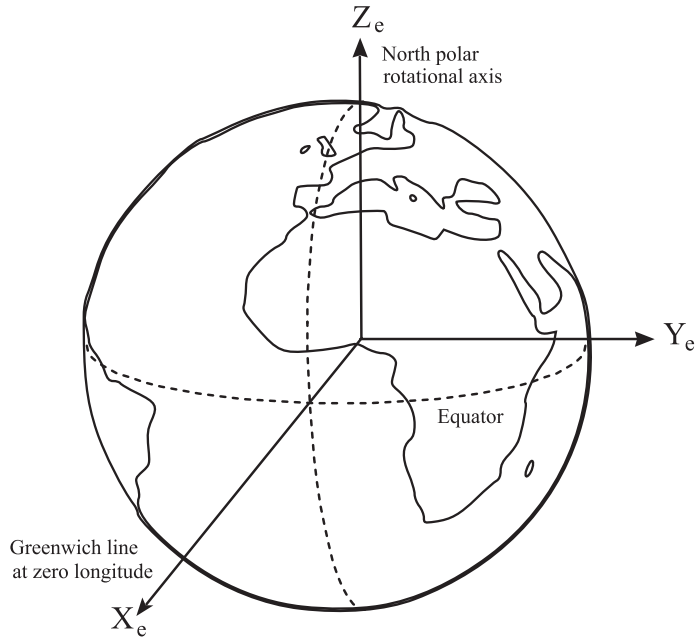

Figure 2.4: ECEF Reference Frame

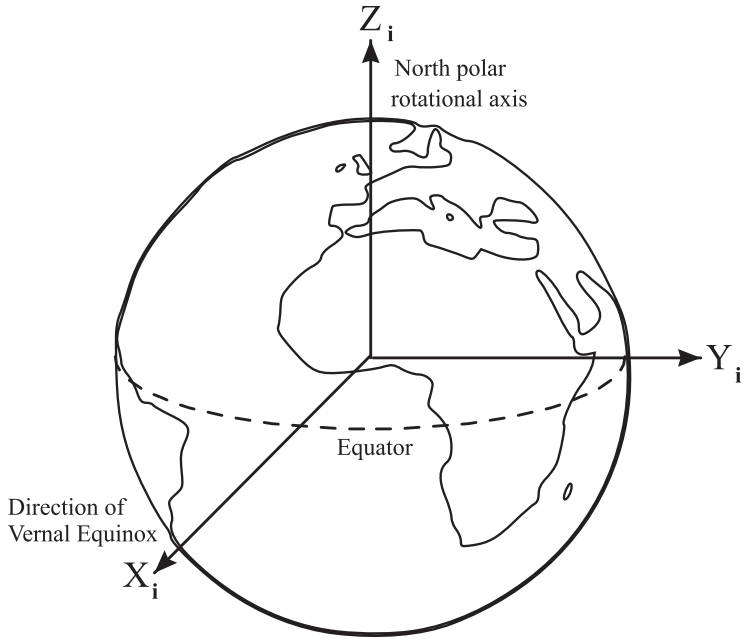

Figure 2.5: ECI Reference Frame

a low earth orbit (LEO) earth observation satellite, it will have a polar sun-synchronous orbit. Sun-synchronous orbits have a retrograde precession of 360 degrees per year, which will ensure that the satellite will pass over the equator at the same local time every orbit. Sun-synchronous orbits are possible for polar orbits with the correct inclination and altitude. For altitudes between 400 and 900 km the inclination must be $98^\circ \pm 1^\circ$ for the orbit to be sun-synchronous.

2.2 Control Algorithms

In this section the different aspects of the satellite attitude control algorithms which were tested will be discussed. The inputs to the controller are the quaternion error and the orbit referenced angular velocity of the satellite. The output of the controller is the reference wheel torque. The controller output will then be sent to the reaction wheel model.

2.2.1 Quaternion feedback

The Euler angle parametrization suffers singularities at ± 90 degree pitch angles when converting from the spacecraft coordinate system to the orbit reference frame. To avoid this problem, the quaternion approach is used, which has a 4-element vector definition without any singularities.

The quaternion error is calculated by using the current and the reference satellite attitude in quaternion representation as shown in equation (2.2.1).

$$\mathbf{q_e} = \begin{bmatrix} q_{4c} & q_{3c} & -q_{2c} & q_{1c} \\ -q_{3c} & q_{4c} & q_{1c} & -q_{2c} \\ q_{2c} & -q_{1c} & q_{4c} & -q_{3c} \\ q_{1c} & q_{2c} & q_{3c} & q_{4c} \end{bmatrix} \mathbf{q} \tag{2.2.1}$$

Where,

$$\begin{aligned} \mathbf{q} &= \begin{bmatrix} q_1 & q_2 & q_3 & q_4 \end{bmatrix}^T \\ &= \text{Current quaternion (attitude)} \\ \mathbf{q_e} &= \begin{bmatrix} q_{1e} & q_{2e} & q_{3e} & q_{4e} \end{bmatrix}^T \\ &= \text{Quaternion error} \\ \mathbf{q_c} &= \begin{bmatrix} q_{1c} & q_{2c} & q_{3c} & q_{4c} \end{bmatrix}^T \\ &= \text{Reference (commanded) quaternion attitude} \end{aligned}$$

The quaternion feedback is a method which makes use of this quaternion error to calculate the error between the reference attitude and the current attitude of the satellite. This quaternion error is an input to the controller along with the orbit referenced satellite angular velocity to be able to calculate the control torque vector as the output of the controller.

2.2.2 PD control

Euler's rotational equations of motion of a rigid spacecraft, as discussed in Wie [18], is repeated here (2.2.2) for the sake of completeness.

$$\mathbf{u} = \mathbf{I}\dot{\boldsymbol{\omega}}^{\mathbf{I}}_{\mathbf{B}} + \boldsymbol{\omega}^{\mathbf{I}}_{\mathbf{B}} \times \mathbf{I}\boldsymbol{\omega}^{\mathbf{I}}_{\mathbf{B}} \tag{2.2.2}$$

Where,

$$\begin{aligned} \mathbf{u} &= \text{control torque input vector} \\ \mathbf{I} &= \text{inertia matrix} \\ \boldsymbol{\omega}^{\mathbf{I}}_{\mathbf{B}} &= \text{inertially referenced body angular velocity vector} \end{aligned}$$

A PD controller is used to control the reaction wheels of the satellite. The quaterion feedback controller for eigenaxis rotations, as discussed in Wie [18], was used in this project. The controller proposed by Wie [18] counteracts the gyroscopic term of Euler's rotational equation. However for most practical

rotational maneuvers the gyroscopic term is small and can be neglected. The control algorithm used in this project is shown in equation (2.2.3). The inputs of the controller are the quaternion error vector and the orbit referenced body angular velocity vector. The output of the controller is the control torque vector which is the input of the reaction wheel system. **P** and **D** are the controller gain matrices to be properly determined.

$$\mathbf{u} = \underset{\mathrm{U\ max\ i}}{\mathrm{sat}} \left(\mathbf{P}\mathbf{q_e} + \mathbf{D}\boldsymbol{\omega}_\mathbf{B}^\mathbf{O} \right) \tag{2.2.3}$$

Where,

$$\begin{aligned}
\mathrm{U}_{max_i} &= \text{Maximum control torque possible for axis i} \\
\mathbf{P} &= K_P\mathbf{I} \\
K_P &= 2\omega_n^2 \qquad (2.2.4) \\
&= \text{Proportional gain} \\
\mathbf{I} &= \text{Moment of inertia matrix} \\
\mathbf{q_e} &= \text{Quaternion error} \\
\mathbf{D} &= K_D\mathbf{I} \\
K_D &= 2\zeta\omega_n \qquad (2.2.5) \\
&= \text{Derivative gain} \\
\boldsymbol{\omega}_\mathbf{B}^\mathbf{O} &= \text{Orbit referenced body angular rate vector} \\
\zeta &= \text{damping ratio} \\
\omega_n &= \text{linear control bandwidth}
\end{aligned}$$

Variable limiter attitude error feedback

Wie [19] discusses an improvement on the control algorithm in equation (2.2.3). A variable limiter attitute error feedback is included in the controller. This improves the sluggish response (with increased transient overshoots) while using the previous controller, when larger rapid maneuvers are done. The slew rate limit needs to be adjusted for large commanded attitude angles. The improved controller is shown in equation (2.2.6). The improvement of the new controller is due to the fact that actuator saturation is prevented by implementing the attitude error feedback saturation. Wie [19] claims that the response using the improved controller is less sluggish and does not have a transient overshoot. The gyroscopic term of the Euler rotational equations

of motion is also neglected in this controller assuming it to be small for all practical rotational maneuvers.

$$\mathbf{u} = \underset{\text{U max i}}{\text{sat}} \left[\mathbf{P} \underset{\text{Li}}{\text{sat}} \left(\mathbf{q_e} \right) + \mathbf{D} \boldsymbol{\omega}_{\mathbf{B}}^{\mathbf{O}} \right] \tag{2.2.6}$$

Where,

$$L_i = \left(\frac{K_D}{K_P} \right) \min \left[\sqrt{4 a_i \left| q_{e_i} \right|} \ , \ \left| \omega_i \right|_{\max} \right] \tag{2.2.7}$$

$$= \text{Attitue-error feedback saturation limit for axis i}$$

$$a_i = U / I_i$$

$$= \text{Maximum control acceleration about axis i}$$

$$q_{e_i} = \text{Quaternion error for axis i}$$

$$\omega_{i\,\max} = \text{Maximum specified slew rate about axis i}$$

2.3 Tetrahedral Configuration

A tetrahedron is a triangular pyramid, which means that it is a polyhedron composed of four triangular faces, three of which meet at each vertex, as can be seen in Figure 2.6. A regular tetrahedron is one in which the four triangles are equilateral. For the reaction wheel configuration designed the triangles will all have side lengths of 60 mm. Using a tetrahedral shape mounting structure means that four equal momentum vectors, perpendicular to each side of the tetrahedron, amounts to a null momentum vector when they are added together.

2.3.1 Conversion Matrix

A conversion matrix is needed to convert the momentum vectors of each reaction wheel in the tetrahedral configuration to the satellite coordinate system. This is needed because the momentum vectors of the wheels are not perpendicular to each other, but rather perpendicular to the planes of the tetrahedral shape on which they are mounted. The angular momentum and torque vectors of the four reaction wheels are shown in the spacecraft coordinate system in Figure 2.7.

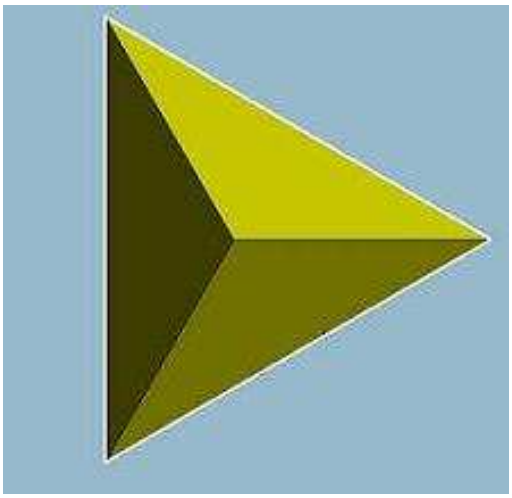

Figure 2.6: The Tetrahedron

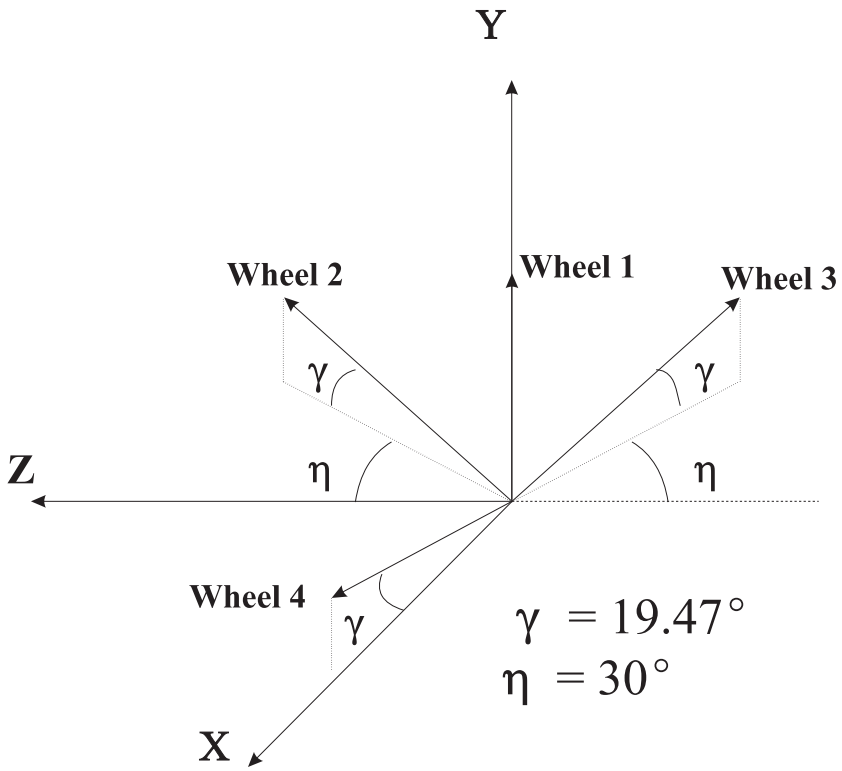

Figure 2.7: Tetrahedral Configuration

The conversion from the wheel angular momentum (or torque) vectors to the Cartesian coordinate system is shown in equation (2.3.1).

$$\begin{bmatrix} h_{wx} \\ h_{wy} \\ h_{wz} \end{bmatrix} = \begin{bmatrix} 0 & \cos\gamma & -\cos\gamma\sin\eta & -\cos\gamma\sin\eta \\ 1 & \sin\gamma & \sin\gamma & \sin\gamma \\ 0 & 0 & \cos\gamma\cos\eta & -\cos\gamma\sin\eta \end{bmatrix} \begin{bmatrix} h_1 \\ h_2 \\ h_3 \\ h_4 \end{bmatrix} \tag{2.3.1}$$

The conversion from the angular momentum (or torque) vectors in Cartesian coordinates to the wheel angular momentum and torque vectors is given in equation (2.3.2).

$$\begin{bmatrix} h_1 \\ h_2 \\ h_3 \\ h_4 \end{bmatrix} = \begin{bmatrix} 0 & \cos\gamma & -\cos\gamma\sin\eta & -\cos\gamma\sin\eta \\ 1 & \sin\gamma & \sin\gamma & \sin\gamma \\ 0 & 0 & \cos\gamma\cos\eta & -\cos\gamma\cos\eta \\ -2\sin\gamma\,(1+\sin\eta) & 2\sin\eta & 1 & 1 \end{bmatrix}^{-1} \begin{bmatrix} h_{wx} \\ h_{wy} \\ h_{wz} \\ 0 \end{bmatrix} \tag{2.3.2}$$

Chapter 3

Simulation

This chapter discusses the complete simulation process. It starts off with explaining the different models used in the simulation. The chapter goes on to discuss the simulation of the reaction wheel system. Thereafter the implementation of the reaction wheel control algorithm is shown. An explanation of how momentum dumping was simulated follows in the next section. The last section in this chapter discusses the PD control block which acts as the attitude controller for the satellite.

MATLAB Simulink is used as simulation environment throughout this project. The basis of the simulations used in this project was provided by Steyn [17]. The simulations were however for a microsatellite application and had to be changed to resemble a nanosatellite. The changes included:

- Modifying the reaction wheel model to simulate the tetrahedral reaction wheel system used in this project
- The speed loop and current loop transfer functions of the actual reaction wheels were determined and entered into the model
- The nanosatellite MOI was estimated and entered in the simulation
- Magnetic dumping was incorporated into the simulation
- The reaction wheel control was changed to control the smaller reaction wheels

3.1 Simulation Models

The full simulation includes the reaction wheel system model, the reaction wheel controller, the magnetic dumping controller, the satellite model and the obit model. This simulation can be seen in Figure 3.1. The different models and controllers used in this simulation will be discussed in further detail in the rest of this chapter. The simulation time has been chosen as 8000 seconds, which amounts to roughly one and a third times the orbital period.

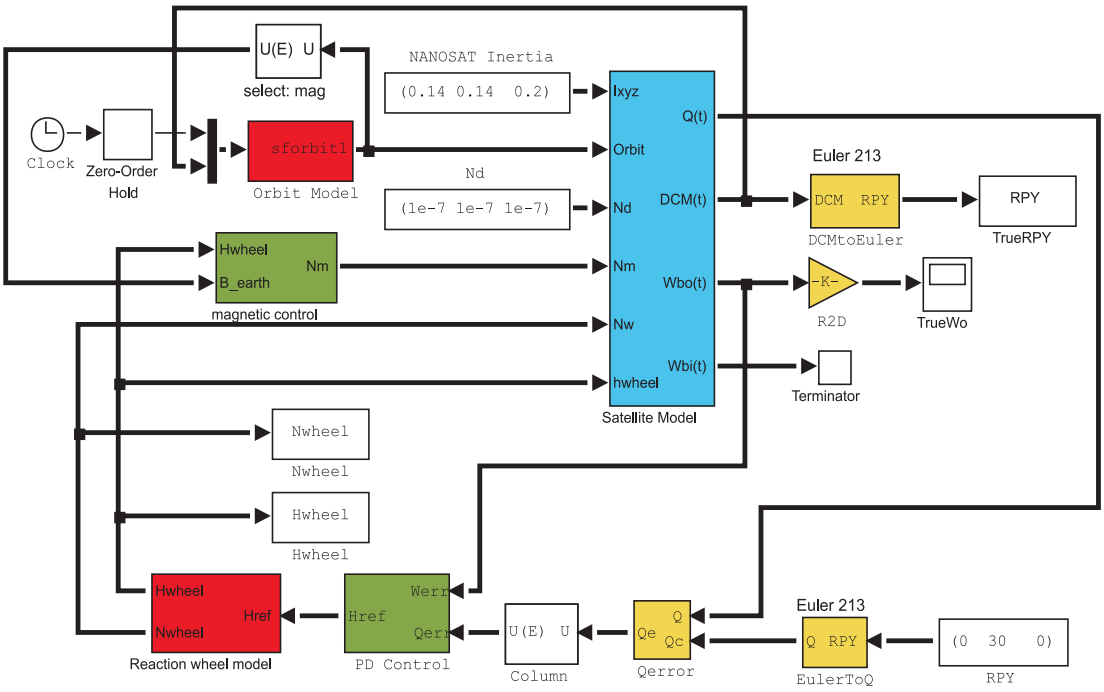

Figure 3.1: Simulink Simulation

The simulation requires a model of the orbit of the satellite. The orbit model is implemented in a S-function block, as seen in Figure 3.1. Using the satellite model, the attitude, orbit and inertially referenced angular velocity of the satellite can be determined. The desired satellite reference attitude is the input to the simulation. The error between the reference attitude and the current attitude is sent into the reaction wheel controller. The output of the controller is a torque command which is converted to an angular momen-

tum reference (through an integration process) for the model of the reaction wheels. The torque and momentum vector of each wheel is determined, using their non-linear models, and sent back to the satellite model.

3.1.1 Satellite Model

The satellite model is shown in Figure 3.2. The satellite dynamics can be described using Euler's dynamic equations of motion as seen in equation (3.1.1). The angular acceleration of the satellite referenced to the inertial coordinate system is influenced by the gravity gradient torque, the disturbance torques, the gyroscopic torque and the input torques exerted by the magnetic torquer and the reaction wheels. Inside the satellite model the inertially referenced satellite body angular velocities are converted to the orbit reference frame. This is used to calculate the current attitude of the satellite in quaternion and direction cosine matrix (DCM) representations.

$$\mathbf{I}\dot{\boldsymbol{\omega}}_{\mathbf{B}}^{\mathbf{I}} = \mathbf{N_{gg}} + \mathbf{N_d} + \mathbf{N_m} - \boldsymbol{\omega}_{\mathbf{B}}^{\mathbf{I}} \times \left(\mathbf{I}\boldsymbol{\omega}_{\mathbf{B}}^{\mathbf{I}} + \mathbf{h_w}\right) - \dot{\mathbf{h}}_{\mathbf{w}} \tag{3.1.1}$$

The satellite moment of inertia was estimated from the current predicted shape and mass of the satellite. The satellite will have a flat cylindrical shape with a diameter of 0.4 m and a height of 0.22 m. The moment of inertia of the satellite was estimated using the predicted mass of 10 kg and the moment of inertia calculations for a cylinder given in equations (3.1.2) and (3.1.3).

$$I_x = I_y = \frac{1}{12} m \left(3R^2 + h^2\right) \tag{3.1.2}$$

$$I_z = \frac{1}{2} m R^2 \tag{3.1.3}$$

3.1.2 Orbit Model

The orbit model makes use of the classical orbital elements (NORAD TLE) and the input reference time. The model gives a wide range of outputs which describe the orbit of the satellite. The outputs of the orbit model include the orbital period, the angular velocity of the satellite, the mean and true anomalies, the satellite altitude, latitude and longitude, a conversion matrix to convert from the inertial reference frame to the orbital reference frame and the inertially and orbitally referenced magnetic field of the earth.

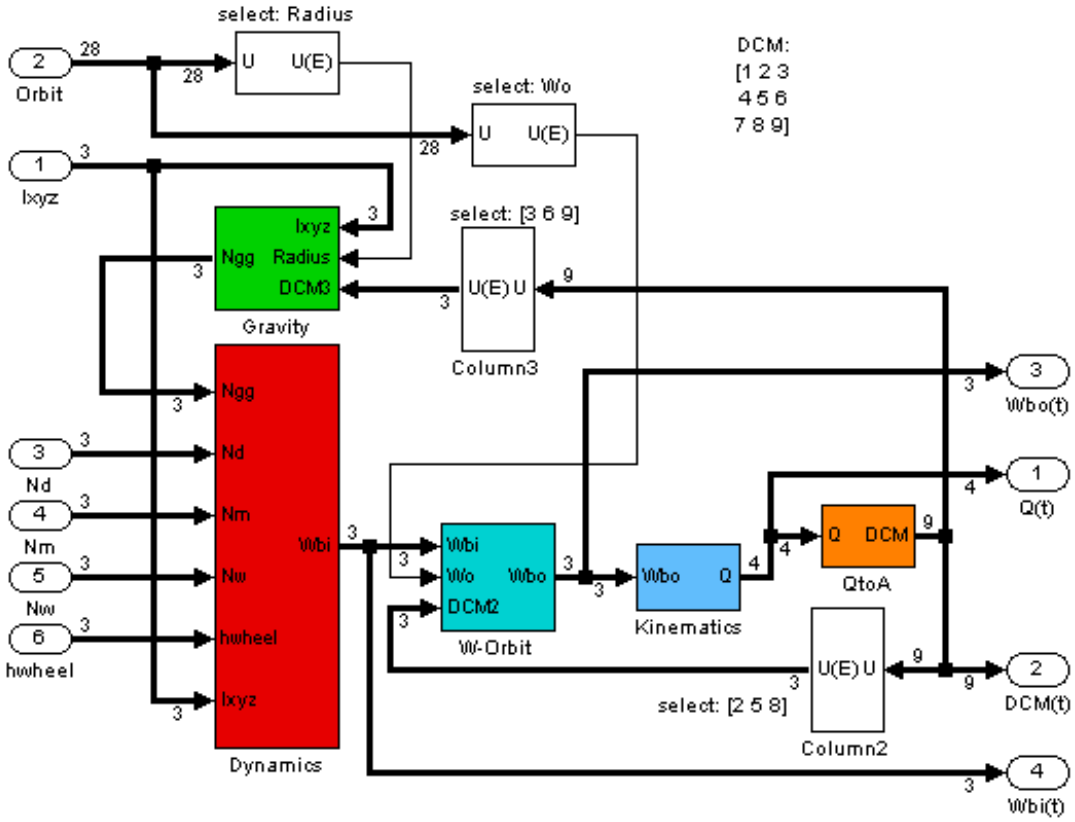

Figure 3.2: Satellite Model

3.1.3 Reaction Wheel System Model

A MATLAB Simulink simulation of the reaction wheel system of a microsatellite (designed by Steyn [17]) was modified so that it could be used to simulate the reaction wheel system of the nanosatellite designed for this project. The reaction wheel system model includes 4 non-linear models of each reaction wheel. One of the four identical non-linear models can be seen in Figure 3.3. The reaction wheel system model also includes the conversion matrix, as seen in equation (2.3.1), which converts the four reaction wheel momentum vectors to the satellite body coordinate system. In this model provision is also made for the fact that the reaction wheels will be spinning at an offset angular velocity of 1000 rpm. An offset wheel speed is used because an optical encoder could not be used to determine the wheel speed and direction, due to size constraints. As explained in more detail in section 4.4.1, the zero

wheel speed crossings therefore needed to be derived from the wheel speed information. Using this particular offset wheel speed minimizes the zero angular velocity crossings and therefore simplifies the wheel spinning direction determination process.

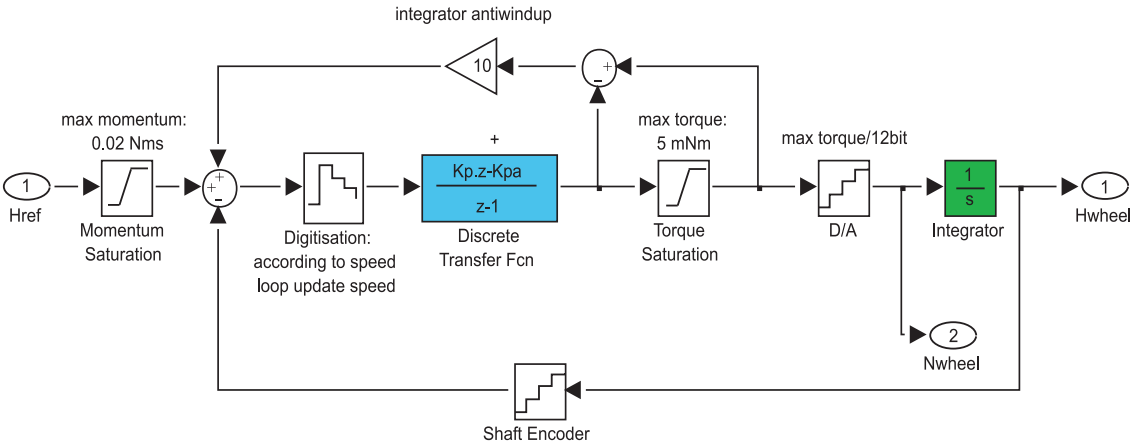

Figure 3.3: Reaction Wheel Model

The non-linear model of each reaction wheel is made up of the following components. At the centre of the non-linear model is the transfer function model of the current loop which is closed inside the brushless DC motor controller. The input to the current loop is the torque (which is related to the current) reference supplied by the speed loop controller and the output is the wheel angular momentum (which is related to the wheel speed). The current loop is assumed to be much faster (more than 10 times) than the speed loop, which is closed around the current loop. The transfer function of the current loop is therefore simplified to a single integrator and an open loop gain. The open loop gain is determined by plotting the wheel acceleration versus the current command. This is done by conducting various tests where the wheel acceleration is measured for different current commands. The wheel acceleration divided by the current reference gives the constant open loop gain.

The second part of the non-linear reaction wheel model is the speed controller which resides inside the 8051 microcontroller. It has a speed error input and a torque command (in digital to analog units) to the BLDC controller

as an output. The transfer function of the discrete PI controller is shown in equation (3.1.4). The calculation of the gains, K_p and K_pa, will be discussed in section 5.2.

$$G_{PI}(z) = \frac{K_P(z-a)}{z-1} \tag{3.1.4}$$

The discrete control difference equation (3.1.5), which will later be used when implementing the speed controller in the microcontroller, is derived from the transfer function shown in equation (3.1.4).

$$u(k) = u(k-1) + K_P e(k) - K_P a e(k-1) \tag{3.1.5}$$

The non-linear reaction wheel model also includes the momentum and torque saturation of each of the reaction wheels. The angular momentum buildup on each reaction wheel is limited to 20 mNms (at 5000 rpm) and the torque which can be exerted by each reaction wheel is limited to 5 mNm. The quantization steps of the digital to analog converter is taken as 2.44 μNm (4096 bits divided into a $\pm$5 mNm range). Anti-integrator windup is also implemented in this model to prevent the integrator from integrating the error when the torque saturation limit has been reached.

3.1.4 Speed controller algorithm

The wheel speed controller is implemented in the microcontroller as shown in equation (3.1.6). The design of this controller is discussed in section 5.2. Speed reference commands can be given at 100 ms intervals, the speed control loop is executed inside the 8051 microcontroller at 10 times per second. Therefore speed measurements are also done at these intervals. The previous torque command and the current and previous angular velocity errors are used as inputs to the controller. The output of the controller is the torque reference command which is converted to digital to analog units before it is sent to the brushless DC controller. The integrator gains K_1 and K_2 are calculated (in section 5.2) according to the closed loop damping and settling time specifications.

$$N_{command}(k+1) = N_{command}(k) + \omega_{err}(k+1) * K_1 - \omega_{err}(k) * K_2 \tag{3.1.6}$$

3.2 Momentum dumping

Momentum dumping is the method of removing unwanted accumulated angular momentum from the reaction wheels. This momentum buildup is due to secular external disturbances on the satellite. Some of the secular disturbance torques are caused by the earth's magnetic field, gravitational and aerodynamic influences on the satellite body. Momentum dumping is done by using the magnetic torquers to create a torque in the opposite direction of the angular momentum vector which needs to be dumped. This section will discuss the algorithms which were used to implement momentum dumping in the Simulink simulation.

The magnetic control block uses the B-field of the earth, as predicted by the orbit propagation model, alongside with the reaction wheel angular momentum vectors in spacecraft body coordinates to calculate the torque which needs to be exerted by the magnetic torquers. The algorithm used to calculate this torque is shown below, in equation (3.2.1), where $\boldsymbol{B}$ is the earth's magnetic field, $\boldsymbol{H}$ is the angular momentum of the reaction wheels in spacecraft body coordinates, $\boldsymbol{M}$ is the torque exerted by the magnetic torquers and k is the magnetic controller gain. The constant, k, must be negative, because the torque generated by the magnetic torquers must be in such a direction so as to decrease the momentum built up on the reaction wheels.

Equation 3.2.1 is obtained by assuming that the earth's magnetic field, $\boldsymbol{B}$, is always perpendicular to the commanded magnetic dipole moment, $\boldsymbol{M}$. The components of the earth's magnetic field (in the orbit reference frame) are time-varying and depend on the orbit parameters (as discussed by Sidi [13]). It is therefore not possible to make use of an analytic method to find the correct value of the controller gain k (in equation (3.2.1)). The optimal value which was found to be $k = -1$, was therefore determined using the "cut-and-try" method. The estimated magnetic torquer saturation value was taken into account when the controller gain was designed. For the designed k value the commanded magnetic moment stays within the specified magnetic torquer saturation value for the simulated disturbance torques.

$$\boldsymbol{M} = k\frac{\boldsymbol{H} \times \boldsymbol{B}}{|\boldsymbol{B}|^2} \tag{3.2.1}$$

The results of the implemented momentum dumping control algorithm can be seen in section 6.1.3. Momentum dumping can however only by done when the magnetic field (B-field) vector of the earth and the momentum vector to be dumped are not in the same direction. This can be seen from the cross product in equation (3.2.1). The cross product implies that the magnetic torque applied depends on the angle between the angular momentum vector and the B-field of the earth, the magnetic torque is a maximum when the angle is 90 degrees and zero when the angle is 0 degrees. Momentum dumping is thus constrained by the position of the satellite in its orbit.

3.3 PD controller block

In section 2.2.2 the theory behind the PD controller was discussed. The gains K_P and K_D were chosen using equations (2.2.4) and (2.2.5) and the closed loop specifications as shown in equation (3.3.1). Inside the PD control block the closed loop specifications, ζ and ω_n, were implemented as constants which can therefore be changed easily (as seen in Figure 3.4). The torque saturation of 5 mNm is also implemented in this block. The torque command is integrated using a discrete integrator, with a sample time of 1 second, to calculate the momentum reference which is sent to the reaction wheel model. This satellite attitude controller is closed at 1 Hz, which is the reason for the integrator sample time of 1 second. This sample time is therefore slow enough to incorporate reaction wheel speed loop controller which is closed at 10 Hz.

$$\begin{aligned} t_{s\,5\%} &= \frac{3}{\zeta\omega_n} \\ &= \text{five percent settling time} \end{aligned} \tag{3.3.1}$$

3.3.1 Variable limiter attitude error feedback controller

The improved PD controller as discussed in section 2.2.2 is now implemented in the simulation. The only difference between the previous (Figure 3.4) and the improved PD controller is the fact that the quaternion error feedback is limited. From Wie [19] it follows that, as the quaternion error increases, the slew rate limit increases for rapid and large maneuvers. This means that the overall response becomes sluggish and has an increased transient overshoot because the actuator is saturated. To achieve improved settling times for

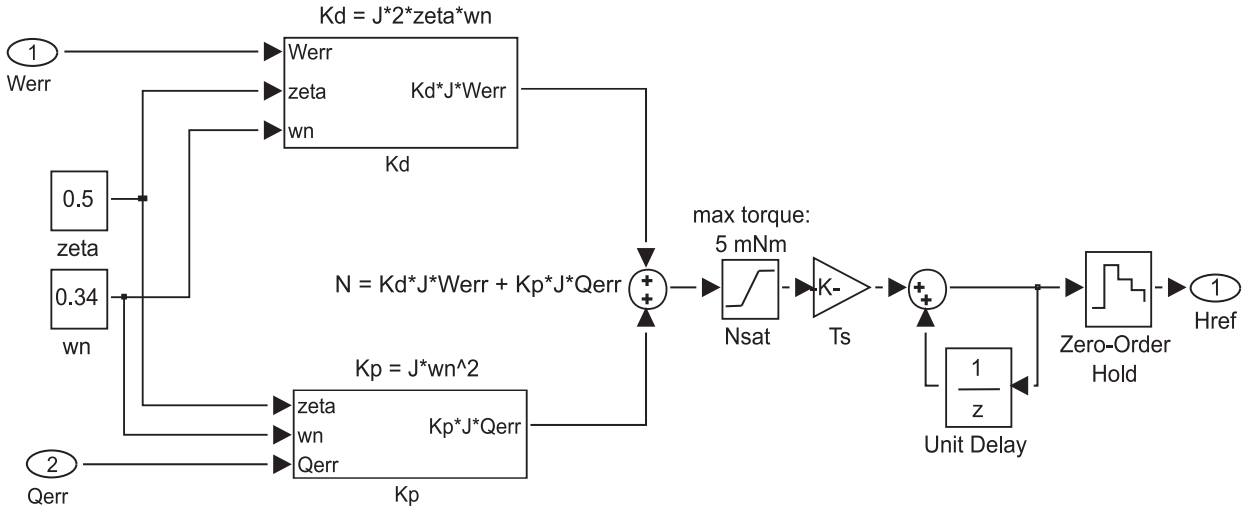

Figure 3.4: PD satellite attitude controller

large maneuvers the slew rate limit is adjusted as showed in equation (2.2.7). The variable limiter insures that the actuator is not saturated and it improves the transient response for large maneuvers. The results of this improved controller will be discussed and compared to the PD controller without attitude error saturation in section 6.1.1.

Chapter 4

Hardware Design

In this chapter the detail design of the different actuators and sensors covered in this project will be discussed. To start with, the design requirements of the ADCS system will be explained. This includes all the actuator and sensor specifications relevant to this project. Thereafter the mission objectives will be stated and discussed. This will be followed by a full explanation of all the design steps followed to complete the reaction wheel system and the rate sensor system.

4.1 Requirements

Previous research at the ESL has been done by Bootsma [4], Ntsimane [10], Baker [1], Greyling [8] on the subsystems of microsatellites, on which the current research on the subsystems of nanosatellites is based. Therefore the main aim of the current subsystems developed is to compact the improved technology into smaller and lighter final units. The biggest requirement of this project is therefore to make the final product as small and as light as possible, due to the fact that it will eventually be flown on a nanosatellite. Another requirement that goes with the size constraint is the power constraint. Smaller, lighter batteries and solar panels must be used on nanosatellites and therefore the subsystems of nanosatellites must be as power efficient as possible.

4.1.1 Reaction Wheel Specifications

Firstly each reaction wheel must be able to deliver a torque of 5 mNm. The reaction wheels must also be able to store an angular momentum of 20 mNms.

This means that the maximum angular velocity of each reaction wheel must be 5000 rpm, while each wheel has a moment of inertia around the spinning axis of 38.2 $\times 10^{-6}$ kgm^2. The minimum speed command which each reaction wheel must be able to follow is 50 rpm.

4.1.2 Rate Sensor Specifications

The aim of building this sensor was to determine whether it is in fact a feasible sensor to use on a nanosatellite. The power usage and sensor drift was analyzed and compared to other off-the-shelf components. It was only required to determine most accurate angular velocity measurements which can be obtained from the rate sensors, this implies that the sensor drift must be as low as possible.

4.1.3 Mission

This nanosatellite will be used as an inspection satellite to observe another satellite (a mother satellite) which will be in close proximity. This means that the nanosatellite's main payload will be a camera to image the mother satellite. It also means that the nanosatellite will have to be 3-axis stabilized to be able to take these images. This requires reaction wheels for accurate attitude control. Magnetic torquers will also be needed to dump the momentum on the reaction wheels, because of momentum buildup due to external disturbance torques on the satellite. To be able to inspect all the sides of the mother satellite, the nanosatellite will have to be in such an orbit so that it will orbit around the mother satellite. The rotation of the nanosatellite to keep its camera facing the mother satellite will be controlled by the onboard ADCS. The nanosatellite will be launched together with the mother satellite, but will inevitably have different drag characteristics. Therefore the nanosatellite will need a propulsion system to enable it to rendezvous with the mother satellite and to make minor orbit adjustments.

4.2 Reaction Wheel Design

In this section the detail design of the reaction wheel will be discussed. Firstly the decisions made during the design of the mounting structure will be explained, the choice of motor will be defended and the rotor design will be

discussed. Lastly the process of designing the motor controller and microcontroller electronics will be presented.

4.2.1 Structure

The reaction wheel system must be redundant and support a zero momentum bias with offset wheel speeds, so the design decision was made to mount the four reaction wheels in a tetrahedral formation. As explained in section 2.3 equal angular momentums of the four reaction wheels amounts to a nett zero momentum vector. This allows each reaction wheel to spin at an equal offset angular velocity of 1000 rpm while the nett momentum stays zero. Due to this fact and the fact that the tetrahedral configuration occupies a smaller volume than the pyramid configuration, the tetrahedral configuration was chosen. The positive directions of the angular momentum vectors can be seen in Figure 2.7.

The structure was chosen to be as small as possible and as rigid as possible to minimize structure vibrations during launch. The structure fits into a figurative cube with dimensions 100 mm by 100 mm by 100 mm. A Solid Edge drawing of the tetrahedral structure alone can be seen in Figure 4.1. The smallest possible tetrahedral shape structure was chosen so as to allow for the rotors to each have a diameter of 50 mm (which will be on the outside of the structure). The four brushless DC motors will be mounted in the center of each of the four plates on the inside of the structure and their axes, on which the rotors will be mounted, will be protruding from the structure as can be seen in Figure 4.2.

The structure can be fully disassembled into 4 plates and 3 standoffs (see Appendix A.1), when assembled all junctions of neighbouring pieces are held together by two 2.5 mm bolts. It is necessary to be able to disassemble the structure fully, because the motors are in such close proximity of each other on the inside of the structure, when assembled, that they have to be fixed to the plates before connecting the plates to each other. The four plates which constitute the tetrahedral structure are also identical, as are the three standoffs, which simplifies the production. The plates were manufactured using laser cutting technology which ensures accuracy. A method called stitching (small slits cut by the laser) was used along the folding lines to ensure that

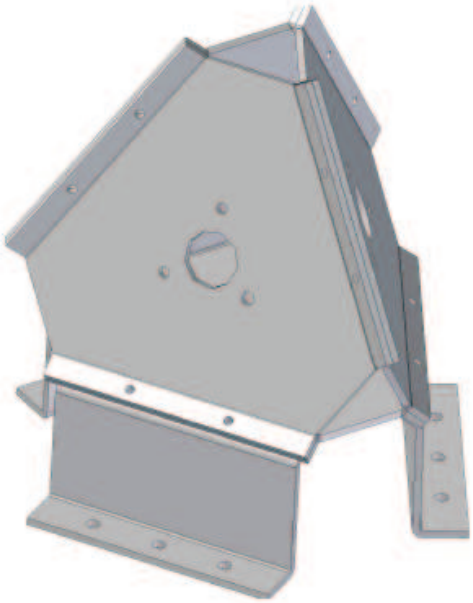

Figure 4.1: Tetrahedral Structure

the position of the folds were accurate.

The reflective optical sensors, used to measure the rotational speed of the rotors, are also mounted in a corner of each of the four plates. The distance from the sensor to the rotor was chosen to provide optimal reflective surfaces for the sensor to discriminate between the polished and black surfaces of the rotor. The standoffs are mounted on the mounting plate, which serves as a baseplate for the structure and a means to mount the structure and the PCB to the satellite.

Due to the triangular shapes which are connected to each other to make up the tetrahedral structure it can withstand large vibrational forces. This is one of the reasons why this shape was chosen. The shape of the tetrahedral structure was therefore assumed to be rigid enough so as to be able to use 1.6 mm aluminium, but further vibration tests would be necessary to verify this assumption. Possibly 1.2 mm aluminium (or maybe even 0.9 mm) could suffice, depending on the vibration specifications of the specific launch vehicle used to launch the nanosatellite.

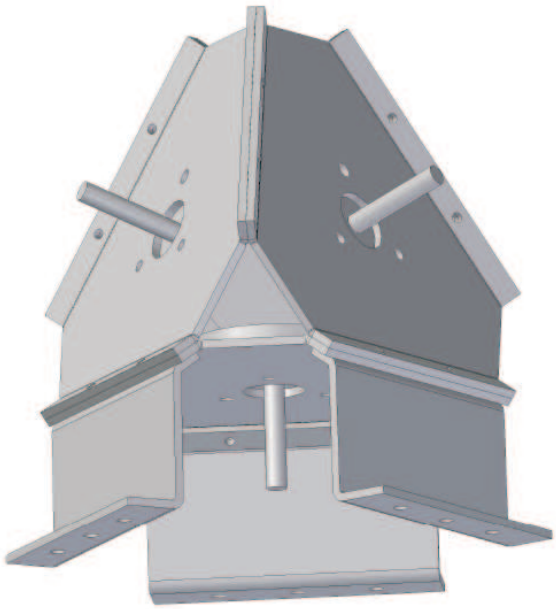

Figure 4.2: Tetrahedral Structure with Motors

4.2.2 Rotor

The material used for the rotor was chosen to have a high density, so as to decrease the volume of the rotor. The other criterion for the material was that it should be easily obtainable and relatively inexpensive. Therefore brass was chosen. The moment of inertia of each rotor around the spinning axis was calculated as 38.2 $\times 10^{-6}$ kgm^2 from the reaction wheel requirements. The rotor diameter was designed to be 50 mm. The rotor has a cup like shape with 1 mm deep slits (1.2 mm wide) on its perimeter, which are used to determine the rotational speed of the rotor, as seen in Figure 4.3. The only problem with this material is the fact that it forms an oxidation layer in a short period of time, which makes the surface dull. This reduces the reflectiveness of the polished surface and the reflected signal coming from the diode is therefore also weaker. This can lead to faulty speed readings and a sealant had to be found to prevent this oxidation.

For the first design iteration it was chosen to machine 40 slits into the rotor. This yielded a speed measurement resolution of 1.5 rpm at a 1 Hz sampling frequency. Seeing that the satellite attitute control loop should ideally be closed at 1 Hz, a faster sampling frequency for the speed measurement was

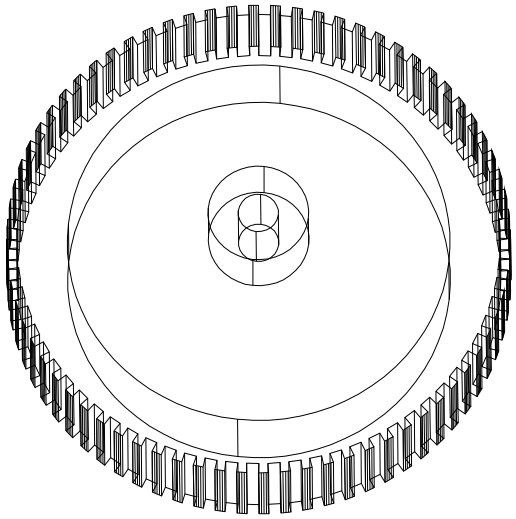

Figure 4.3: The Brass Rotor

needed. A better resolution could only be obtained when more slits were machined into the rotor. Therefore during the next design iteration it was chosen to machine 72 slits on the side of each rotor, which would yield a speed measurement resolution of 8.33 rpm at a faster sampling frequency of 10 Hz. This would allow the satellite attitude controller to run at 1 Hz. The speed loop is therefore executed every 100 ms (as explained in section 3.1.4), but the angular velocity is only displayed every second, thus with a resolution of 0.83 rpm. There was no speed measurement resolution requirement, the resolution must only allow for the speed loop to be closed at 10 Hz. The specific number of slits was chosen due to the fact that it was easier to machine slits into the rotor at integer angles (in this case 5 degrees). A better resolution could be obtained by machining more slits on the perimeter of each rotor, but the accuracy at which it could be machined would deteriorate due to the machinery available. Therefore it was decided to keep to 72 slits for this project until funding allowed a better machining process.

4.2.3 Motor

A brushless DC motor was chosen for this project, because the commutation wear on a brushed DC motor is not desired for space applications. Three small brushless DC motors were considered for this project, the 5.2 mNm Faulhaber motor, the 13 W and the 6 W EC flat Maxon motor (see datasheets

in Appendix B). The three key elements, on which the choice of motor was made, were the size of the motor, its nominal operating voltage and the power consumption of the motor. In the next 3 paragraphs these three criteria will be discussed for each motor and the final decision will be motivated.

The maximum torque requirement for each motor is 5 mNm (according to the specifications, see section 4.1.1). The power consumption, at an output torque of 5 mNm and an angular velocity of 5000 rpm, of each motor was therefore compared to each other. The power consumption under these operating conditions of the Faulhaber motor is 5.65 W, the 6 W Maxon motor, 4.98 W, and the 15 W Maxon motor, 4.92 W (see Appendix B for calculations). It can therefore be seen that the 15 W Maxon Motor has the smallest power consumption by a small margin.

The size of the motor was to be as small as possible. This is why the EC-flat series of Maxon motor was chosen above the Faulhaber motor. The brushless DC motors in the EC flat series has an axial length of 28 mm in total, which is a critical dimension in this compact design. The axial length of the Faulhaber motor is 44 mm. Using this motor would enlarge the tetrahedral configuration by a significant amount.

The nominal voltage also needed to be in the 12 V range, due to the smaller power supply which will be used on the nanosatellite. Therefore the 6 W Maxon motor with a nominal operating voltage of 9 V was chosen above the 15 W Maxon motor with a nominal operating voltage of 24 V.

It is therefore clear that, by taking all the above specifications in account, the 6 W Maxon motor was the best choice of motor for this project.

4.2.4 Motor Drive Electronics

The motor drive electronics can be divided into 4 parts, the 8051 microcontroller and its components, the four brushless direct current (BLDC) controllers and their peripheral components, the power distribution and communications components. The schematics for these four parts of the motor drive electronics can be seen in Appendix A.2.

8051 microcontroller

The 8051 microcontroller has a 16 MHz crystal as clock source. This clock source was chosen so that the CAN controller can operate at 1 Mhz, the UART baud rate at 19200 baud and a timer can be set up to interrupt at 10 Hz for the wheel speed control loop. External to the microcontroller a reset circuit is set up to prevent small voltage drops in the power supply from resetting the microcontroller. The serial peripheral interface (SPI) of the microcontroller is used to communicate with an external digital to analog converter (DtoA) which drives the references for the BLDC controllers. The inter-integrated circuit (I2C) port of the microcontroller is used to interface with an external analog to digital converter (AtoD), which converts the rate sensor outputs. The Joint Test Action Group (JTAG) interface is used to program the microcontroller. Four output pins on the microcontroller are used to drive the enable inputs of the BLDC controllers and another four output pins drive the direction of rotation input pins on the BLDC controllers. Four input pins of the microcontroller are configured as external timer inputs and act as counters to count the pulses from the optical reflective sensors, to determine the rotational speed of the rotors.

BLDC controllers

The BLDC controller from ST Microelectronics (with component number L6235) and its peripheral components have been chosen to fit the application. One of the main requirements was that the controller should have an onchip three-phase transistor bridge to drive the BLDC motors. This would minimize the PCB space required for these components, as one controller would be needed for each of the four BLDC motors. The other requirements for the controllers are: It should be able to operate from a 12 V supply and it should be able to deliver 0.7 A of current to the motor. The peripheral components for the BLDC controllers include a charge pump, an external overcurrent and thermal protection circuit, a current sense resistor, a PWM off time selection RC circuit, a speed output pulse width selection RC circuit and bypass capacitors and pull up resistors on the Hall sensor inputs.

The internal workings of the BLDC controller will now be discussed briefly by taking a look at its block diagram as seen in Figure 4.4. The first is the

constant off time PWM controller which makes use of an external RC circuit to determine the off time. The external RC circuit has been chosen to give a PWM switching frequency of between 8 kHz and 10 kHz (depending on the on-time chosen by the controller). The optimal switching frequency would be between 25 kHz and 40 kHz, but the choice was limited by the minimum on time which is set by the controller.

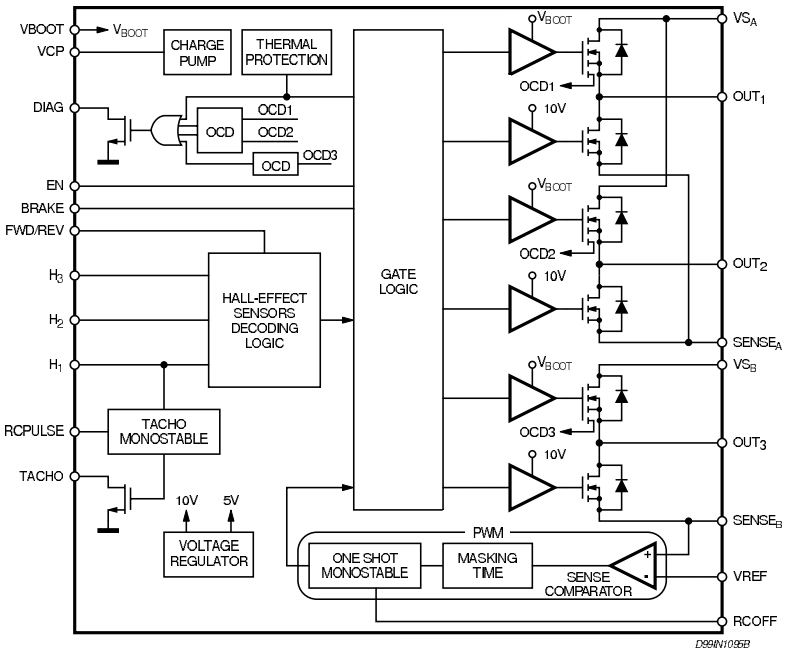

Figure 4.4: BLDC controller Block Diagram

The second part of the BLDC controller consists of the three phase transistor bridge which drives the BLDC motors. The current drawn by the BLDC motor is determined by measuring the voltage drop over a sense resistor which is connected between the source of the three lower transistors in the bridge and ground.

The tacho monostable uses the signal coming from the first Hall sensor to output a pulse which length can be determined by an external RC circuit. The BLDC motor uses an eight pole permanent magnet, which means that four pulses per revolution can be measured and used to verify the speed output coming from the reflective optical sensors. The pulse width is chosen to

be short enough to accommodate the maximum rotational speed and long enough to be registered on an input pin on the 8051 microcontroller. The maximum rotational speed is 5000 rpm, resulting in the upper bound of the pulse width of 3 ms and the lower bound set by the 8051 microcontroller is 125 ns. A pulse width of 282 μs was therefore chosen and the resulting resistor and capacitor values were calculated according to equation (4.2.1).

$$t_{PULSE} = 0.6 \times R_{PUL} \times C_{PUL} \tag{4.2.1}$$

The Hall-effect sensors decoding logic provides the appropriate driving of the three-phase bridge outputs according to the signals coming from the three Hall sensors. Lastly onboard the controller there are thermal protection and overcurrent detection circuits to protect the controller against overheating and drawing too much current.

The sense resistor is chosen according to the peak current in the load and there are two constraints to its resistance value. The first is that it dissipitates energy due to the fact that all the current drawn by the BLDC motor flows through this resistor and must therefore be kept as small as possible. The second constraint is the fact that the voltage over the sense resistor is compared to the reference voltage by the comparator; therefore the lower the sense resistor value is, the higher the peak current error will be, due to noise on the input reference voltage.

The recommended voltage drop over the sense resistor (according to the datasheet) is 0.5 V when the peak current is flowing through it (see equation (4.2.2)). The power rating of the sense resistor must also be taken into account and can be calculated using equation (4.2.3). A resistance value of 0.733 Ω is therefore chosen for the sense resistor, which is achieved by putting three 2.2 Ω resistors in parallel (the parallel combination insures that the power capability is adequate). The maximum torque required, of 5 mNm, results in the maximum current of 0.7 A drawn by the BLDC motor. This was calculated using the torque constant of the BLDC motor (according to its datasheet) and determining the static and dynamic friction during operation. The required power rating is therefore 0.36 W. Each of the 2.2 Ω resistors have a power rating of 200 mW resulting in a combined power rating of 600 mW which meats

the requirement.

$$R_{sense} = 0.5/I_{peak} \tag{4.2.2}$$

$$P_R = I_{peak}^2 \times R_{sense} \tag{4.2.3}$$

Power Distribution

Three voltage levels are needed to supply the components on the Motor Drive Electronics PCB. The BLDC controller needs a 12 V supply, the 8051 microcontroller needs a 3 V supply and the rest of the components need a 5 V supply. The 12 V supply which is connected to the PCB is regulated down to 5 V using a switching regulator (with an efficiency between 86% and 95% depending on the load and the input voltage). The 5 V supply is then regulated to 3 V using a linear regulator.

Communications

The 8051 microcontroller communicates with the ground test computer using a serial UART connection. This communication is used to send the wheel speed and rate sensor information to the ground test computer and to receive speed commands from the ground test computer, for demonstration and ground testing purposes. The hardware for the CAN bus connection to communicate with the on-board computer is also implemented. The SPI on the 8051 microcontroller is used to communicate with the DtoA converter which outputs an analog voltage to the voltage reference input on the BLDC controller. The I^2C connection on the 8051 microcontroller is used to communicate with the AtoD converter which converts the rate sensor data as stated previously.

4.3 Rate Sensor Design

The design of the rate sensor system can be divided into 3 parts, the PCB design, the mounting design and the calibration of the sensors. These three design steps will be discussed briefly below. The rate sensors manufactured by Analog Devices (with component number ADXRS401), which will be used in this project, have a range of $\pm 75\ ^\circ/\text{s}$.

Micro electromechnical (MEMS) gyros are usually designed as an electronically driven resonator, often fabricated out of a single piece of quartz or silicone, as described in Bijker [3]. The working of a MEMS gyro relies on the Coriolis force that causes displacements of the resonator when an angular rate is applied to the sensor. These displacements can be detected by a capacitive pickoff and demodulated to form the output of the sensor.

4.3.1 PCB design

The rate sensor system is divided into 4 parts, the three PCBs on which the rate sensors are mounted, for the x, y and z-axis and the main gyro board, which hosts the AtoD converter and the instrumentation amplifiers. The schematics for these hardware designs are shown in Appendix A.3.1.

Three rate sensors are used per axis to be able to improve the estimation of the true angular velocity. Thus on each of the three PCBs which are mounted on the rate sensor mounting structure there are 3 rate sensors and their peripheral components, which includes a passive 20 Hz low pass filter. The filter cut off frequency was chosen while considering the 100 Hz sampling frequency. The design of this filter is discussed in Appendix A.4. The Nyquist frequency (50 Hz) is therefore half of the sampling frequency and acts as the upper bound for the low pass filter cut off frequency. This upper bound ensures that no aliasing occurs. The nominal output of the rate sensor is 2.5 V and it deviates 15 mV per $^\circ$/s angular velocity. A full scale angular velocity of $\pm 15\ ^\circ$/s is used for this satellite application. This means that the output of the rate sensor will swing between 2.275 V and 2.725 V.

On the main sensor board instrumentation amplifiers are used to rescale the rate sensor output signal to use a bigger range of the AtoD converter's possible inputs. A 2 V reference is subtracted from the rate sensor output before amplifying the signal by factor of 2. The minimum and maximum output of the instrumentation amplifier will thus now be 0.55 V and 1.45 V respectively for the full scale angular velocity outputs from the rate sensor. The AtoD converter uses an internal reference of 2.048 V which means that the minimum and maximum outputs of the AtoD converter will be 1100 and 2900 (DtoA units) respectively. This means that a resolution of $16.67 \times 10^{-3}\ ^\circ$/s can be obtained.

4.3.2 Mounting structure

Firstly it is very important that the 3 surfaces on which the x, y and z rate sensors will be mounted on must be orthogonal to each other. Care has thus been taken in the manufacturing of the structure to respect this specification. Secondly it was important that the structure should be as light as possible, but materials which tend to outgas in space had to be avoided. Delrin was thus chosen, because it is a strong material which is easy to machine and does not outgas in space. A hollow cube was manufactured to save on weight, leaving just enough of the frame of the cube to mount the three PCBs (see Figure 4.5). The total weight of the structure is 9.4 g. Due to the fact that the dimensions of the PCB to which the rate sensors are soldered are 22 mm by 32 mm, the Delrin cube has dimensions of 32 mm by 32 mm by 22 mm.

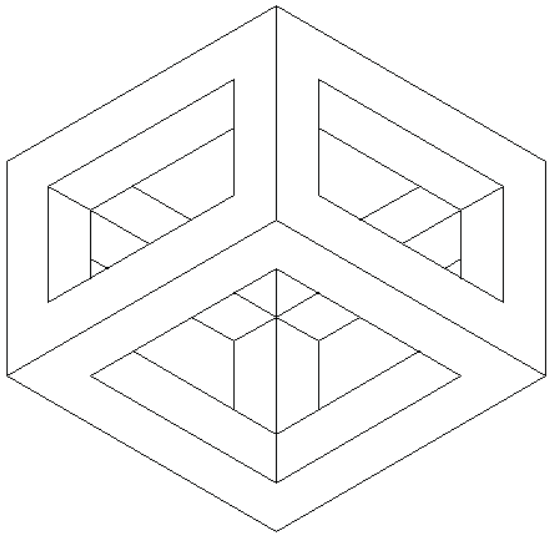

Figure 4.5: Rate Sensor mounting structure

4.3.3 Calibration

Before the rate sensors can be used they need to be calibrated. This procedure includes calibration of the axis, the temperature output, the offset drift due to temperature variation and determining the bias instability. Lastly the initial conditions of the rate sensor output were recorded just after the power

to the rate sensors were switched on. This will be used to calibrate the initial transients of the rate outputs due to the warming up of the rate sensors internally. These procedures will be explained in the sections to follow.

Orthogonality

Two of the tree rate sensors were used per axis, which means that there are effectively two sets of rate sensors which can be used to measure the angular rates. These two sets will from here on be referred to as rate sensor set 1 and 2. The orthogonality calibration was done fixing the rate sensor system to the inner gimbal of a turn table. Four tests per axis were performed, each consisting of a 360 degree rotation around the particular axis. The angular rate data was analysed by integrating the measured angular rates to obtain an angular displacement measurement for both sets of rate sensors as seen in Table 4.1 and 4.2. This measurement was then compared to the true rotation angle of 360 degrees to calibrate the axis.

Table 4.1: Rate Sensor Calibration Measurements (set 1)

	Experiment 1	**Experiment 2**	**Experiment 3**	**Experiment 4**
Roll Axis Test				
Roll Axis	357.5396	361.6532	353.4244	361.3211
Pitch Axis	0.0816	0.7392	0.9164	2.4368
Yaw Axis	11.8473	12.1771	8.7964	14.7277
Pitch Axis Test				
Roll Axis	0.2990	2.1714	0.6660	2.7608
Pitch Axis	363.9619	365.2805	362.9093	360.8096
Yaw Axis	4.3880	1.5358	6.6809	1.5553
Yaw Axis Test				
Roll Axis	1.0037	2.9626	1.2215	2.3299
Pitch Axis	0.8885	2.6775	2.4592	1.6639
Yaw Axis	363.9620	364.9807	361.5431	359.3850

As can be seen from Tables 4.1 and 4.2 there is some cross coupling between the roll, pitch and yaw axes. This cross coupling effect is due to the fact that the sides of the mounting structure might not be perfectly orthogonal to each other and the rate sensors might not have been soldered onto their

Table 4.2: Rate Sensor Calibration Measurements (set 2)

	Experiment 1	**Experiment 2**	**Experiment 3**	**Experiment 4**
Roll Axis Test				
Roll Axis	347.8919	349.8659	339.7070	350.5748
Pitch Axis	1.7944	0.5451	1.2360	1.3549
Yaw Axis	14.2961	11.2277	8.2123	13.6768
Pitch Axis Test				
Roll Axis	0.1142	1.6765	0.2184	0.7802
Pitch Axis	346.8632	341.4480	348.7228	343.0313
Yaw Axis	3.8859	2.7142	0.8585	1.1198
Yaw Axis Test				
Roll Axis	5.9208	6.2102	10.3636	10.6652
Pitch Axis	0.1456	1.2869	3.5055	0.7491
Yaw Axis	364.5231	364.9161	359.3170	361.4272

respective PCBs very accurately. A decoupling matrix (**A**, as seen in equation (4.3.1)) was calculated to correct these errors. The method of calculating this decoupling matrix is shown in equation (4.3.2). This decoupling matrix is then multiplied with the rate sensor measurements to obtain the true angular velocities.

$$\begin{bmatrix} Y_{cr} & Y_{cp} & Y_{cy} \end{bmatrix} = \mathbf{A} \times \begin{bmatrix} Y_{mr} & Y_{mp} & Y_{my} \end{bmatrix} \quad (4.3.1)$$

$$\mathbf{A} = \begin{bmatrix} Y_{cr} & Y_{cp} & Y_{cy} \end{bmatrix} \times inv\left(\begin{bmatrix} Y_{mr} & Y_{mp} & Y_{my} \end{bmatrix}\right) \quad (4.3.2)$$

Where,

Y_{cr} = average true roll angle of rotation for the four experiments

Y_{cp} = average true pitch angle of rotation for the four experiments

Y_{cy} = average true yaw angle of rotation for the four experiments

Y_{mr} = average rate sensor measured roll angle of rotation for the four experiments

Y_{mp} = average rate sensor measured pitch angle of rotation for the four experiments

Y_{my} = average rate sensor measured yaw angle of rotation for the four experiments

A matrices (as seen in equation (4.3.2)) were calculated for both sets of rate sensors. The results of these calculations can be seen in equations (4.3.3) for

Table 4.3: Rate sensor biases for different temperatures

Temperature (°C)	**30**	**35**	**40**	**45**	**50**
Rate sensor bias : $(10^{-3} \times \text{rad/s})$					
Roll 1	3.88	8.75	9.57	13.08	19.39
Roll 2	-5.31	-11.35	-16.49	-21.94	-26.54
Pitch 1	5.94	12.20	17.92	25.32	29.68
Pitch 2	9.45	18.38	28.78	37.95	47.24
Yaw 1	0.82	1.33	3.33	5.13	4.09
Yaw 2	11.29	23.26	32.98	44.36	56.47

rate sensor set 1 and (4.3.4) for rate sensor set 2.

$$\mathbf{A_1} = \begin{bmatrix} 1.0035 & 0.0006 & 0.0128 \\ 0.0025 & 0.9986 & -0.0040 \\ -0.0315 & -0.0076 & 0.9940 \end{bmatrix} \tag{4.3.3}$$

$$\mathbf{A_2} = \begin{bmatrix} 1.0389 & -0.0042 & 0.0218 \\ -0.0020 & 1.0446 & 0.0000 \\ -0.0351 & -0.0019 & 0.9956 \end{bmatrix} \tag{4.3.4}$$

Temperature

Firstly the temperature output of the rate sensor needed to be calibrated. This is done by putting the rate sensors in a temperature controlled oven and capturing the temperature output data at different known oven temperatures. This data is then used to calibrate the temperature outputs of the rate sensors. Then the angular rate output data of rate sensors during these tests is used to calibrate the rate output bias offset due to temperature variation. Five tests were completed at 30 °C, 35 °C, 40 °C, 45 °C and 50 °C. The different rate sensor biases for each test at a fixed temperature is given in Table 4.3.

Temperature calibration is essential for satellite applications due to the varying temperature in the space environment. The bias offset variation was found to be in the order of 1.2×10^{-3} rad/s for a variation of 1 °C as seen in Table 4.4.

Table 4.4: Rate sensor drift with temperature change

Rate sensor	Roll 1	Roll 2	Pitch 1	Pitch 2	Yaw 1	Yaw2
Bias drift: $(10^{-3} \times \text{rad/s per } ^\circ\text{C})$	0.78	-1.06	1.19	1.89	0.16	2.26

Allan Variance

After performing the axis calibration tests, the bias drift of the Analog Devices rate sensor was found to be relatively large (in the order of 150 $^\circ/h$) and therefore it needed verification that this bias drift was in fact due to the bias instability of the rate sensor. This procedure will be explained in the next paragraph.

Bias drift can be modeled as random walk, in other words the integration of white noise. For a signal composed of a random walk process with additional white noise added (which is the case with the rate sensor signal), over a short period of time the measured variance of the signal will be dependent on the added white noise. However, over long periods of time, the random walk process will begin to dominate. Allan Variance is a method of extracting the variance of the white noise process driving the random walk, as well as the variance of the added white noise. This is done be calculating the variance of the sampled data as a function of averaging time. Time variance (TVAR) is a form of Allan Variance (Cropp *et al.* [6]) and for discrete signals the TVAR is the variance of the double difference of the mean of a block of data (as seen in equation (4.3.5)).

$$\sigma^2_{\bar{x}} = \frac{1}{6\,(N-2)} \sum_{i=0}^{N-3} \left(\left(\Delta^2 \bar{x}_i \right)^2 \right) \tag{4.3.5}$$

Where,

$$\Delta^2 \bar{x}_i = \bar{x}_{i+2} - 2\bar{x}_{i+1} + \bar{x}_i$$

The Allan Variance (as seen in equation (4.3.6)) technique as explained by Bijker [3] was used in this project. It was used to determine the angle random

walk and the rate random walk of each of the rate sensor outputs.

$$\sigma_A^2(T) = \frac{1}{2(N-1)} \sum_{k=1}^{N-1} \left(y(k+1) - y(k)\right)^2 \tag{4.3.6}$$

Where,

$$\begin{aligned}
y(k) &= \frac{1}{n} \sum_{i=(k-1)n+1}^{kn} x(i) \\
x(k) &= \text{data points spaced by } T_s \\
T_s &= \text{Sample time} \\
T &= nT_s \\
&= \text{the bin size (in seconds) into which the data is divided} \\
n &= \text{the number of data points over which} \\
&\quad \text{the average values were calculated} \\
N &= \text{the number of complete bins which fit into the data}
\end{aligned}$$

The relationship between the Allan variance and the power spectral density of random processes (as seen in equation (4.3.7)) was used to determine the power spectral density of the rate sensor signal from its Allan variance (Bijker [3]).

$$\sigma_A^2(T) = 4 \int_0^\infty S(f) \frac{\sin^4(\pi f T)}{(\pi f T)^2} df \tag{4.3.7}$$

where $S(f)$ is the power spectral density (PSD) of a random process.

Rate sensor measurements were taken under certain fixed circumstances. The rate sensor outputs must be stabilized (so as to eliminate the initial conditions) and the rate sensor system must remain stationary. The Allan Variance technique was used to characterise the noise on the rate sensor output signals. According to Bijker [3] the uncertainty in the sensor data can be assumed to be generated by noise sources of specific character, as given below:

1. Angle random walk
2. Rate random walk
3. Bias instability
4. Quantisation
5. Drift rate ramp

As stated in Bijker [3], the first two noise sources will dominate the noise on MEMS devices. Therefore only these noise sources will be examined.

Angle random walk: The angle random walk is the measurement noise on the rate sensor outputs which causes drift (random walk) on the integrated rate sensor output signal. This noise can be approximated as white noise with a angle random walk spectral density coefficient, Q, where the PSD is given as:

$$S_{ARW}(f) = Q^2 \tag{4.3.8}$$

Substituting equation (4.3.8) into equation (4.3.7) (Bijker [3]):

$$\sigma_{ARW}(T) = \frac{Q}{\sqrt{T}} \tag{4.3.9}$$

Where the units of Q will be $\mathrm{rad/s}/\sqrt{Hz}$.

Rate random walk: The rate random walk drift on the rate sensor outputs due to temperature differences and other external interferences. The PSD of this noise is given in equation (4.3.10).

$$S_{RRW}(f) = \left(\frac{K}{2\pi f}\right)^2 \tag{4.3.10}$$

Substituting equation (4.3.10) into equation (4.3.7) (Bijker [3]):

$$\sigma_{RRW}(T) = K\sqrt{\frac{T}{3}} \tag{4.3.11}$$

Where the units of K will be $\mathrm{rad/s^2}/\sqrt{Hz}$.

Graphical representation: The calculated Allan deviation can be plotted against averaging time on a log-log scale along with equations (4.3.9) and

(4.3.11) which will appear as straight lines with inverse gradients. An example of the Allan deviation vs averaging time plot for each of the rate sensor outputs can be seen in Figure 4.6. The asymptote with the negative slope is used to calculate the angle random walk value and the asymptote with the positive slope, the rate random walk value. From this graph the values of Q and K can be determined using equations (4.3.9) and (4.3.11). For short window times, the angle random walk will be the most significant in the Allan deviation value. These values will decrease for longer window times due to the average being taken over more samples. At a certain point, the Allan deviation will increase when the rate random walk is starting to dominate.

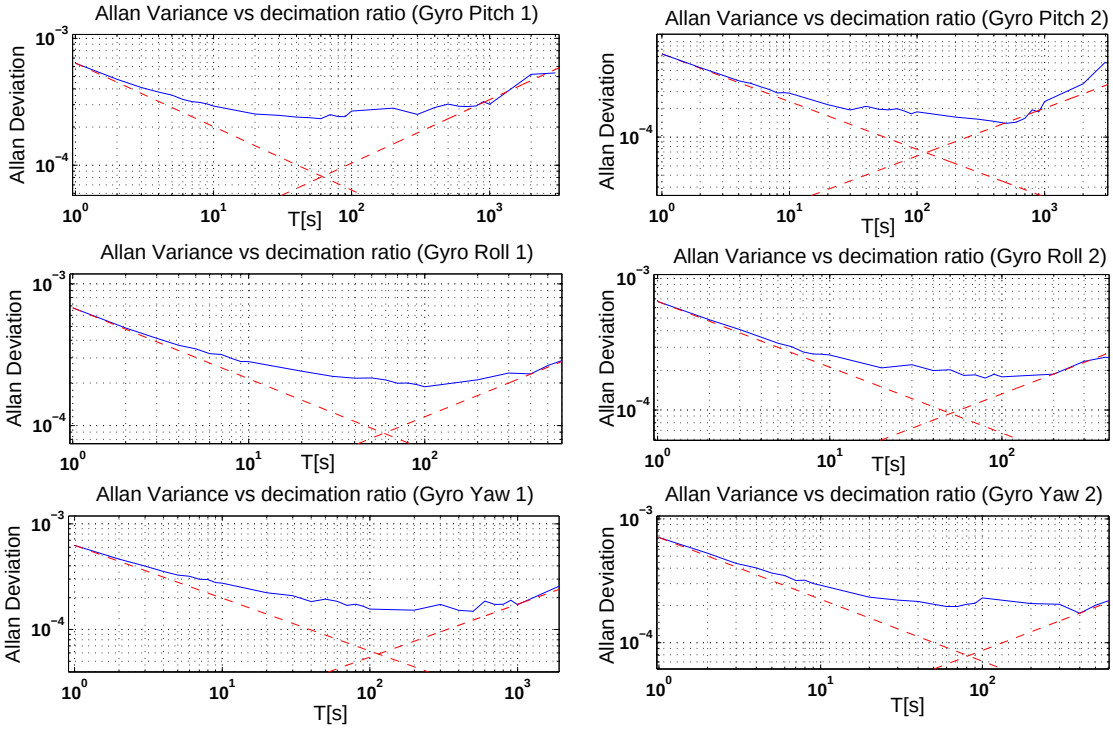

Figure 4.6: Allan Deviation vs averaging time

Initial conditions

The rate sensors used display an initial transient condition where, due to the heating of the sensor internally, the biases of the output signals drift in a certain direction. As previously stated the power resources on a nanosatellite

are very limited. Therefore the rate sensors will only be switched on for very short periods of time. The initial transients of each of the output signals was thus recorded and will be used to calibrate the rate sensor outputs in the initial state just after the power to these sensors has been switched on.

4.4 Integration

The integration of the reaction wheel system and the rate sensor system with a hardware-in-the-loop (HIL) Simulink simulation will be discussed in this section.

4.4.1 Reaction wheel system integration

The following parts of the reaction wheel system needed to be integrated with each other: The structure, BLDC motors, the rotors, reflective optical sensors and motor drive electronics and the 8051 microcontroller.

The reflective optical sensors were tested along with the 8051 microcontroller to ensure that the correct angular velocity reading is calculated by the microcontroller. The direction of angular rotation must be derived from the rotational speed readings using a predictive algorithm implemented on the microcontroller. This algorithm uses the current and previous wheel speed measurements to predict the wheel speed direction changes. This derivation is needed, because the reflective optical sensor only has one output which is high for a reflective surface and low for a non-reflective surface. No encoding therefore exists to extract directional information.

When the rotors were integrated with the system and tested at a rotational speed of more than 3000 rpm it was found that the vibrations due to unbalanced rotors were significant and problematic for this application. Under such circumstances the possibility exists of damaging the electronics and sensitive sensors. It was therefore required to balance the brass rotors. It was done using a simple technique of adding a small weight iteratively to the rotor at different locations until the vibration was minimized. A hole of the same mass as the balancing mass was then drilled on the opposite side of the rotor. This process was repeated if the result was not satisfying until the vibration was significantly damped at a rotational speed of 5000 rpm.

The integration of the structure with the PCB hosting the motor drive electronics and the 8051 microcontroller, required a mounting plate, designed to be as light as possible, but strong enough to withstand the vibrations during launch. The mounting plate was machined from 1.6 mm aluminium, but further research might show that a thinner aluminium plate may be sufficient.

4.4.2 Reaction wheel system and rate sensor system integration

The I^2C communications interface of the 8051 microcontroller was required to enable reception of the rate sensor data from the AtoD converter. A rate sensor measurement update is sent to the microcontroller every 10 ms. This data is then sent to the ground test computer via the UART interface. The raw data is sent to the computer and it is therefore not calibrated in the 8051. The main gyro board is supplied with 5 V and 3 V from the reaction wheel system PCB. During this integration step it was also required to verify that the 8051 microcontroller is capable of executing all the software tasks timeously (this includes I^2C, SPI, UART communication and the rotor speed calculations). This was verified by using another timing device to determine the time between wheel speed control intervals which was found to be 10 ms as expected.

Chapter 5

Software Design

This chapter will discuss the software design for this project. At first a brief overview of all the microcontroller software tasks will be given along with a flow chart. Thereafter a detailed area of the software design will be discussed, namely the implementation of the wheel speed control algorithm.

5.1 Microcontroller code implementation

The main tasks of the 8051 microcontroller can be divided into 5 parts: The rotational speed calculation and speed control of each of the 4 rotors, the I^2C communication with the AtoD (which converts the rate sensor data), the SPI communication with the DtoA (which converts the reference voltage for the BLDC controllers) and the UART communication with the ground test computer (which is used to send speed reference commands and receive rotor speed and rate sensor data). In this section brief commentary will be given on the implementation of each of these tasks and which microcontroller resources were used to fulfill these tasks.

5.1.1 Rotational speed calculation

To be able to determine the rotational speed of each of the rotors the pulses from each of the reflective optical sensors need to be counted. A time reference is also needed to determine how many pulses are recorded in a certain time. One of the 8051 timers are used for this purpose, it generates an interrupt every 100 ms. Timers 2, 3, 4 and the programmable counter array (PCA) timer are used as counters to count the pulses from the reflective optical sen-

sors. The values stored in the counters are used every 100 ms to determine the rotational speeds of each of the rotors.

5.1.2 Speed control

The speed control implemented on the 8051 microcontroller is explained in section 5.2. The speed loop is closed at 10 Hz. Additional checks are implemented in the controller to ensure that variable overflows do not cause faulty calculations. For this reason saturation checks of certain variables are implemented. The maximum torque requirement and angular momentum which is applicable for this project is also taken into account in the controller.

The wheel speed sign is determined by the controller onboard the 8051. The previous speed reading is used together with the new reading to determine whether the wheel speed is decreasing or increasing. When the wheel speed is around zero this information is used together with the wheel speed reference to identify the changes in the wheel speed direction, seeing that the reflective optical encoder only supplies magnitude readings and not direction.

When the wheel speed is below a certain threshold and the wheel speed reference is zero the current reference to the BLDC controller is zeroed. The static friction is estimated using the minimum current reference which puts the wheel into motion. The maximum torque command incorporates the motor friction to ensure that the true maximum torque output of the BLDC motor reaches the torque specification. The kinetic friction is assumed to be much smaller than the static friction.

5.1.3 I^2C communication

The I^2C clock frequency is set at 220 kHz. This is done according to the minimum low and high times for the I^2C clock as specified by the AtoD converter. There are twelve 12-bit values to be transmitted every 10 ms. This means that 24 data bytes (2 bytes per sampled channel) are needed to transmit the rate sensor data and one additional byte is needed to transmit the slave address of the AtoD converter. Between each transmitted byte there is an 18.2 μs conversion period in which the AtoD converter converts the analog voltage.

This means that one transmitted byte along with the acknowledge bit and the conversion time effectively takes 59 μs. Thus sending the 12 channels of converted rate sensor data over the I^2C connection takes 1.48 ms. Seeing that this bundle of data is only sent every 10 ms, the I^2C bus is sufficiently fast. The other limiting factor is the fact that the I^2C communication takes some of the 8051 processing time each 10 ms and therefore should be as short as possible. A moving average filter is used to filter the data which is received from the AtoD converter. The output of the filter now has a frequency of 10 Hz, and the data can be sent to the ground test computer along with the wheel speed measurements.

5.1.4 SPI communication

The SPI communication is set up according to the specifications of the DtoA converter. The maximum SPI clock frequency specified by the DtoA converter is 50 MHz, but it was decided that a clock frequency of 2 MHz is sufficient. This decision was based on the fact that four 16 bit words needed to be sent in 100 ms (one analog voltage reference for each BLDC controller). This amounts to 32 μs of transmitting time, which is less than 0.04% of the 100 ms period. The SPI interface on the microcontroller side is set up to be in 4-wire master mode. This means that it is configured to have Master out Slave in (MOSI), slave select (NSS) and serial clock (SCK) outputs and a Master in Slave out (MISO) input.

5.1.5 UART communication

The UART is configured to operate at 19200 baud. Each 100 ms 24 bytes of rate sensor data and 20 bytes of wheel velocity data are sent via the UART interface and four wheel speed references can be received. This amounts to a total of 53 bytes (with protocol implementation characters) which need to be sent each 100 ms. A maximum of 24 bytes of wheel speed reference data can also be received each 100 ms. The UART interface is implemented using interrupts, which means that while there is no data to send or receive the processor is free to process other tasks, it does not need to poll for data on a fixed time basis.

5.1.6 Flow chart overview

A flow chart depicting the sequence of tasks completed by the microcontroller is shown in Figure 5.1. It gives a brief overview of the sequence of tasks which need to be executed by the 8051 microcontroller. The flow chart shows the initialization stage and the main execution loop. The reaction wheel speed control loop block will be discussed in more detail in section 5.2.

5.2 Implementation of wheel speed control algorithm

A proportional-integral (PI) controller is implemented on the 8051 microcontroller to control the wheel speeds of each of the four reaction wheels. The form of the controller can be seen in equation (5.2.2). As stated previously, the current loop is closed inside the BLDC controllers, it is assumed to be much faster than the speed loop, which is closed at 10 Hz. Therefore the current loop can be approximated using only an open loop gain (K_{OL}) and an integrator. This was confirmed to be a valid approximation through practical measurements. Therefore only the open loop gain had to be determined to complete the model of the current loop (see equation (5.2.1)).

$$\begin{aligned} G_{OL}(s) &= \frac{K_{OL}}{s} \\ G_{OL}(z) &= \frac{K_{OL}T_s}{z-1} \end{aligned} \tag{5.2.1}$$

$$G_{PI}(z) = \frac{K_p(z-a)}{z-1} \tag{5.2.2}$$

This PI controller can now be written as a difference equation in the time domain as in equation (5.2.3). This controller will then be implemented in the microcontroller, with the controller gains K_1 equal to K_p and K_2 equal to $K_p a$.

$$u(k) = u(k-1) + K_p e(k) - K_p a e(k-1) \tag{5.2.3}$$

The process of calculating the closed loop transfer function (of the speed loop) can be seen in equation (5.2.4). The poles are placed according to the design specifications, with a damping factor of 0.9 and a five percent settling time of 0.53 s. This means that the poles of the second order system will lie at $-5.65 \pm 2.74i$ in the s-plane. The controller gains, K_1 and K_2, can then

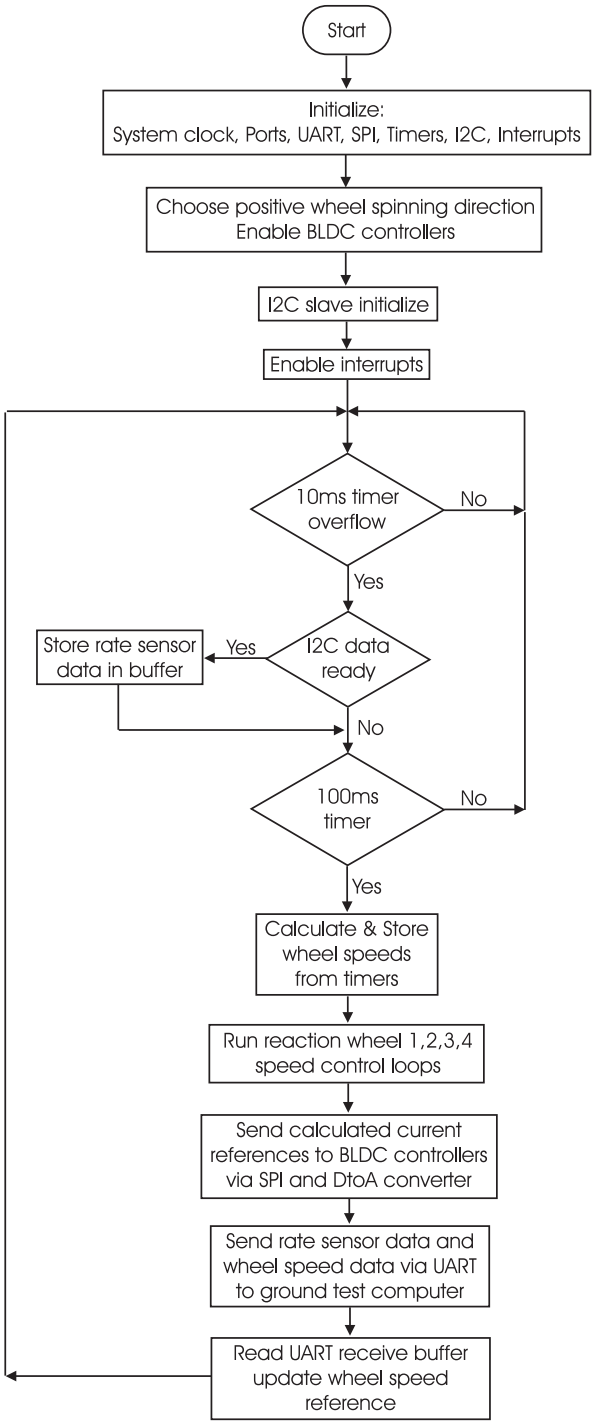

Figure 5.1: Flowchart of the tasks executed by the microcontroller

calculated as 11.12 and 8.31 respectively using equation (5.2.4) and the time domain specifications.

$$\begin{aligned} G_{CL}(z) &= \frac{\frac{K_p(z-a)}{z-1} \times \frac{K_{OL}T_s}{z-1}}{1 + \frac{K_p(z-a)}{z-1} \times \frac{K_{OL}T_s}{z-1}} \\ &= \frac{K_{OL}T_sK_p(z-a)}{z^2 - \left(2 - K_{OL}T_sK_p\right)z + \left(1 - K_{OL}T_sK_pa\right)} \end{aligned} \tag{5.2.4}$$

Chapter 6

Results

In this chapter the outcomes which have been achieved will be discussed. Explanations will also be given for the goals which could not be reached. The first section in this chapter will give some simulation results which can be compared to the real system at a later stage. Thereafter the reaction wheel system in the simulation will be replaced with the real system and the results of the hardware-in-the-loop tests will be shown. Lastly the results using the experimental setup controller, designed to use the rate sensor feedback to control the reaction wheel system, will be discussed.

6.1 Simulation Results

In this section the results from the simulation as discussed in Chapter 3 will be given. Firstly it will be demonstrated that the PD controller implemented performs as expected. Thereafter the inclusion of disturbance torques into the simulation will be motivated and lastly the effectiveness of the momentum dumping will be discussed.

6.1.1 PD controller

This section discusses the results of the PD satellite attitude controller as explained in section 3.3. The results which will be presented in this section were obtained using the controller gains as stated in equation (6.1.1). The algorithms for the controller gains in section 2.2.2 are repeated here to show

how they were calculated.

$$\begin{aligned} t_{s\,5\%} &= 15s \\ \zeta &= 0.8 \end{aligned}$$

Therefore,

$$\begin{aligned} \omega_n &= 0.25 \\ K_P &= 2\omega_n^2 \\ &= 0.125 \\ K_D &= 2\zeta\omega_n \\ &= 0.4 \end{aligned} \tag{6.1.1}$$

Figure 6.1 shows that the reference attitude of the satellite is followed with a 5% settling time of 13.85 s. In this example a reference roll angle of 30 degrees has been chosen. It can be seen that the actuators control the satellite to follow this reference angle with little or no overshoot. The resulting five percent settling time of 13.85 s is 1.15 s less than the specified settling time of 15 s. This is due to the fact that the three-axis quaternion feedback controller is not linear. Similarly it can be shown that pitch and yaw reference angles will be followed.

Variable limiter attitude error feedback results

The results for the improved PD controller (as discussed in section 3.3.1), which implements a variable limiter for the attitude error feedback, will be presented in this section. Figure 6.2 shows the different responses of the two controllers. It shows that the controller which implements the limited attitude error feedback has an improved transient response during large maneuvers. For small angle maneuvers the two controllers, however, perform similarly. It was therefore decided to use the simple PD controller (without the attitude error limiter) in practise, because the responses of the two controllers are equivalent for maneuvers up to 90 degrees. The added complexity of the improved controller is also undesirable for this application.

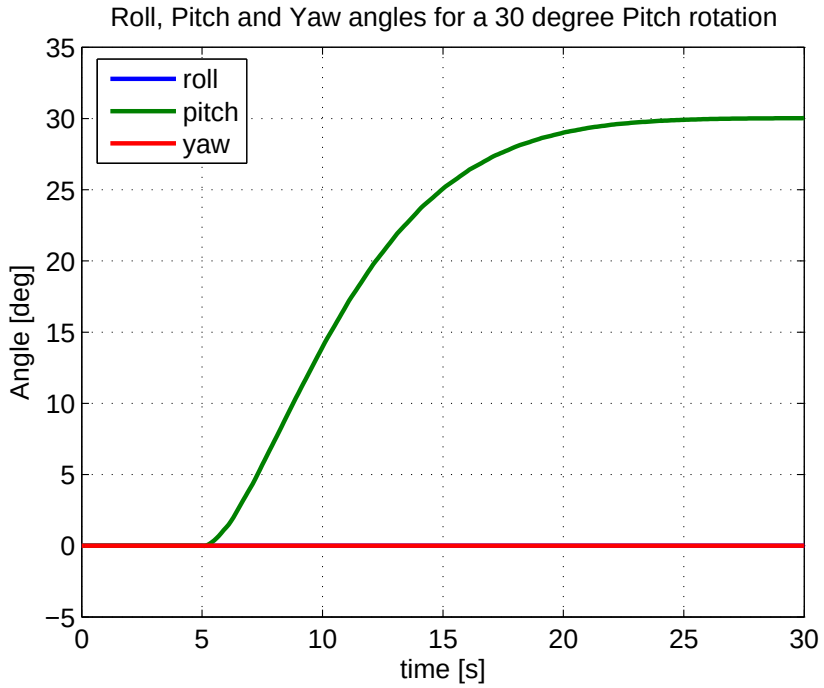

Figure 6.1: Simulation Result - reference attitude

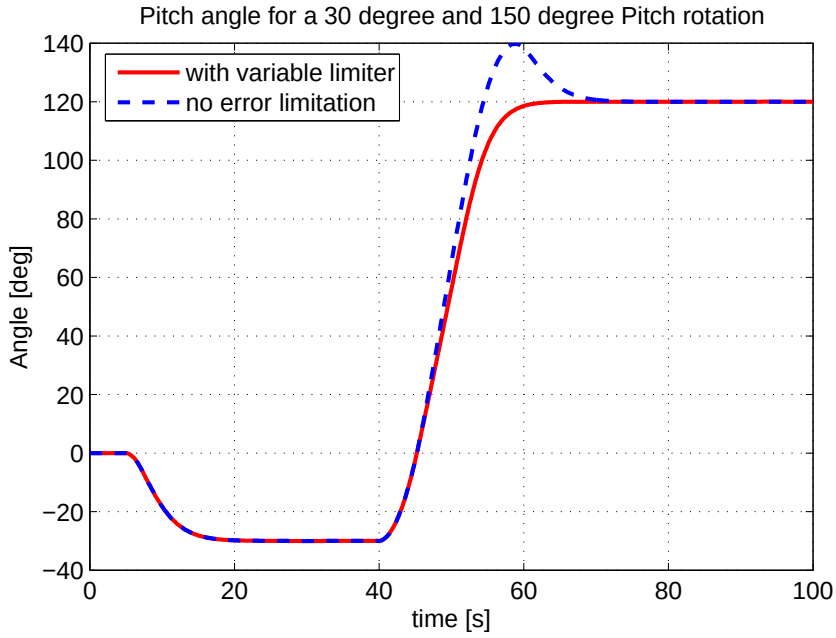

Figure 6.2: PD controllers with and without attitude error limitation compared

6.1.2 Disturbance torques

Constant disturbance torques in the order of 10^{-7} Nm were applied to the satellite in the x- and y-axis and 10^{-8} Nm in the z-axis in the simulation to show the effect of the momentum dumping ($N_d = \left[10^{-7}\, 10^{-7}\, 10^{-8}\right]^T$ Nm). The disturbance torques are dominated by the gravity gradient torque for satellites where the moment of inertia in the z-axis is different to the x- and y-axis. The disturbance torque used in the simulation was therefore calculated using the worst case gravity gradient torque calculation as shown in equation (6.1.2). The satellites altitude was taken as 600 km and its moments of inertia as discussed in section 3.1.1 ($I_x = I_y = 0.14$ kgm^2, $I_z = 0.2$ kgm^2).

$$T_g = \frac{3\mu}{2R^3}\left|I_z - I_y\right| \sin(2\theta) \tag{6.1.2}$$

Where,

T_g = Gravity gradient torque

μ = Earth's gravity constant $\left(3.986 \times 10^{14}\, m^3/s^2\right)$

R = Orbit radius (from centre of earth) [m]

θ = maximum deviation of the z-axis from the local vertical (worst case: 45 degrees) [rad]

6.1.3 Momentum dumping results

The fact that momentum dumping can only be done when the angular momentum vector and the magnetic field vector of the earth are not in the same direction is verified by Figure 6.3. The maximum momentum is dumped between 4000 s and 6000 s, when the magnetic field vector is more favourable to generate a torque to dump the angular momentum. Figure 6.3 shows the angular momentum of the reaction wheels in spacecraft body coordinates over a period of 8000 seconds while momentum dumping is implemented. The period of one orbit is about 6000 seconds, therefore the periodic influence of the earth's B-field on the dumping efficiency can be seen clearly. Figure 6.3 therefore proves that momentum dumping as implemented in the simulation, works effectively.

The results shown in Figure 6.3 can be compared to the case where no momentum dumping was implemented, as shown in Figure 6.4. The angular

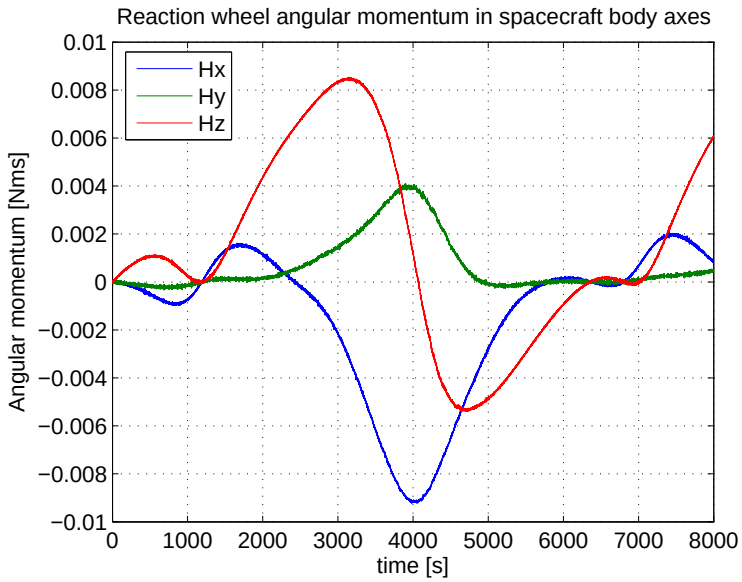

Figure 6.3: Simulation Result - Momentum Dumping

momentum buildup due to constant external disturbances is evident. The need for momentum dumping to be implemented is therefore clear.

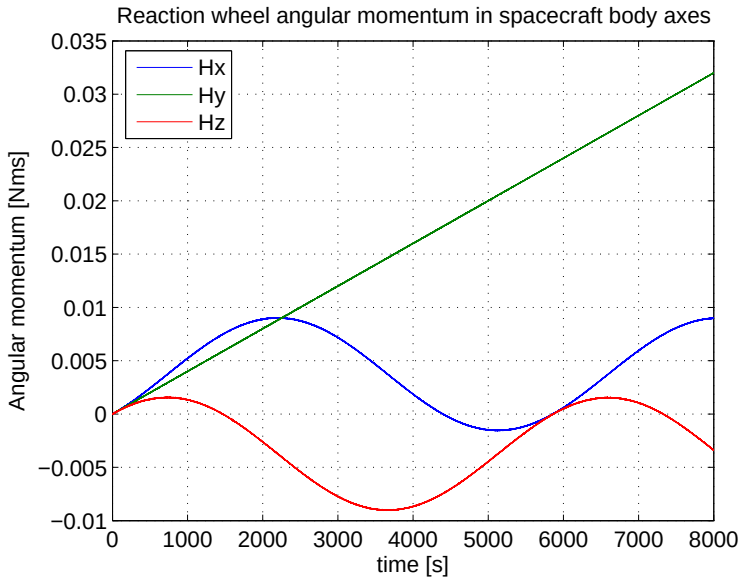

Figure 6.4: Simulation Result - No Momentum Dumping implemented

6.2 Hardware-in-the-loop

The hardware-in-the-loop (HIL) simulation has one main objective, to prove that the speed control loop implemented on the 8051 microcontroller behaves as expected. This is done by comparing the angular velocity outputs of the reaction wheels to the angular velocity outputs of the reaction wheel model, while both the model and the real system are receiving the same inputs. This will also serve as a method of verifying the accuracy of the reaction wheel model.

In this chapter the changes made to the simulation as discussed in chapter 3 will be discussed. Then the interfacing between the Simulink simulation and the 8051 microcontroller will be explained. Lastly this chapter will give a summary of the results obtained from the hardware-in-the-loop tests.

6.2.1 HIL Simulation

Figure 6.5 presents the Simulink simulation model as used in Chapter 3. The model has been changed to run the actual reaction wheel system in parallel with its model to enable a comparison of their outputs and to verify the accuracy of the model. The HIL block is an S-function block which contains the C code used to implement the communications protocol between the Simulink simulation and the 8051 microcontroller. The inputs to the HIL block are the wheel angular velocity references for each reaction wheel and the outputs are the angular velocities measured from every reaction wheel.

Other than the added HIL block, convertion gains were required to convert from the angular momentum reference output of the PD controller to the wheel speed reference in rpm which is sent to the microcontroller. A convertion method was also required for the wheel speed measurement, coming from the microcontroller, to the wheel angular momentum and torque input of the satellite model. The disturbance torques were removed from the simulation along with the magnetic control implementing momentum dumping. Seeing that the speed loop controller uses speed references in rpm units the angular momentum reference values used in the simulation needed to be converted to angular velocity values and scaled to the correct units. This was done by firstly dividing the angular momentum values by the moment of in-

ertia of the rotors and then converting them from rad/s units to rpm units.

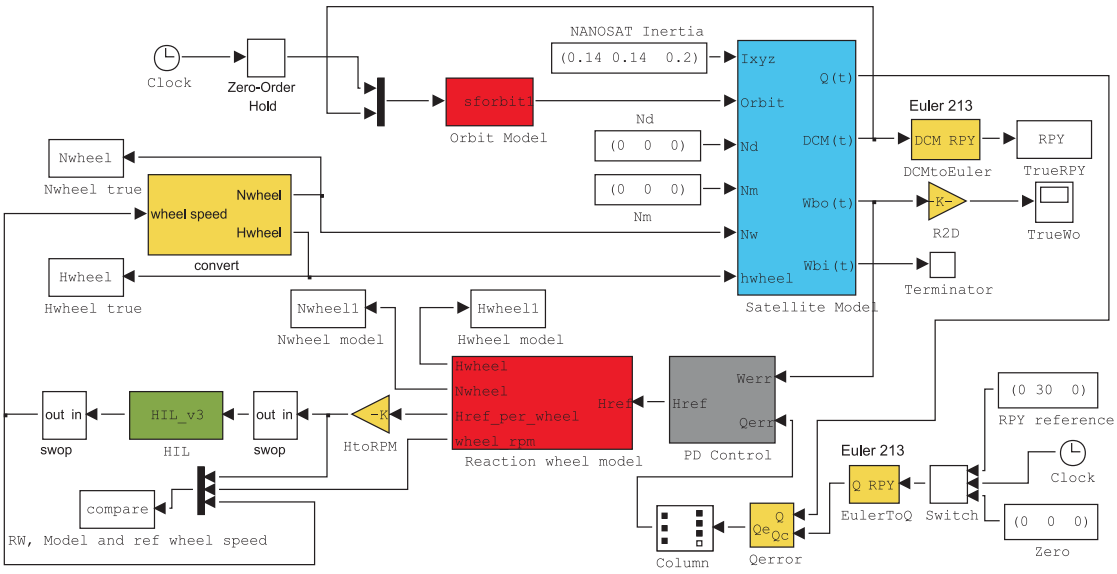

Figure 6.5: Hardware-in-the-loop

The control of the actual reaction wheel system in this HIL simulation was firstly done in an open loop fashion, using the reaction wheel system model outputs as feedback to the satellite model. This was done to determine whether the actual reaction wheel system was modelled accurately enough. The only objective at this stage was therefore to compare the reaction wheel model and the actual reaction wheel outputs.

6.2.2 Communications protocol

The protocol implemented to communicate between the ground test computer and the 8051 microcontroller was designed to use ASCII characters to represent the speed data, the direction of rotation and the reaction wheels number. The contents of a single data packet is explained in Figure 6.6. This was done in order to be able to interpret the ascii data without conversions being necessary. Each wheel speed was also preceded by a unique character to relate it to the specific wheel. The speed reference command sent to the wheel microcontroller implements an absolute wheel speed command and a

direction of rotation for each wheel. A current reference command was not needed for this application and was therefore not implemented.

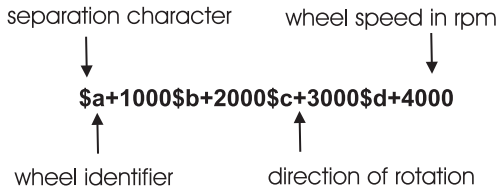

Figure 6.6: Communications protocol implementation

6.2.3 HIL results

Before the hardware-in-the-loop simulation could be implemented it was necessary to prove that the reaction wheel model resembled the true reaction wheel with small enough modelling errors to be able to insert the hardware into the control loop. This was done by sending the same angular velocity reference to both the reaction wheel model and the true reaction wheel. The angular velocity, angular momentum and torque outputs of the model and the true system were compared. The results, as seen in Figure 6.7, showed that the reaction wheel model was accurate enough to proceed with the hardware-in-the-loop simulation. The small differences between the model and the true reaction wheel outputs still eminent are due to the fact that the effects of wheel friction (and air friction) are not included in the model of the reaction wheel. That is why the model angular velocities display more overshoot at some stages during the simulation.

The reaction wheel model was then replaced by the actual reaction wheel in the control loop. To compare the difference between the reaction wheel and its model, a 30 degree pitch rotation was commanded using the actual reaction wheel and the model in two separate simulations. The result is shown in Figure 6.8. Figure 6.8 shows very small differences in the 30 degree reference step response. These differences are due to small modelling errors (as explained above), seeing that identical satellite attitude controllers were used in both simulations. The HIL simulation results showed a five percent settling time of 13.6 s. The response when the model of the reaction wheel was used for feedback showed a five percent settling time of 13.9 seconds. It can

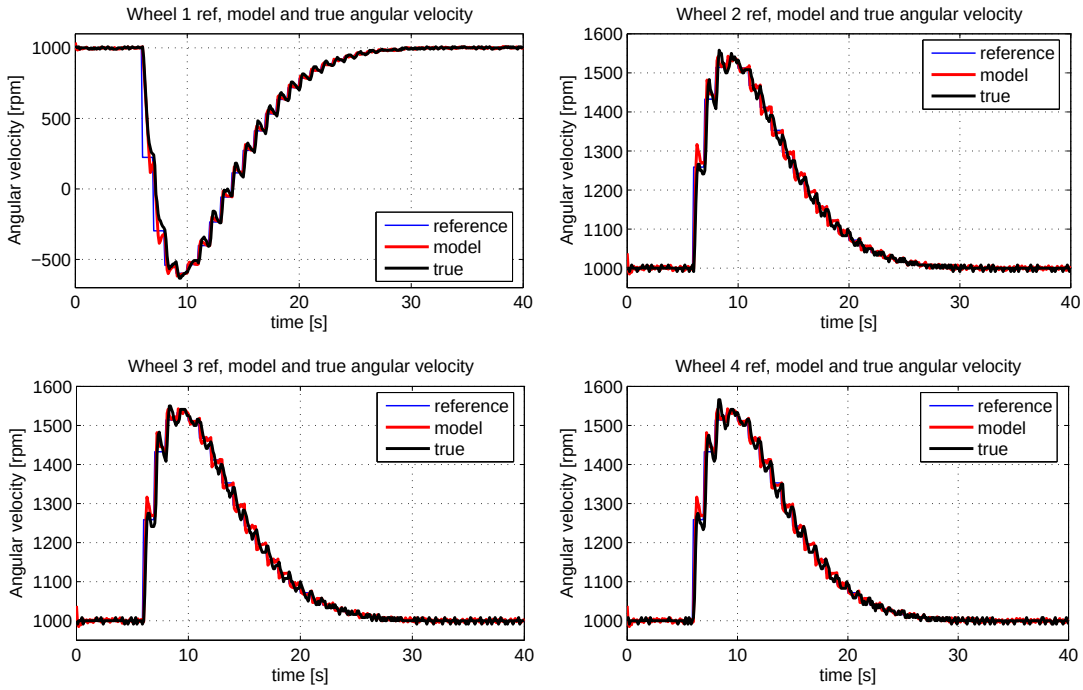

Figure 6.7: Model and true RW system compared

therefore be seen that the results obtained from the two simulations (using the model and the actual reaction wheel system for feedback) are very well related. This also proves that the initial specification, requiring a 30 degree rotation to be completed in less than 60 seconds, is satisfied in the simulation.

Figure 6.9 shows the angular velocity of the reaction wheel system compared to its model in the simulation with a 30 degree pitch reference step, during a hardware-in-the-loop simulation. The fact that Figure 6.9 and Figure 6.7 are quite similar is also an indication that the model of the reaction wheel is quite accurate. It is clear from Figure 6.10 that there are minor differences between the damping coefficients of the actual reaction wheel system and the model of the reaction wheel system. Smaller errors can be observed from the actual reaction wheel response for bigger angular velocity steps. The reasons for these differences will be discussed in section 6.4.1.

The angular momentum vector of wheel number one is aligned to the ver-

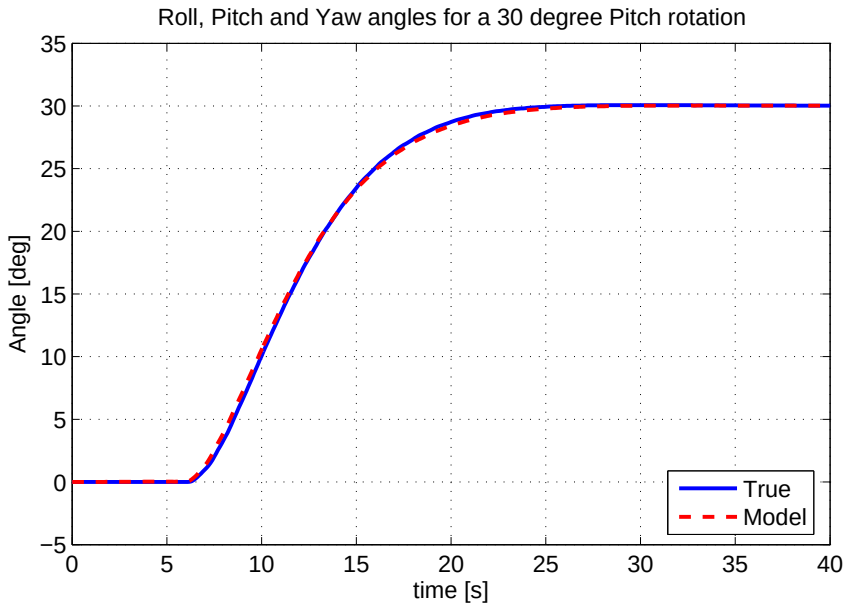

Figure 6.8: Angular displacement compared using Model and true RW system

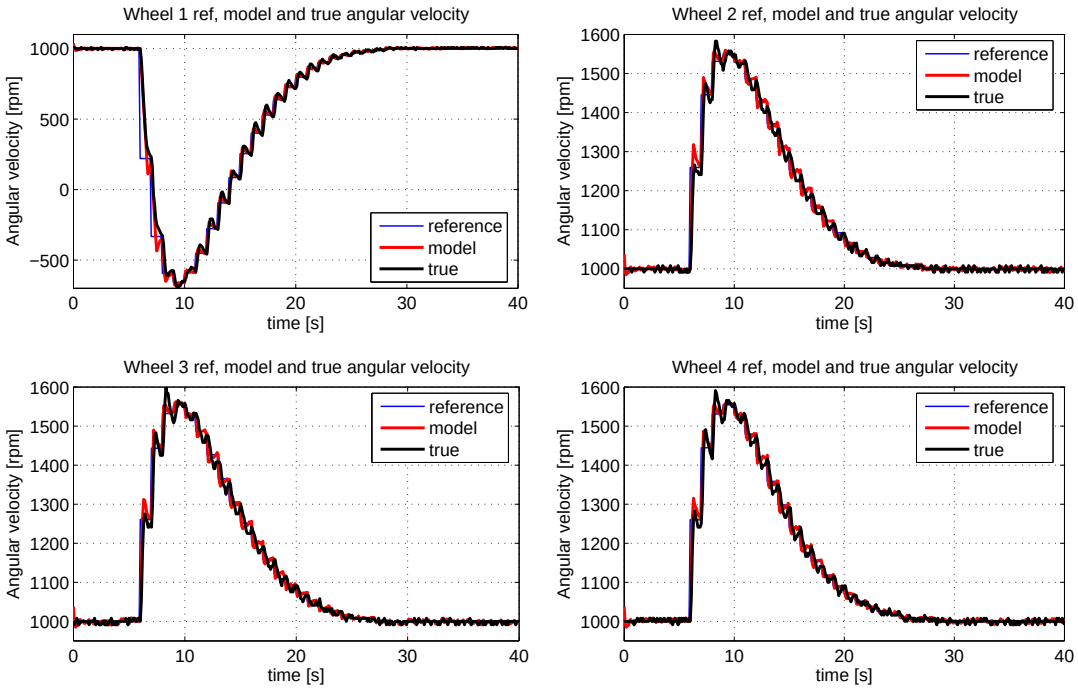

Figure 6.9: Hardware-in-the-loop results - 30 degree pitch rotation

tical axis (pointing downward) which is the pitch axis of the actual reaction wheel system. Wheels two, three and four are the wheels aligned at angles of 70.53 degrees from the upward pointing vertical. From Figure 6.9 it can be seen that the wheel one is accelerated in the opposite direction to wheels two three and four to create the angular momentum in the pitch axis which will turn the simulated satellite. The reaction wheel speeds converge back to 1000 rpm which means that the angular momentum exchange on the satellite will be transferred back to the reaction wheels bringing the satellite to a standstill at the end of the 30 degree pitch maneuver.

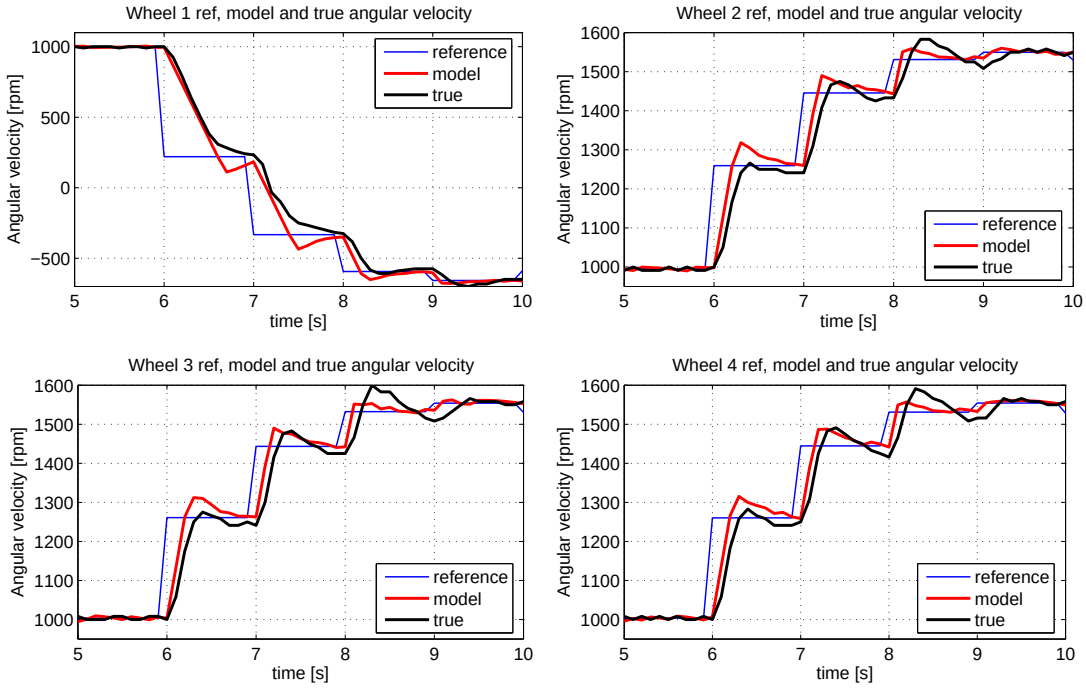

Figure 6.10: Hardware-in-the-loop results - 30 degree pitch rotation (zoomed in)

Figure 6.11(a) shows the torque results in the x, y and z-axis for the hardware-in-the-loop results. It is clear that the maximum torque of each of the four wheels is combined to give a torque vector of around 10 mNm in the pitch axis. Looking at the angular momentum in the x, y and z-axis in Figure 6.11(b) it can be seen that the pitch reference step causes the step in the angu-

lar momentum of the reaction wheels in the y-axis and then the gradual return to a zero angular momentum to bring the simulated satellite to a standstill after the rotation.

6.3 Power, Mass and Size Budgets

Power

The specification was to minimize the power consumption of each of the components used on the reaction wheel PCB as far as possible. Therefore components with a low current usage were chosen. Some components can also be switched off or switched to a low current state to save power. In Table 6.1 the maximum current usage of each of the components is shown according to the power supply voltage it uses. The table is divided into a section where the datasheet current usage values are given and a section where the measured values are shown. A total current usage for the total reaction wheel system is also given for each power supply. Due to the fact that the 5 V regulator is powered from the 12 V supply the current drawn by the 5 V regulator is included in the 12 V current usage. The same is true for the 5 V supply and the 3 V regulator.

Examining Table 6.1 reveals that the total power consumption (1.77 W) of the reaction wheel PCB is quite high for a nanosatellite application. The initial goal was for the power consumption to be less than 1 W in total. The only solution to this problem would be to lower the power supply voltage. Depending on the satellite bus voltage this would entail adding another voltage regulator which would add more power losses to the system. Tests were done with lower supply voltages of 9 V and 8 V which lowers the power consumption to 1.23 W and 1.09 W respectively.

Table 6.2 shows the total measured power consumption for the different operating conditions stated. For each condition the calculated and measured power consumption is given. The equation (B.0.1) used to calculate the power consumption for the different operating conditions is discussed in Appendix B. It can be seen that the calculated power consumption is lower than the measured power consumption for each of the operating conditions. This is

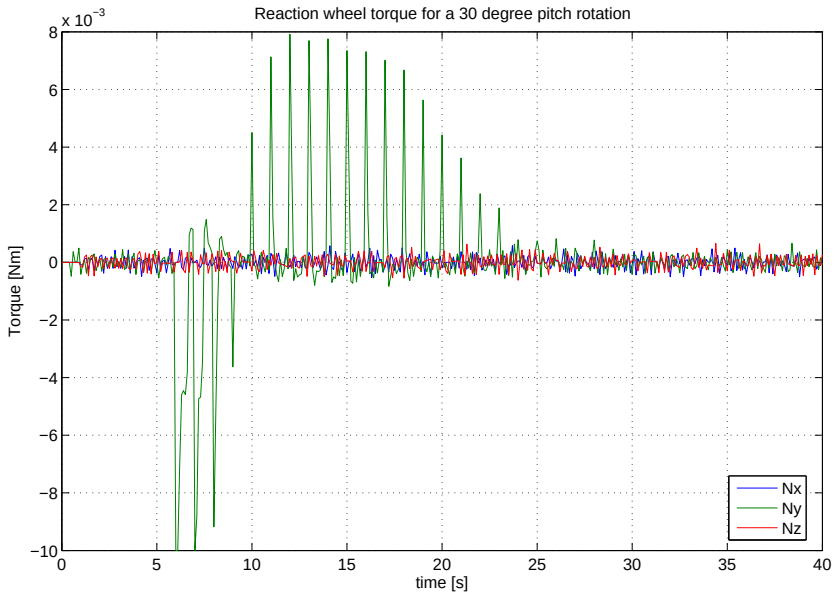

(a)

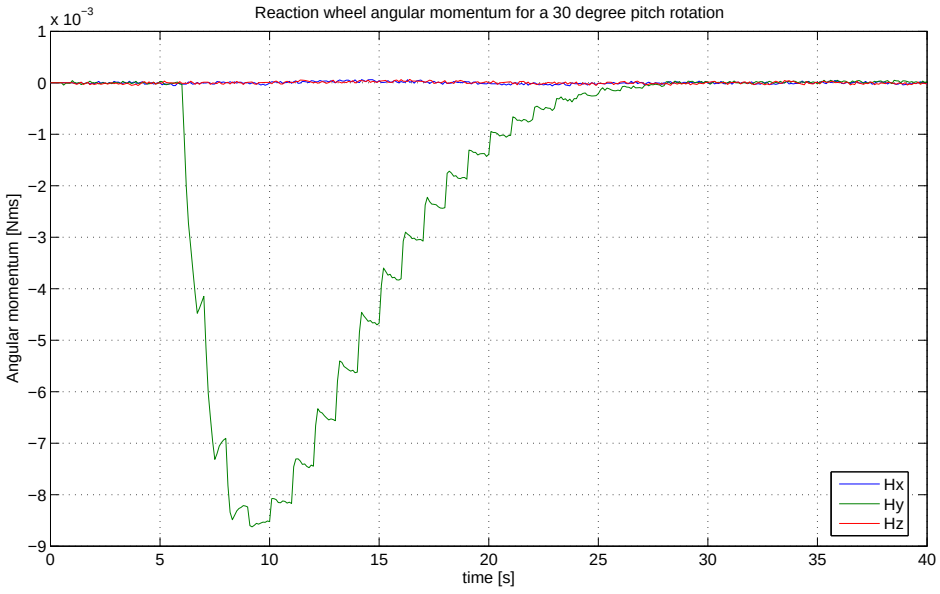

(b)

Figure 6.11: (a) The reaction wheel torque and (b) angular momentum in the x, y and z-axis during a 30 degree pitch maneuver

Table 6.1: Current usage of RW system

Component	**12V** $I_{usage}[mA]$	**5V** $I_{usage}[mA]$
Datasheet values (max):		
BLDC controllers	40	
5V regulator (I_Q)	7	
Optical sensors		60
DtoA converter		0.88
Current sensor		1.9
RS485 Tranceiver		0.5
RS232 Tranceiver		0.257
CAN Tranceiver		10
Measured values:		
BLDC motors (V_s)	36	
BLDC controllers	52	
8051 microcontroller		
Optical sensors		60
Total measured current usage:	147.6	101

due to the fact that the no load current specified in the datasheet is lower than the practical current drawn by each motor at a constant angular velocity. The reason for this difference is mainly air friction which influences the rotation of the rotor. The power consumption for the following conditions is shown in Table 6.2:

- All the reaction wheels are stationary
- All the reaction wheels rotate at a speed of 1000 rpm
- All the reaction wheels are at maximum acceleration (at 1000 rpm)
- All the reaction wheels are at maximum acceleration (at 5000 rpm)

Mass

The mass budget for the reaction wheel system is given in Table 6.3. As can be seen from Table 6.3 the maximum weight contribution comes from the rotors, which generate the angular momentum. Their weight can only be decreased by increasing their size, but because of the volume constraint the

Table 6.2: Measured power consumption of RW system

Condition	**Power usage** $[W]$ Measured	**Power usage** $[W]$ Calculated
4 wheels stationary	1.77	
4 wheels at 1000rpm	2.62	2.42
4 wheels (max accel, 1000 rpm)	11.77	10.5
4 wheels (max accel, 5000 rpm)	20.1	18.9

Table 6.3: Mass budget measured for RW system

Component	**Mass (g)**
Structure	110.11
Rotors	333.76
BLDC Motors	128
Optical sensors	4.6
Mounting plate	51.22
PCB	123.26
Total mass:	750.95

size of each of the reaction wheels is also limited. A compromise thus needed to be found for the optimal size and weight of the reaction wheels. The other significant contributions are made by the structure, the PCB and the BLDC motors. Further improvements can be made using 1.2 mm (or maybe even 0.9 mm) aluminium to manufacture the structure after verifying that it is rigid enough to withstand the vibration envorinment during launch.

Size

The size of the complete reaction wheel system is 110 mm by 110 mm by 130 mm high. The biggest contribution to the volume of the reaction wheel system is the structure, which was designed to be as small as possible to be able to house the BLDC motors on the inside. The depth and width of the system was minimized to the size of the PCB, which itself was designed to be as small as possible. The height of the system consists of the height of the tetrahedral structure, the aluminium plate standoffs connecting the structure to the base plate and the standoffs connecting the base plate to the PCB. The height of the aluminium plate standoffs can be reduced by 1 cm if they are redesigned to be the minimum height, which is the height of the

rotor. Other than that the reaction wheel system was designed to occupy the smallest possible volume.

6.4 Reaction wheel Measurements

This section will discuss some results regarding the reaction wheel system as a whole and how effective it would be to use in a nanosatellite. The section will also take the system requirements into account and discuss whether they have been satisfied. The different subsystems of the reaction wheel system will be discussed individually, and finally the system as a whole will be evaluated.

6.4.1 Wheel speed control system

The reaction wheel controller was evaluated by comparing the results of the reaction wheel model with that of the actual reaction wheel. The description of the reaction wheel model was done in section 3.1.3. An angular velocity reference step of 1000 rpm at 5 s and another 500 rpm at 10 s was given to each reaction wheel of the true system, and their corresponding models. The result is shown in Figure 6.12. It can be seen that the model and the true reaction wheel follow the reference with five percent settling times of 1.24 s and 1.15 s respectively. The other noticeable difference is the damping of the true reaction wheel system which is much larger than that of the model. This is due to the fact that the reaction wheel model does not incorporate wheel friction and air friction. The dynamic friction of each the BLDC motors have a damping effect on the step response. When the initial accelerations of the reaction wheel model and the true system are compared, they are found to be quite similar. These initial accelerations of the true reaction wheel and the model can be calculated from Figure 6.12 as 128.68 and 134.17 rad/s^2 respectively. This implies that the torque capability of each reaction wheel modelled is accurate. The 0.1 s delay between the reference and the model output is due to the fact that model output can only start changing after its input, the reference wheel speed, has changed. The fact that the true wheel speed is slightly smaller than the modelled wheel speed at any given time is due to wheel and air friction as discussed above.

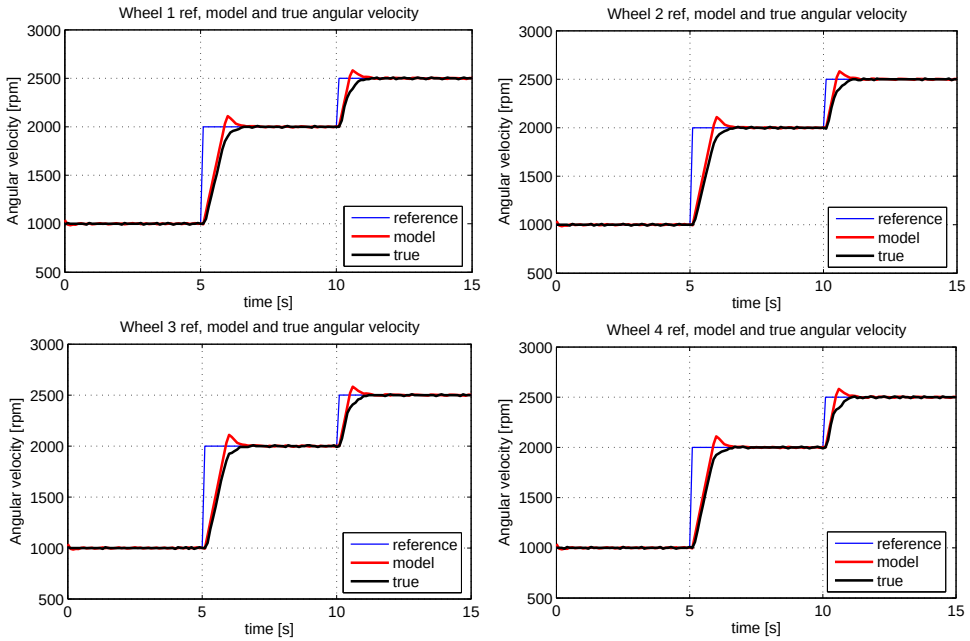

Figure 6.12: Model and true system comparison: 1000 rpm speed reference step

6.4.2 Reflective optical sensors

The reflective optical sensors have been found to be adequate for the purpose of wheel speed measurement. At the maximum wheel speed of 5000 rpm the sensor is required to measure 6000 pulses per second and it does so effectively. This means that the speed measurement resolution is 8.33 rpm when measurements are taken every 100 ms (as discussed in section 4.2.2). The only drawback of this sensor is its power consumption, it draws a minimum of 10 mA of current from the 5 V supply. When the resistor which limits the current to the infrared diode is increased the sensor fails to detect the slits in the rotor. The power consumption for these four sensors therefore amounts to 200 mW, which is problematic for a nanosatellite application due to the limited power available.

6.4.3 Rotor

The rotors are unbalanced due to their manufacturing which is done locally at a workshop at the university to save on manufacturing costs. The balancing of the rotors was also not done professionally, therefore small unbalances could still remain. For the non-reflective surfaces to be detectable by the opti-

cal reflective sensors a coating was required. This was done using an iodizing process which leaves a black residue. This proved to be a sufficient method in this application.

6.4.4 Microcontroller

The microcontroller needs to execute a few different tasks: Measuring and controlling each of the four wheel angular velocities, UART, SPI and I^2C communication, as stated previously. It was proven practically that the 8051 microcontroller has sufficient processing power to execute all these tasks.

6.5 Rate sensor results

This section contains analysed test data which will be used to determine the suitability of the Analog Devices rate sensors for space applications. Three sets of data were used to verify the accuracy of the results. The results from one set of data will be displayed in this section and the rest of the results from the second and third sets of data can be seen in Appendix C. Figure 6.13 shows the recorded data from the six rate sensor outputs while the sensors were at rest and kept at a fairly constant temperature.

The temperature influence will be discussed further in section 6.5.3. It is clear that the measurement noise is quite significant, this shows in the covariance results in section 6.5.4. The variance of the rate sensor outputs is in the order of 4×10^{-6} rad^2/s^2. The rate sensor outputs are firstly filtered using a passive low pass filter with a cutoff frequency of 20 Hz. Thereafter the analog signal, which is sampled every 10 ms, is converted to a digital signal using a 12 bit analog to digital converter. The digital signal is then filtered using a moving average filter, which means that the average of 10 samples is taken and the filtered rate sensor data is sent to the ground test computer every 100 ms.

6.5.1 Allan Variance results

The first of the tests was to calculate the Allan Variance of each of the rate sensor outputs. The seven hours of data as shown in Figure 6.13 was used for this calculation. The Allan Variance technique, as explained in section 4.3.3, was applied to retrieve the results as shown in Figure 6.14. The angle random

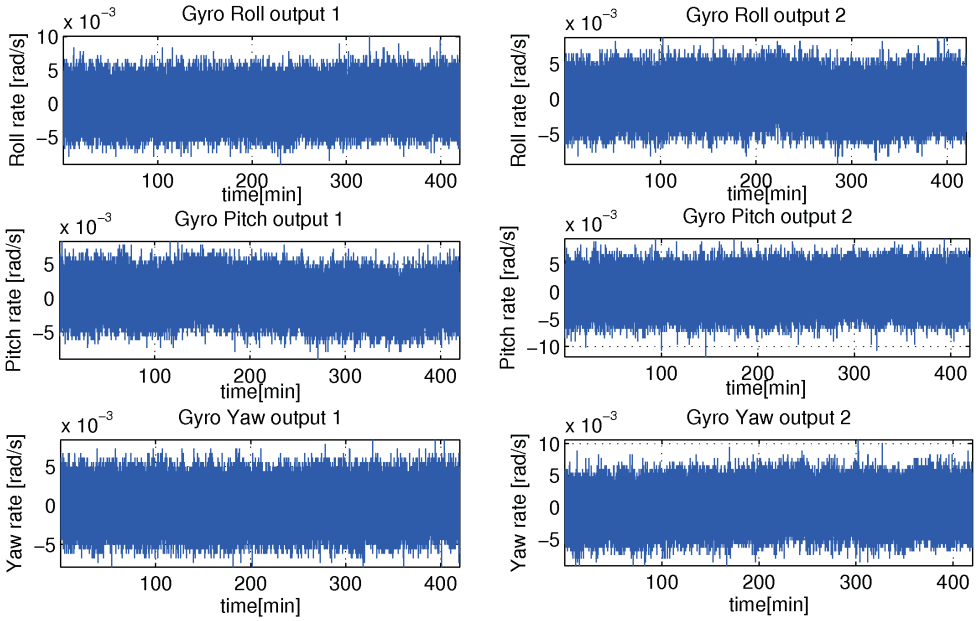

Figure 6.13: Rate Sensor outputs over 7 hours

walk (ARW) and rate random walk values for each sensor as shown in Table 6.4 can be calculated from the graphs in Figure 6.14. This is done by using equations (4.3.9) and (4.3.11) which represent the dotted lines on the left hand side and right hand side, respectively, in Figure 6.14. The value of the angle random walk can be obtained where the negative slope crosses $T = 1$ s and the value of the rate random walk can be obtained where the positive slope crosses $T = 3$ s. From Figure 6.13 it is clear that the measurement noise is quite large (with variances in the order of 10^{-4} rad^2/s^2). The measurement noise can be decreased using a higher order analog filter, in this application only a passive first order analog filter was used.

6.5.2 Integrated rate sensor outputs

The rate sensor data was then integrated to give angular displacements. The graph of angular displacements is shown in Figure 6.15 indicating maximum angle random walk in the order of 30 radians over a 7 hour period. The average drift was determined by calculating the drift over each 1 hour period

Table 6.4: Angle Random Walk and Rate Random Walk values for the rate sensors

Rate Sensor	**ARW** $\left(1 \times 10^{-4}\, rad/s/\sqrt{Hz}\right)$	**RRW** $\left(1 \times 10^{-5}\, rad/s^2/\sqrt{Hz}\right)$
Roll 1:	6.77	2
Roll 2:	6.69	2.3
Pitch 1:	6.38	1.8
Pitch 2:	7.46	1.2
Yaw 1:	6.26	0.95
Yaw 2:	7.09	1.5

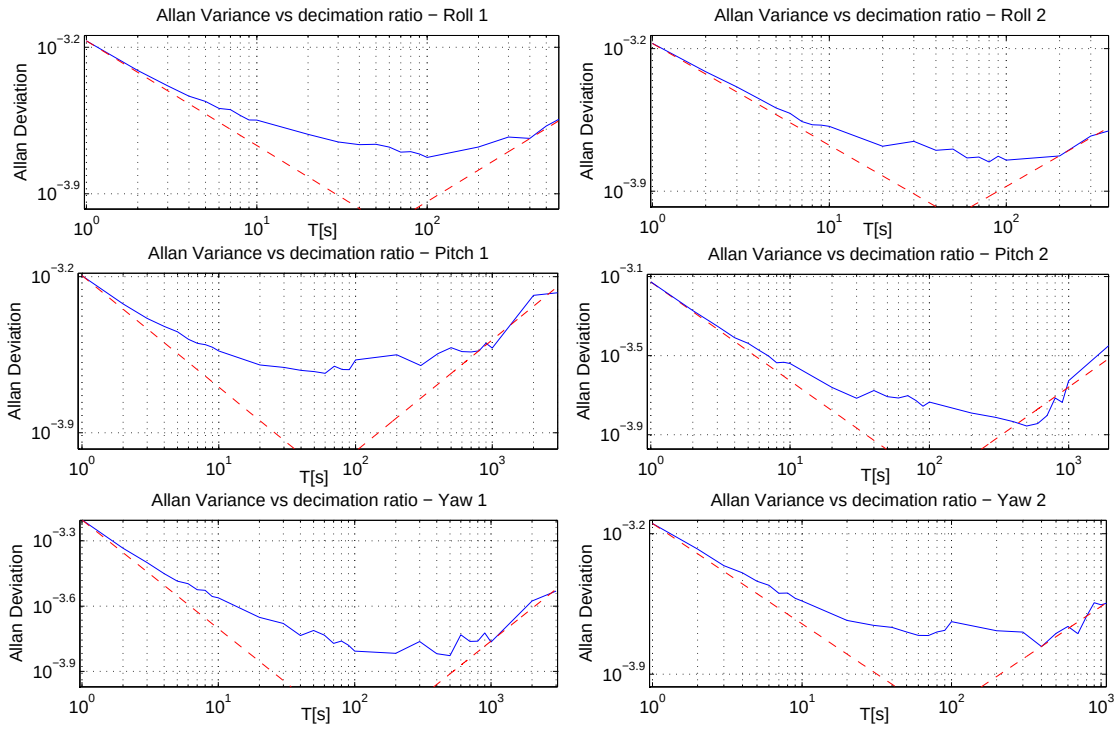

Figure 6.14: Allan Variance of the rate sensor outputs

for every sensor and taking the average over all these periods. The result was an average angular drift in the measured Euler angles of 203 degees per hour.

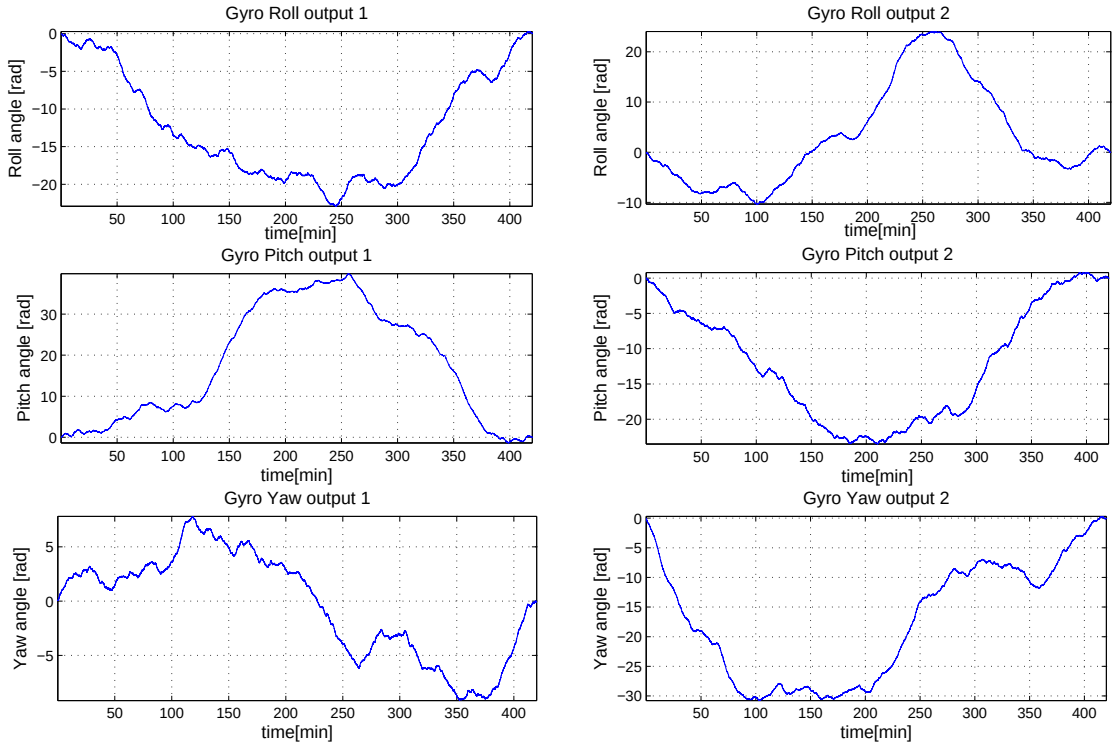

Figure 6.15: Integrated rate sensor outputs

6.5.3 Filtered rate sensor outputs

The rate sensor outputs are filtered to retain the only the rate random walk effect. The filter frequency is chosen from Figure 6.14, where the Allan deviation value is at its smallest. This means that all the measurement noise will be filtered out. The graph in Figure 6.14 reaches a minimum at an averaging time of 500 s, which means that a filter frequency of 0.02 Hz must be used. The filtered rate sensor output retaining only the rate random walk effect can be seen in Figure 6.16.

The rate random walk is due to temperature changes and other effects influencing the rate sensor output bias. From Figure 6.17 it can be seen that

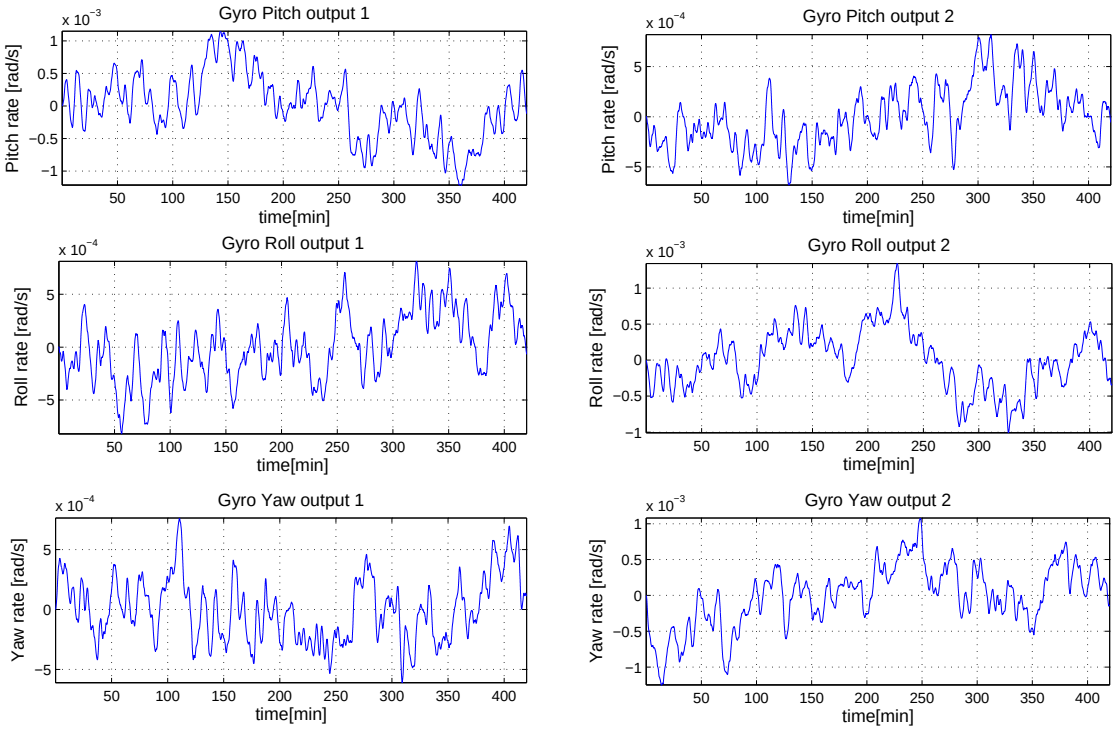

Figure 6.16: Filtered rate sensor outputs - at cut off frequency of 0.02 Hz

the temperature variations during these tests were minimal, which means that the rate random walk recorded was mostly due to the characteristics of the sensor. The changes in the bias of the output of the rate sensors due to temperature variation can be eliminated after calibration.

6.5.4 Rate sensor characterization

The rate sensor output can be modelled as the true angular rate added to measurement noise (white noise) and a random walk process (integrated white noise) as seen in equation (6.5.1). The measurement noise figure is expressed in the covariance matrix of the rate sensor outputs and the random walk process is described by the covariance matrix of the derivative of the filtered rate sensor outputs. To identify the noise characteristics of this sensor it is also required to be able to identify rate random walk and angle random walk values for each of the sensors as seen in Table 6.4.

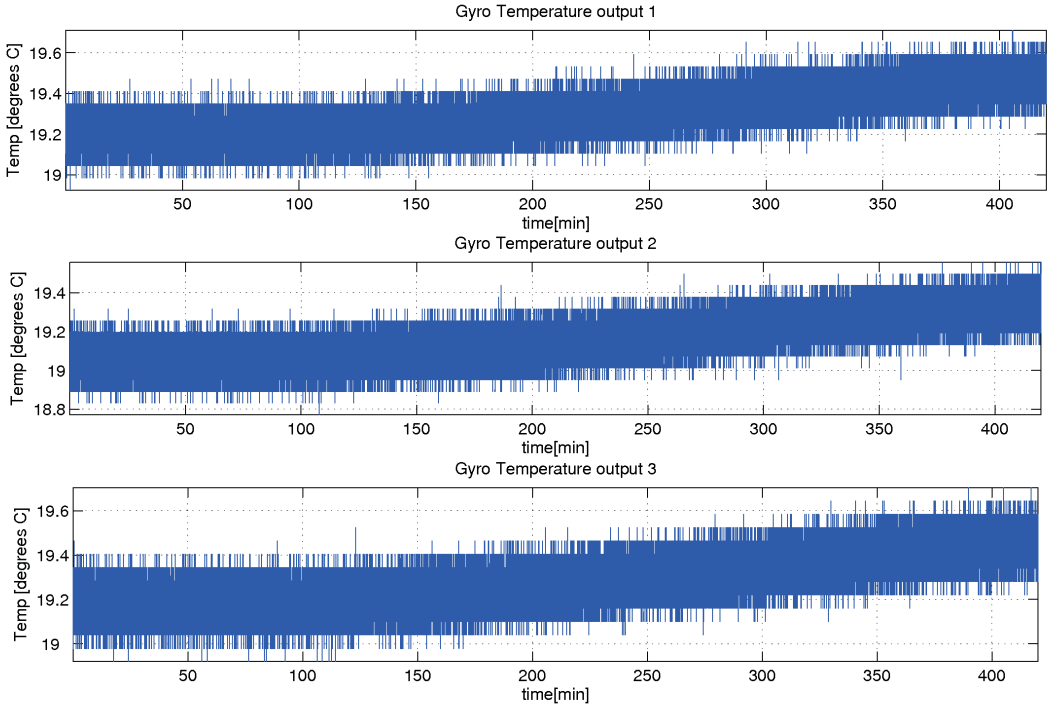

Figure 6.17: Temperature outputs of rate sensors

$$y = \omega + b + v \tag{6.5.1}$$

Where,

y = rate sensor output

$\dot{b}$ = w_b

b = rate sensor bias from random walk process

w_b = RRW component noise

$\mathbf{Q}$ = $Cov[w_b]$

= RRW covariance matrix

v = ARW component noise or measurement noise

$\mathbf{R}$ = $Cov[v]$

= ARW covariance matrix

ω = true angular rate

The covariance matrix of the rate sensor outputs is shown in equation (6.5.2) (with units of $1 \times 10^{-5}\,\mathrm{rad}^2/\mathrm{s}^2$).

$$\mathbf{R} = \begin{bmatrix} 0.4113 & -0.0038 & -0.0030 & 0.0043 & -0.0018 & 0.0018 \\ -0.0038 & 0.3997 & 0.0082 & -0.0017 & -0.0013 & 0.0061 \\ -0.0030 & 0.0082 & 0.3842 & -0.0074 & -0.0006 & -0.0018 \\ 0.0043 & -0.0017 & -0.0074 & 0.5286 & -0.0005 & 0.0049 \\ -0.0018 & -0.0013 & -0.0006 & -0.0005 & 0.3389 & 0.0005 \\ 0.0018 & 0.0061 & -0.0018 & 0.0049 & 0.0005 & 0.4662 \end{bmatrix} \tag{6.5.2}$$

The covariance matrix of the derivative taken of the filtered rate sensor outputs (with units of $1 \times 10^{-11}\,\mathrm{rad}^2/\mathrm{s}^4$) is shown in equation (6.5.3).

$$\mathbf{Q} = \begin{bmatrix} 0.3139 & -0.0323 & 0.0271 & -0.0075 & 0.0015 & 0.0017 \\ -0.0323 & 0.2821 & 0.0297 & 0.0086 & 0.0007 & 0.0260 \\ 0.0271 & 0.0297 & 0.4796 & -0.0137 & 0.0151 & 0.0064 \\ -0.0075 & 0.0086 & -0.0137 & 0.2687 & 0.0074 & -0.0041 \\ 0.0015 & 0.0007 & 0.0151 & 0.0074 & 0.2687 & 0.0154 \\ 0.0017 & 0.0260 & 0.0064 & -0.0041 & 0.0154 & 0.3288 \end{bmatrix} \tag{6.5.3}$$

6.5.5 Rate sensor measurements improvement method

The rate sensors were the only feedback used during the experimental setup (as seen in Figure 6.19) tests which were conducted. Due to the Euler angle drifts on these sensors a possibility of improving the measurements using multiple sensors per axis was explored. An article by Bayard [2], which implements a Kalman filter to combine the readings from each sensor, was studied. It proved that a theoretical improvement of the angular rate measurements was possible if the outputs of the sensors on each axis have a high negative correlation factor. This proved not to be the case in practice, for which reason this technique was not implemented.

6.6 Control system - air bearing experimental setup

In this section the control system which is implemented as a Simulink simulation (as seen in Figure 6.18), to control the attitude of the air bearing experimental setup, will be discussed in detail along with its performance. At first the air bearing experimental setup and the simulation will be explained and thereafter the communications interface between the simulation and the reaction wheel microcontroller. Then some results will be discussed, whereafter the external disturbances will be taken into consideration.

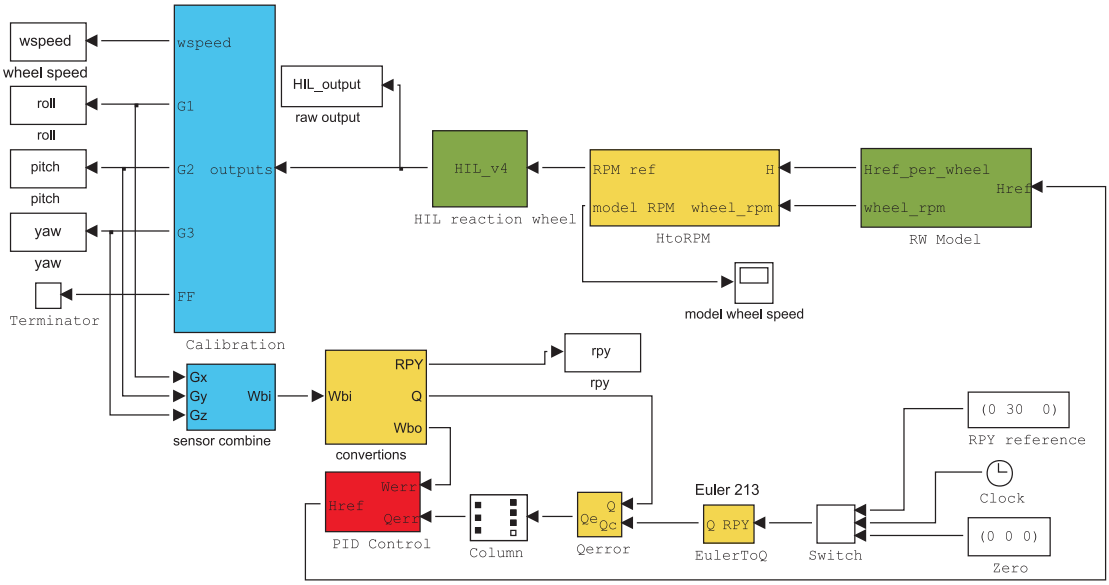

Figure 6.18: HIL simulation - air bearing experimental setup

6.6.1 Air bearing experimental setup overview

The experimental setup as seen in Figure 6.19 is used to prove that the reaction wheel system can be used, along with the rate sensors as feedback, to control the attitude of the setup with one free axis of rotation at a time. The experimental setup consists of 5 main parts. The level adjustable table is used to ensure that the setup is level. The air bearings are used to create near frictionless conditions for rotation in one axis. A metal bar placed on top of a glass disk (which floats on top of the air bearings) is used to represent the moment of inertia of the nanosatellite. The reaction wheel system is also placed

on top of the glass disk. To ensure that lateral disturbances do not push the setup off the air bearings, a cable which is hung from the ceiling, is attached to the reaction wheel system. The communications and power supply lines also run along this cable. The cable only suspends some of the weight of the reaction wheel system to ensure that minimum lateral movement and only rotation takes place.

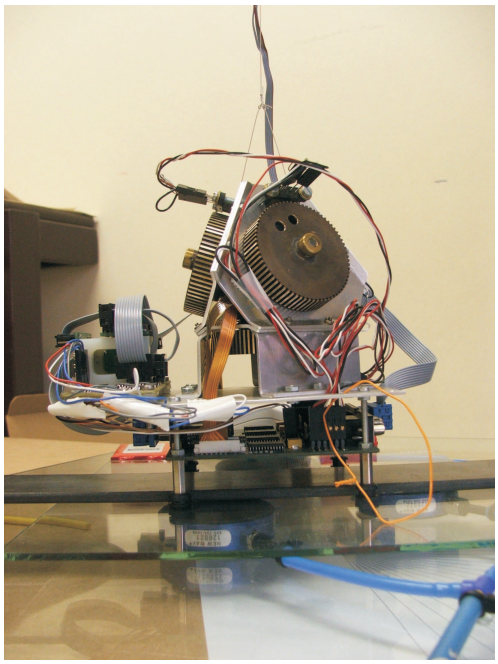

Figure 6.19: Experimental Setup

6.6.2 HIL simulation components

The hardware-in-the-loop simulation (as seen in Figure 6.18) can be divided into four main parts. The first part is the hardware-in-the-loop block. It implements the communication protocol which is used to communicate with the 8051 microcontroller. The input to this block is the reference reaction wheel speeds for each wheel and the output is the measured wheel speeds and the rate sensor and temperature outputs. The second block is the rate sensor calibration block. It implements the orthogonality, temperature and initial conditions calibration of the rate sensor outputs. The third block is the reaction wheel system block which is a model of the four reaction wheels.

This block is used to compare the measured wheel angular velocities to the predicted angular velocities in the reaction wheel model. The last of the four main parts of the simulation is the PD controller. This implements the controller which controls the attitude of the experimental setup in one axis at a time. It makes use of a quaternion error input and the angular velocities measured by the rate sensors. Its output is a reference angular momentum for each of the four reaction wheels.

6.6.3 Moment of inertia

The moment of inertia of the air bearing experimental setup was determined applying the law of conservation of momentum. The test was started while all the reaction wheels and the experimental setup were stationary. The reaction wheel in the vertical (pitch) axis is spun up to a fixed wheel speed. Accoring to the law of conservation of momentum (equation (6.6.1)) the experimental setup will now have an equal opposite momentum. The rotational speed of the setup is measured and used to calculate its moment of inertia.

$$I_{rotor} \times \omega_{rotor} = I_{setup} \times \omega_{setup} \tag{6.6.1}$$

The moment of inertia of the reaction wheel rotors therefore needed to be determined accurately. This was done using a computer-aided design (CAD) program and the string suspension method (as discussed in Appendix D) to verify the accuracy of the result. The CAD analysis revealed a result of 36.8 $\times 10^{-6}$ kgm^2 for the moment of inertia of the reaction wheel rotor. It was found that there was a significant difference between the result using the CAD program and the string method. It was decided that the CAD result was more accurate (and reliable) and it was therefore used for further calculations.

A wheel speed of 3000 rpm (or 314.16 rad/s) was commanded for the reaction wheel in the vertical (pitch) axis. This results in a wheel angular momentum of 11.56 mNms. The experimental setup will therefore have an equal opposite momentum, as discussed above. The angular velocity of the setup was measured for 10 different tests and an average angular velocity of 2.459 rpm (or 0.258 rad/s) was found. The moment of inertia of the air bearing experimental setup was therefore determined as 44.9 $\times 10^{-3}$ kgm^2.

The moment of inertia used in the PD controller of the air bearing experimental setup control system was therefore adjusted to the calculated value for the setup.

6.6.4 Communications interface

Similar to the hardware-in-the-loop simulation a UART interface is used to communicate with the 8051 microcontroller. A baud rate of 19200 bps is used for this communication interface. The protocol is designed so that a speed command can be sent every 100 ms to the 8051 microcontroller, while a measured wheel speed for each wheel along with the six rate sensor outputs and the three temperature outputs is received from the 8051 microcontroller each 100 ms. The time of communication is however determined by the microcontroller so that the 100 ms interval between each data packet is accurate.

6.6.5 HIL control system results

Due to the HIL air bearing experimental setup the control system could only be tested with one free axis of rotation. Some results will be given to prove that the control system performed as expected in the particular axis of rotation. Firstly the measured pitch Euler angle obtained by integrating the rate sensor data can be seen in Figure 6.20(a). These measurements were taken after giving a reference step pitch angle of 30 degrees at 25 s. The reference angle step of 30 degrees is followed with a five percent settling time of 17 seconds. When compared to the specification of 30 degrees reference angle step in less than 60 seconds it proves that the system satisfies its requirements with quite a large margin.

When looking at the angular velocities of each of the four reaction wheels (as seen in Figure 6.20(b)) it is clear that the maximum wheel speed of 5000 rpm is not exceeded. The build up (or loss) of angular momentum on each of the wheels during standstill (between seconds 50 and 100) is due to external disturbances mostly caused by the cable connected to the ceiling. This cable ensures that the setup does not slide off the three air bearings.

The rate sensor angular and rate variations are now compared to the con-

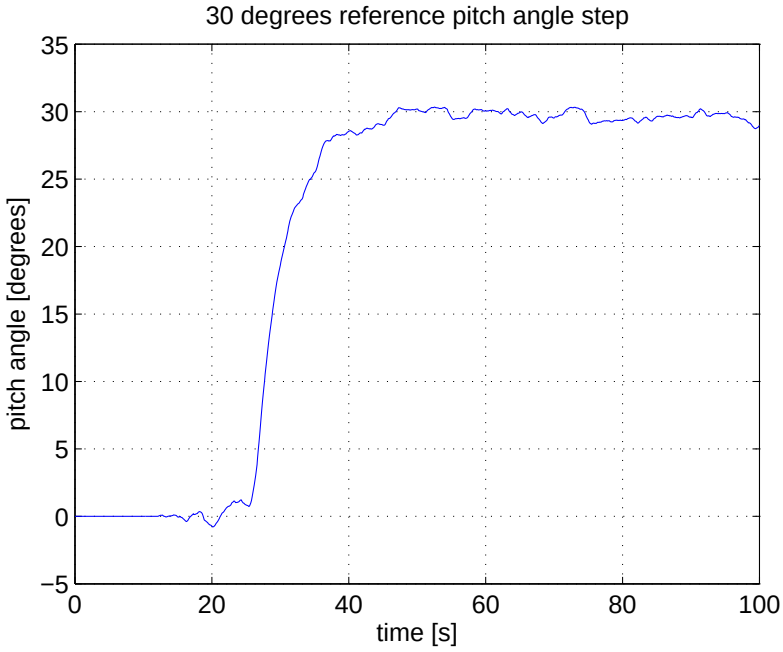

(a)

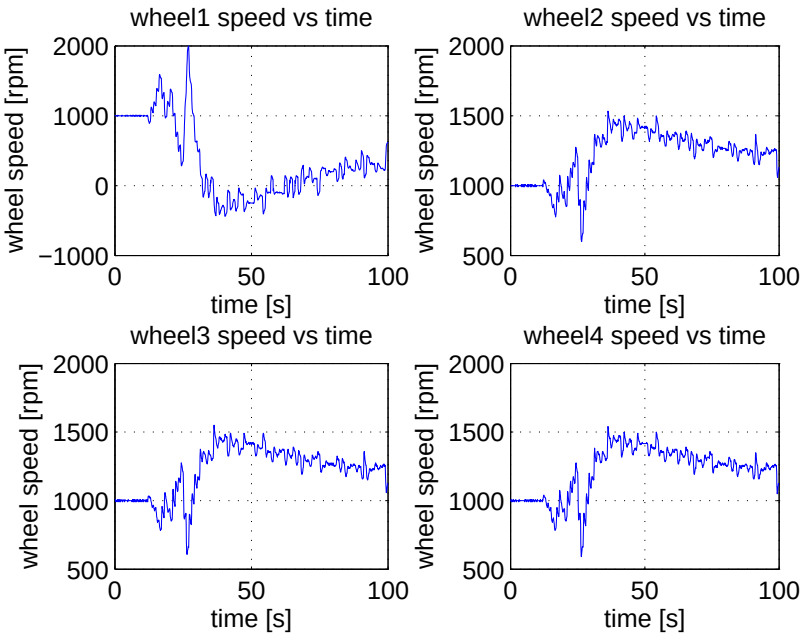

(b)

Figure 6.20: (a) 30 degree reference pitch angle step, (b) Reaction wheel angular velocities during this maneuver

trolled angular and rate variations (RMS), respectively, at a constant reference angle. This is done to determine the variation which is added by the controller. This analysis gives another perspective on the efficiency of the controller which is implemented.

Firstly the angular RMS values from the integrated rate sensor signal and the controlled angle is measured. From Figure 6.20(a) a RMS angular variation, between seconds 50 and 100, of 0.352 degrees can be measured. The measured RMS variation of the integrated rate sensor signal is 0.297 degrees. From these values it can be seen that the controller adds a small amount of RMS variation to the measured signal. The initial drift which can be seen in Figure 6.21 is during the calibration time (during first 10 seconds). The offset which is still emminent at 10 seconds in the simulation is therefore eliminated after calibration and will not have an effect on the simulation.

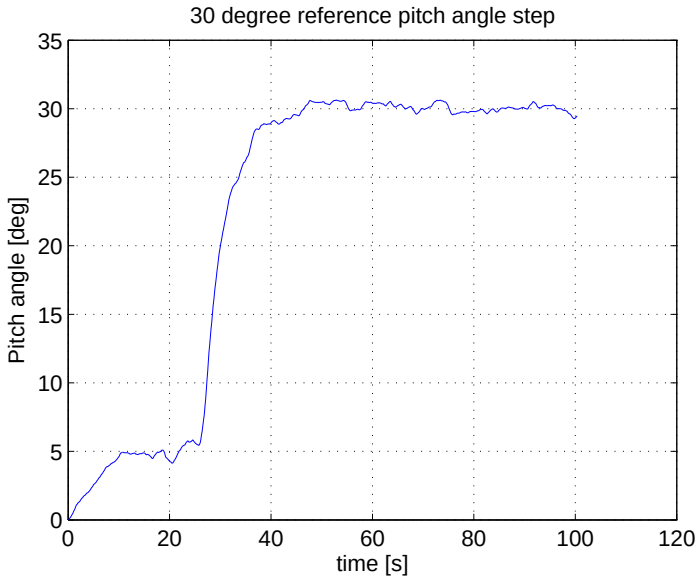

Figure 6.21: Integrated rate sensor measurement of the 30 degree pitch maneuver

The rate variations are now calculated using the rate sensor signal and the controlled rate. The satellite orbit referenced body angular rate is used to find the controlled RMS rate variation. The controlled RMS rate variation was calculated as 0.38 $^{\circ}$/s. The RMS variation of the rate sensor signal is

measured as 0.47 °/s. The reason why the RMS rate variation of the controlled rate is smaller than that of the rate sensor signal is the fact that the satellite attitude control loop is closed at 1 Hz and the rate sensor signal has a frequency of 10 Hz. This means that the controller uses the average of 10 rate sensor measurements to control the attitude of the satellite. This brings about the difference in rate RMS variation.

The last analysis looks at the RMS variation of the high pass filtered measured wheel speed signal. The highpass filtered wheel speed signals are shown in Figure 6.22. The average RMS variation of the filtered wheel speed signals is calculated as 62.99 rpm. This RMS variation shows that a large amount of control input is used to keep the satellite stationary. A lower RMS value would be preferable due to the smaller power consumption (at a constant reference angle) it would have as a result. The variation in the wheel speed can be decreased using either of the following two methods: The first would be to use a rate sensor with less measurement noise and the other method would be to design a controller with a lower bandwidth to be used when no maneuvers are executed.

6.6.6 External disturbances

The external disturbances have unwanted effects on the experimental setup. These disturbances are due to the cable suspended from the ceiling which counters any lateral disturbances. The communication and power wires which run along this cable also create disturbance torques. These disturbance torques create a momentum buildup on the reaction wheels, which could cause the momentum on the reaction wheels to saturate. The disturbances are however small enough to be compensated for during a 100 second test period. It was not possible to measure the magnitude of the disturbance torques due to the fact that they vary depending on the angular position of the setup and the position of the wires running along the cable. Air movement around the experimental setup could also cause disturbance torques, but they will be much smaller than that of the disturbances caused by the cable and wires.

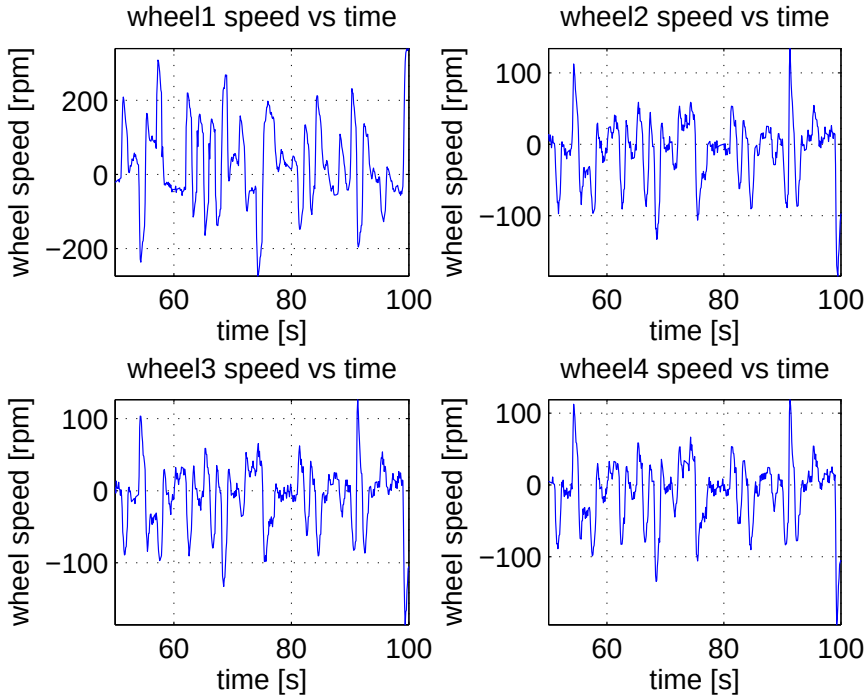

Figure 6.22: High pass filtered wheel speed measurements of the 30 degree pitch maneuver

Chapter 7

Conclusions and Recommendations

This chapter will present some of the conclusions made after completing this project. The conclusions will be divided into three sections. The first will discuss the effectiveness of the reaction wheel system to be used as actuator on a nanosatellite. The second will entail the viability of the rate sensor for space applications. The experimental setup will be evaluated critically discussing the results obtained and how they can be improved. Lastly the outcomes will be discussed in the light of the specifications given for each system evaluating their fulfillment of the goals set.

The recommendations part of this chapter will look at possible improvements on each of the systems and subsystems designed. Recommendations will be made for future work and classified in the order of importance.

7.1 Conclusions

7.1.1 Satellite simulation evaluation

The satellite model used in the simulation provides a platform on which the reaction wheels could be tested as attitude actuators. Due to the fact that all of the subsystems of the satellite are currently in the design phase, the actual characteristics of the satellite, such as its size, weight and moment of inertia, can only be estimated. The simulation can thus only be used to verify, using the model of the reaction wheel and the estimated model of the satellite, that

the reaction wheel is an adequate actuator for the final satellite. The moment of inertia values chosen for the nanosatellite model were estimated using a flat cylindrical shape for the satellite, because it requires a small drag coefficient. This is why the moment of inertia in the vertical axis (z-axis) is larger that in the lateral axes (x- and y-axis) as seen in equations (7.1.1), (7.1.2) and (7.1.3). The estimated satellite dimensions are as follows: It has a height of 0.22 m and a diameter of 0.4 m, giving it a volume of 0.0276 m^3.

$$I_x = 0.14 \quad kgm^2 \tag{7.1.1}$$

$$I_y = 0.14 \quad kgm^2 \tag{7.1.2}$$

$$I_z = 0.2 \quad kgm^2 \tag{7.1.3}$$

It was therefore decided to use the real reaction wheel in the simulation by conducting certain hardware-in-the-loop tests. These HIL simulations would serve a double purpose, firstly it would eliminate the errors made by using the model of the reaction wheel and secondly it could verify the reaction wheel model.

Hardware-in-the-loop evaluation

During these simulations, as explained previously, the reaction wheel model was replaced with the actual reaction wheel system. This served the purpose of being able to design a controller to control the satellite attitude by using the physical reaction wheel system. This simulation proved that the reaction wheel performed as expected and the results showed that the torque and momentum storage capability specifications were met. The closed loop specifications for the satellite attitude controller were also met using the actual reaction wheel system as actuator.

7.1.2 Reaction wheel system evaluation

Torque and momentum storage capability

The specifications for each reaction wheel, of 5 mNm maximum torque and 20 mNms momentum storage capability, were met as stated above. This was done using one of the smallest and most power efficient BLDC motors currently available on the market. Until more efficient products are available the chosen motor suits this application best. These, above stated, specifica-

tions allow for a rotational maneuver of 30 degrees to be completed with a five percent settling time of less than 20 seconds as shown in the HIL simulation. The specification was therefore met, requiring a 30 degree maneuver to be completed in at least 60 seconds. This is more than adequate for the application as described in the mission objectives.

Size, mass and power usage

Seeing that the reaction wheel system was designed to be used on a nanosatellite, some of the most important design specifications were its size, weight and power usage. These specifications were however not fixed values, due to the fact that the current technology available needed to be explored and the smallest, lightest, most power efficient design was required. The results of the system regarding these specifications were found to be quite viable for its space application.

The total mass of 751 g is 7.5 percent of the maximum total satellite weight of 10kg. This ratio is quite acceptable taking into account that the reaction wheels contribute most of the weight of the ADCS and the proportional weight of the ADCS of an average satellite is normally a tenth of the total satellite mass. There is however still a margin for improvement in the weight of the tetrahedral structure, due to the thickness of the aluminium used currently.

The size of 110 mm by 110 mm by 130 mm occupies about 6 percent of the estimated total satellite volume of 0.027 m^3. This ratio is adequate, especially when taking into account that the on board electronics (such as the on board computer) are becoming smaller with improved technology and will require a smaller internal volume of the satellite.

A power analysis was done for the average consumption per orbit. It was assumed that no maneuvers would be done in eclipse and two maneuvers would be completed in the sunlit part of the orbit. These maneuvers would entail a positive 30 degree off-nadir reference pitch angle step and a reference angle to return to the nadir position and another equivalent maneuver in the negative 30 degree direction. Measurements were taken to determine the average power consumption for a single 98.2 minute orbit expecting the

maneuvers, as explained above, to be executed. The estimated eclipse time for the nanosatellite is 35 minutes and the period in the sunlit part of the orbit 63 minutes. The maneuvers are expected to last 17 seconds (see Figure 6.20(a) each. This means that for the rest of the orbit (97.1 minutes) the rotors will be spinning at a constant speed of 1000 rpm. The power consumption for the wheels to run at the nominal offset speed of 1000 rpm is 2.7 W (as seen in Table 6.2). The average power consumption, over the 17 seconds it takes to complete a 30 degree maneuver (in one direction), was measured as 6.36 W. This means that the average power consumption per orbit was estimated to be 2.74 W.

A Lithium-Ion battery has a specific energy density of 70 - 110 Wh/kg, which means that the storage capacity to support the nominal offset wheel speed of 1000 rpm should not be a problem (when a total battery mass of about 0.5 kg is allowed).

The output power intensity of Silicon solar cells, at the beginning of their lifetime, with the sun normal to the surface of the cells is 202 W/m^2. The cylindrical surface of the satellite (as discussed in section 7.1.1) facing the sun will be 0.088 m^2. Therefore the power generated by the solar cells (in the sunlit part of the orbit) according to equation (7.1.4) is 17.8 W.

$$P_O = P_{intensity} \times A_{solar\ panel} \tag{7.1.4}$$

The required power to be supplied by the solar cells, in the sunlit part of the orbit, is determined using equation (7.1.5). The efficiencies of the voltage supply paths from the solar cells (X_d) and the batteries (X_e) are estimated as 90% and 80% respectively. The time during eclipse (T_e) and during the sunlit part of the orbit (T_d) are as discussed above. The power consumption during daylight is estimated as 14 W and the consumption during eclipse, 10 W. This estimation was done by assuming that the reaction wheel system power consumption will be a fifth of the total power consumption during daylight and that most of the other susbsystem will be switched to a lower power mode during eclipse. According to equation (7.1.5) a solar array capable of

generating 22.5 W during the sunlit part of the orbit will be necessary.

$$P_{sa} = \frac{\frac{P_e T_e}{X_e} + \frac{P_d T_d}{X_d}}{T_d} \tag{7.1.5}$$

From the calculations, (7.1.4) and (7.1.5), it can be seen that the power required from the solar panels are higher than the power which can be generated by the Silicon solar cells. Solar cells with a higher efficiency (for example Gallium Arsenide cells) will therefore be required for this nanosatellite. Improvement on the power consumption of the reaction wheel system might also be necessary, which will decrease the average power usage per orbit.

Reaction wheel electronics

The BLDC controller (which has internal power MOSFET transistors) chosen for this application was the most compact and power efficient controller which could be found on the market. The maximum quiescent supply current of 10 mA however makes a large contribution to the total power usage (as seen in Table 6.1). It would be advisable to use a more power efficient product when it becomes available.

The 8051 microcontroller on which the speed controller is implemented, proved to have sufficient processing power for the tasks it is required to perform. Its measured power usage of 90 mW is also a very small part of the total power usage of the reaction wheel electronics (as seen in Table 6.1).

The voltage regulator used to convert the 12 V bus voltage to 5 V has a maximum efficiency of 95 percent at a load of 0.2 A. As shown by Table 6.1 the regulator will however be used at a nominal load of 0.1 A, where the efficiency will be 92 percent. The regulator used to convert from 5 V to 3 V was however chosen to be a linear regulator (due to the fact that the output and input voltage difference is small) and its efficiency will be lower.

7.1.3 Rate sensor system evaluation

The aim of testing the rate sensors was to determine whether they can be used on a nanosatellite. It was found that the sensors have a bias stability of 203 degrees per hour or 3.4 degrees per minute. The sensors have an angular

random walk in the order of 7 $\times 10^{-4}$ rad/s/$\sqrt{Hz}$. Comparing this to newer rate sensors available on the market (for example the ADIS16250), the rate sensors used in this project perform poorly. The ADIS16250, manufactured by Analog Devices, has a bias stability of 57.6 degrees per hour or 0.96 degrees per minute. Its range of $\pm 320\,^{\circ}$/s is four times larger than that of the rate sensor used in this project. This means that the angular random walk value as specified in the ADIS16250 datasheet, for the equivalent range of the rate sensor used in this project, will be four times smaller. Its angular random walk without digital filtering is therefore 2.5 $\times 10^{-4}$ rad/s/$\sqrt{Hz}$ for a $\pm 80\,^{\circ}$/s range. This means that after implementing the 10 Hz digital filter as in the case of this project the ADIS16250 will perform much better than the rate sensors used for this project.

When looking at the specification set for other space applications it is clear that an angular random walk in the order of 5 $\times 10^{-5}$ rad/s/$\sqrt{Hz}$ and a bias stability in the order of 100 degrees per hour is acceptable. In the 3-Axis micro gyroscope feasibility study done by Prezzavento [12] different rate sensor application classes were compared, ranging from orbit control to failure detection. The article determines the average required angular random walk and bias stability for each of these classes. These specifications were used to evaluate the characteristics of the rate sensors used in this project. These values were also compared to the results from an article by Dussy [7].

It can therefore be concluded that the rate sensors used in this project are not the best sensors currently available on the market and their performance leaves a large margin for improvement. This sensor would not be adequate for space applications and further research on other sensors, such as the ADIS16250 would be necessary. The ADIS16250 was not available at the time during the project when the rate sensors for this project was chosen.

7.1.4 Air bearing experimental setup evaluation

To evaluate the experimental setup it would be required to compare it to the situation it simulates, when the satellite is in space. The fact that the experimental setup only has one free axis of rotation limits the testing possibilities. The setup can however be tested in three orthogonal axes (during three different tests by, changing the setup orientation) to prove that it would

perform as expected in a full three axis of rotation environment. The other main drawback of the experimental setup is the disturbance torques exerted by the stabilizing cable, communication and power wires connected to the setup. The disturbances are different with each test, making it difficult to analyse the true performance.

The experimental setup can thus be seen as a simulation of a satellite in space with: One free axis of rotation at a time and large disturbance torques. If it can be proven that the reaction wheel can be used successfully as actuator for the experimental setup it will also perform well in space. The only difference is that the maximum angular momentum will not be reached in such a short time, due to smaller disturbance torques in space.

It was shown during the tests using the experimental setup that the reaction wheel performed well, as the only actuator, over short periods of time. The tests thus prove that the reaction wheel system will be adequate for space applications on nanosatellites.

7.2 Recommendations

Regarding the reaction wheel system further improvements can be done in the following areas:

- The size and weight of the structure can be improved
- The optical reflective sensors can be replaced with a more power efficient sensor
- The number of slits on each rotor can be increased with a better machining process, to improve the speed measurement resolution
- The better machining process can be used for the manufacturing of the rotors to eliminate unbalances or the wheels can be properly balanced (static and dynamic)

Considering the rate sensor system the following improvements are recommended:

- A more power efficient rate sensor with better bias stability and smaller angle random walk characteristics must be found

- The analog filtering process must be done using an active filter, e.g., a second order Butterworth filter
- A 16-bit in stead of a 12-bit analog to digital converter can be used

The improvements which can be made to the experimental setup to minimize the external disturbances are as follows:

- The stabilizing cable can be replaced with a needle point rotational setup
- The communication wires can be replaced with a wireless RS232 connection
- Instead of the power cable Lithium Polymer (LiPo) battery cells can be used as power source

Appendices

Appendix A

Hardware

A.1 Reaction wheel mounting structure assembly

The structure as shown in Figure 4.2 is assembled from six different parts. Three baseplates as seen in Figure A.1(a) and three standoffs as seen in Figure A.1(b). The different parts are connected to each other using 2.5 mm screws and bolts. It was necessary to design the structure so that the BLDC motors could be fixed to the baseplates before the structure is assembled, due to the limited space inside the structure.

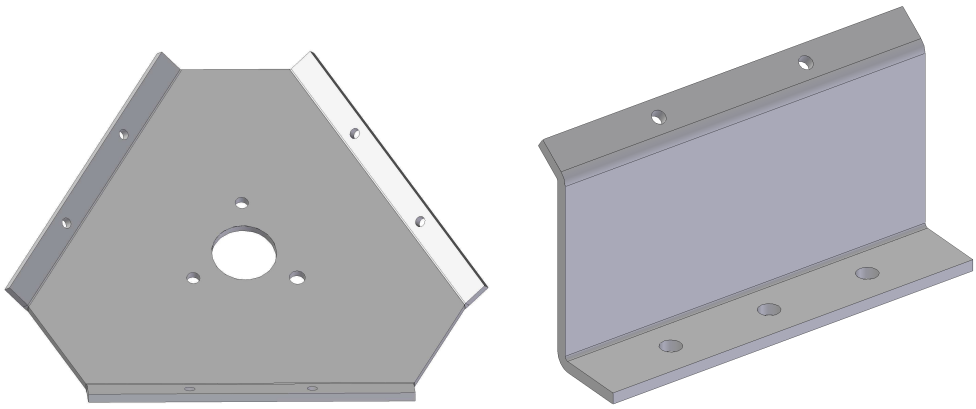

(a) (b)

Figure A.1: The reaction wheel structure (a) baseplate and (b) standoff

A.2 Reaction wheel PCB schematics

In this section the PCB schematics will be given for the reaction wheel PCB. The schematic for the BLDC drivers and peripherals includes the following components:

- BLDC controllers and their peripheral components
- Connector for the optical encoders
- Connector for each BLDC motor
- Bypass capacitors for each voltage level

The schematic for the power distribution and communication includes the following components:

- 5 V switching regulator
- 3 V linear regulator
- Power connector
- JTAG connector
- Current sense components for the 5 V power supply
- CAN controller with RS485 tranceiver
- RS232 tranceiver

The microcontroller schematic includes the following components:

- 8051 microcontroller
- Digital to analog converter and its reference voltage supply component
- Bypass capacitors for each of the voltage supplies
- LEDs to indicate that the voltage supplies are active
- 16 MHz crystal as external clock source for the 8051 microcontroller
- Reset circuitry

A.2.1 BLDC drivers

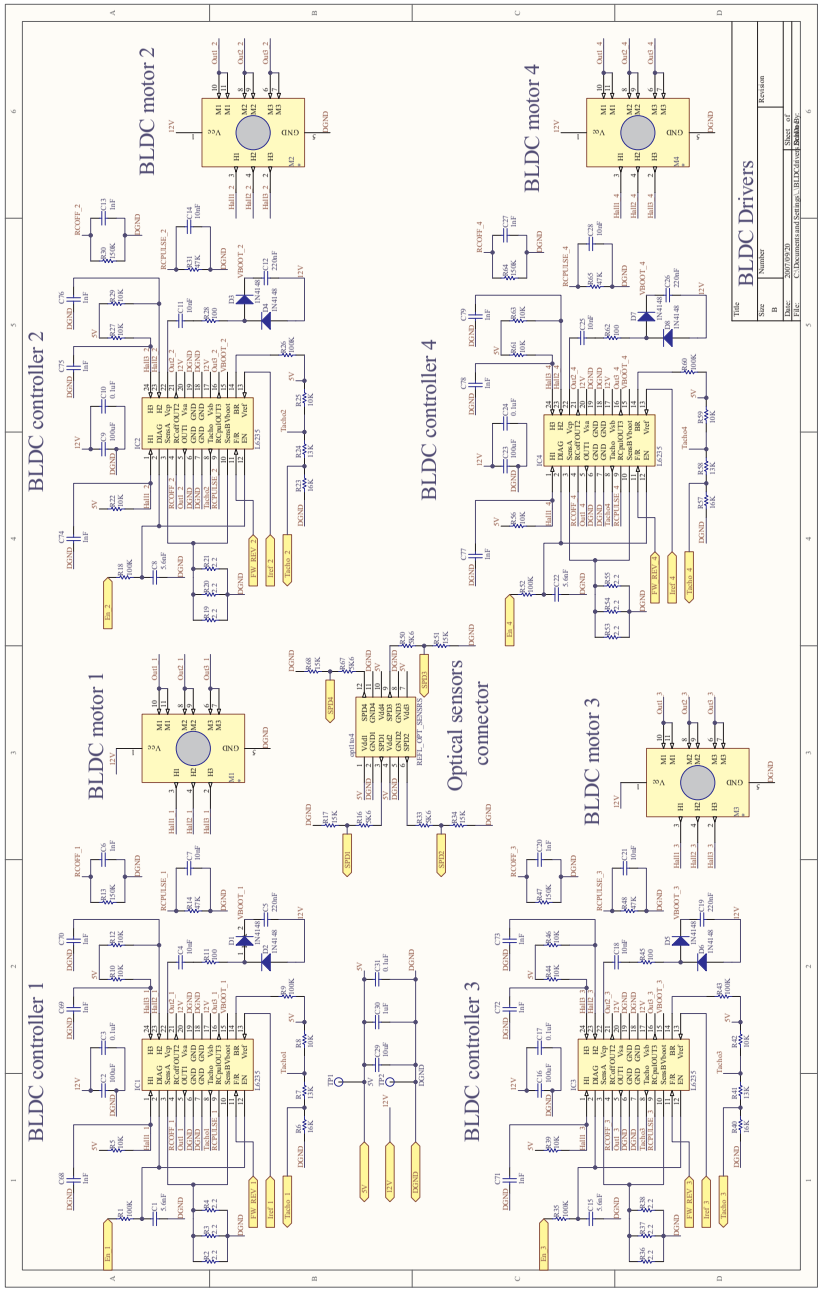

Figure A.2: BLDC drivers schematics

A.2.2 Power distribution and communication

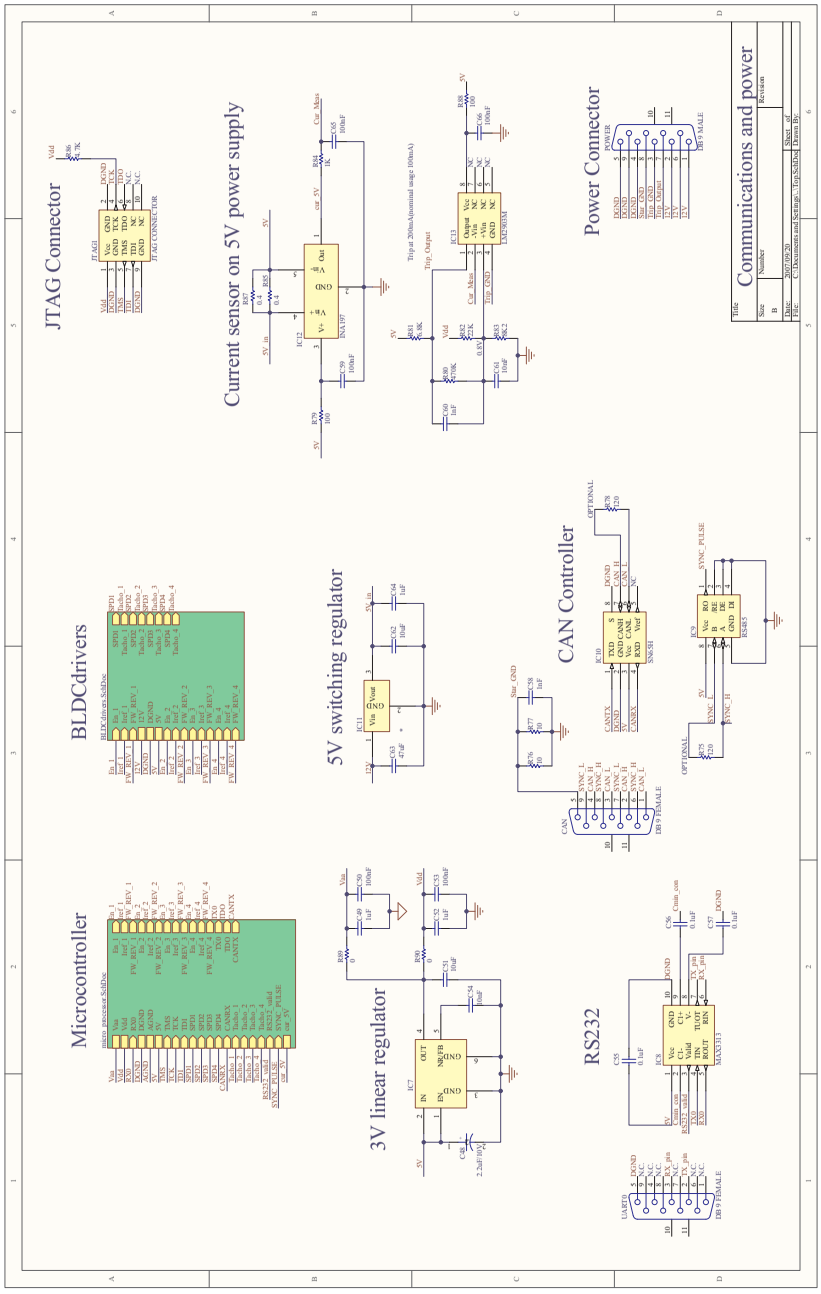

Figure A.3: Power distribution and communications schematics

A.2.3 Microcontroller and peripherals

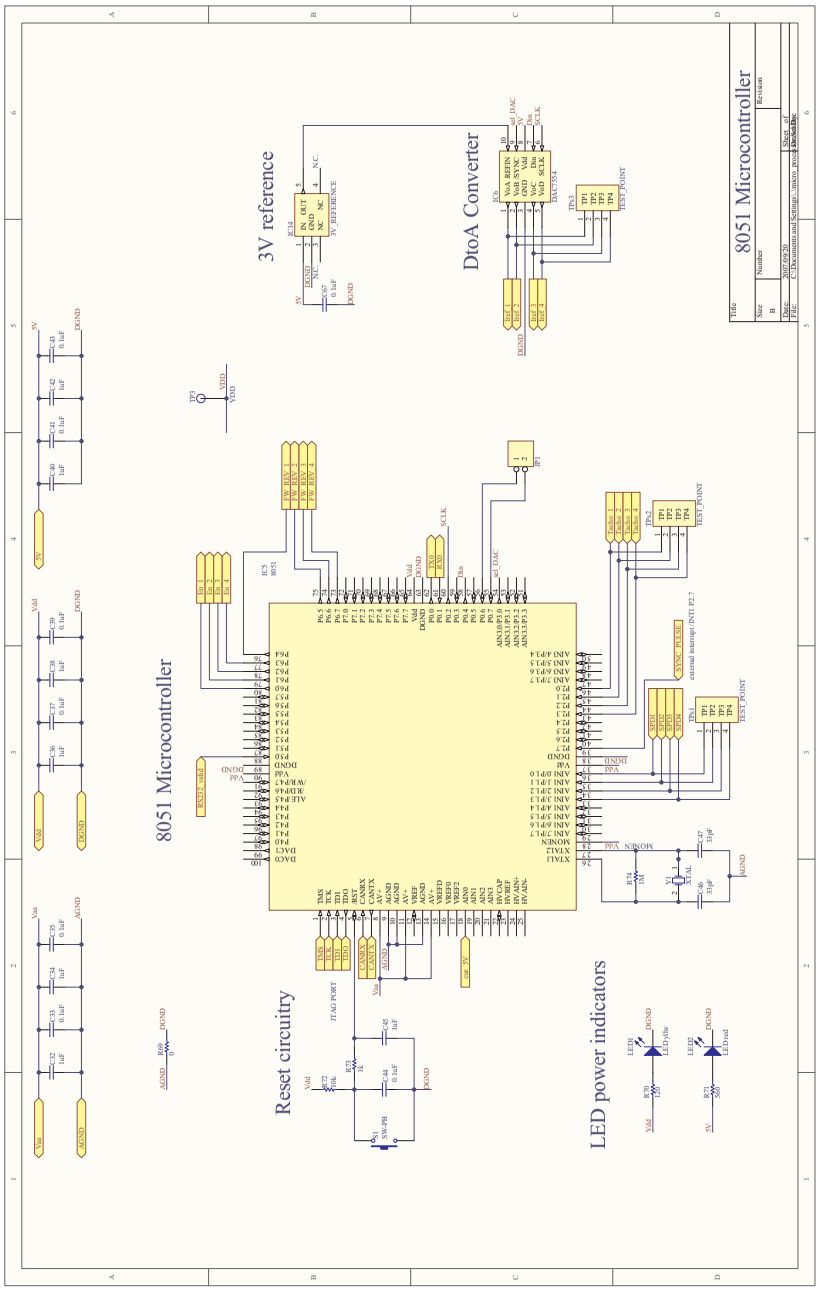

Figure A.4: 8051 microcontroller and peripherals

A.3 Rate sensor PCB schematics

In this section the PCB schematics for the rate sensor system will be given. The system is divided over four PCBs: The main rate sensor PCB and three equivalent othogonally mounted rate sensor PCBs. The main PCB includes the following components:

- Digital to analog converter
- 2 V reference supply component
- Power and I^2C connectors
- Connectors for each of the three mounted PCBs
- Operational amplifiers to change the rate sensor output voltage levels

The rate sensors themselves are soldered onto the three equivalent orthogonally mounted rate sensor PCBs. Each PCB has space for three rate sensors. The other components on this PCB are the rate sensor peripheral components including the passive analog first order filter.

A.3.1 Rate sensor Main PCB

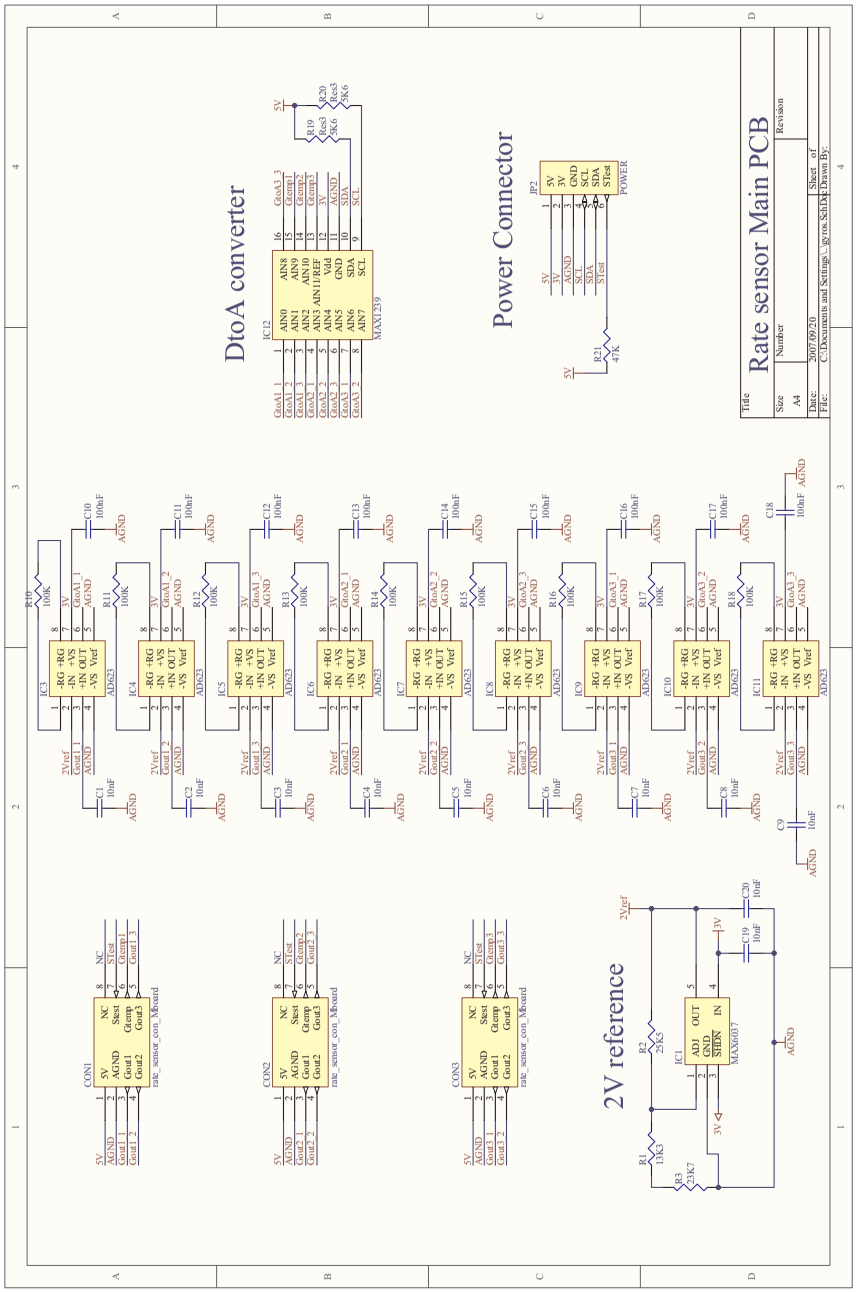

Figure A.5: Main Rate sensor PCB

A.3.2 Rate sensor Mounting PCB

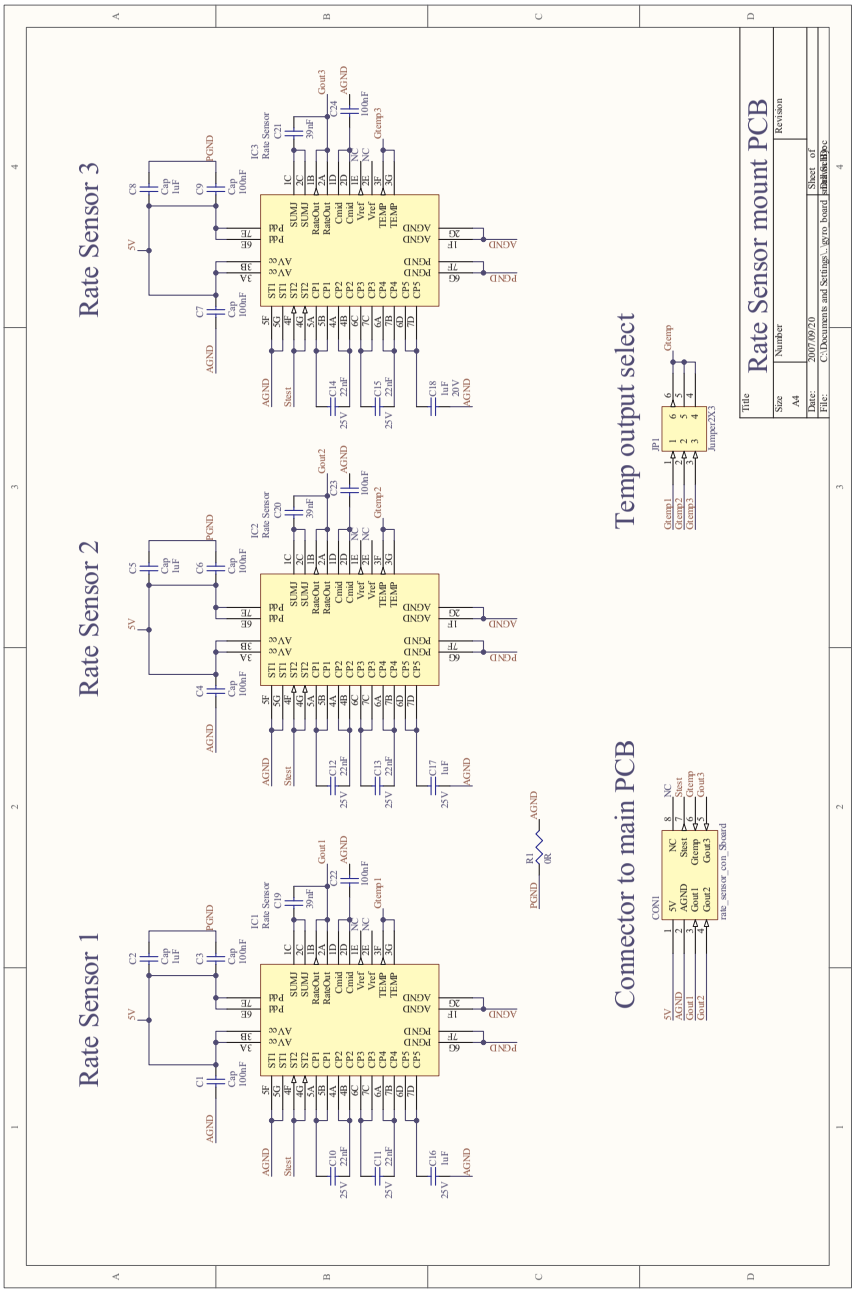

Figure A.6: Rate sensor PCB - mounted to the structure

A.4 Rate sensor filter design

Equation (A.4.1) was used to calculate the resistor and capacitor values for the passive first order low pass filter. Seeing that a 180 KΩ resistor is integrated into the rate sensor package, only the value of the capacitor needed to be determined. The required filter 3 dB cut off frequency is 20 Hz, as discussed in section 4.3.1. According to equation (A.4.1) a 44 nF capacitor is required for the specified cut off frequency. A 39 nF capacitor was therefore used, which results in a cut off frequency of 22.7 Hz. Figure A.7 shows the 3 dB cut off frequency of 22.7 Hz (or 142.6 rad/s) on a bode plot of the passive first order low pass filter.

$$f_{3dB} = \frac{1}{2\pi RC} \tag{A.4.1}$$

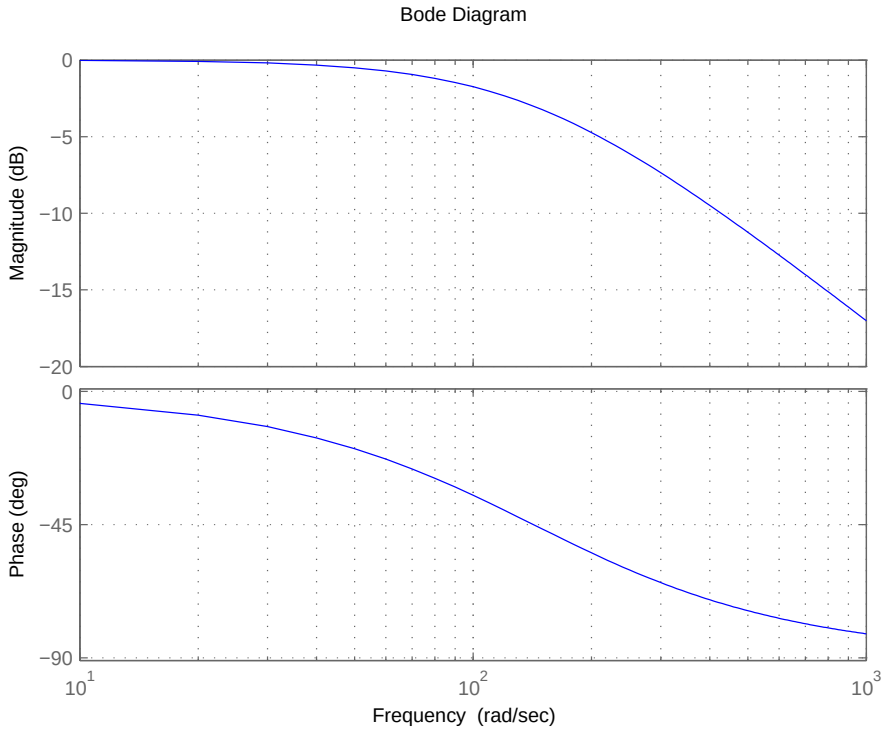

Figure A.7: Rate sensor Filter - Bode Plot

Appendix B

BLDC motors datasheets

The three BLDC motors as shown in Figure B.2, B.3 and B.4 were compared to determine which would fit the application best. Equation (B.0.1) was used to calculate the power usage of each of the three BLDC motors at the specified maximum output torque of 5 mNm and the specified maximum angular velocity of 5000 rpm. The equation for a DC motor was used for this calculation, but the power consumption of a BLDC motor can be calculated using the same equation. The results of the power calculations are shown in Table B.1. The meaning of the variables in equation (B.0.1) is depicted by the schematic in Figure B.1.

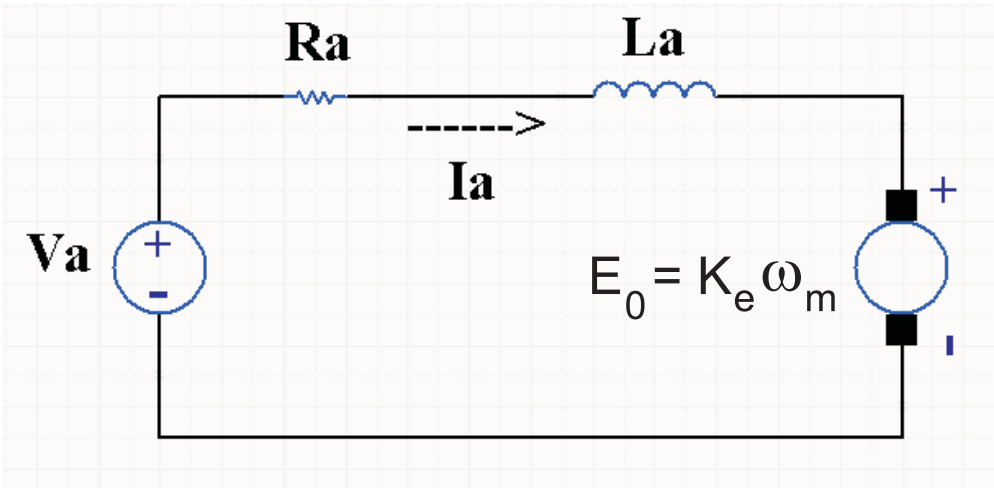

Figure B.1: Schematic to describe a DC motor

$$
\begin{aligned}
P_{max} &= V_{a\,max} I_{a\,max} \\
&= (V_{Ra\,max} + E_{0\,max})\, I_{a\,max} \qquad \text{(B.0.1)}
\end{aligned}
$$

Where,

$V_{a\,max}$ = Maximum voltage over armature

$I_{a\,max} = N_{max}/N_{const} + I_{NL}$

= Maximum armature current

I_{NL} = No load current

N_{const} = Torque constant

N_{max} = 5 mNm

= Maximum torque specification

$V_{Ra\,max} = I_{a\,max}\, \Omega_{terminal}$

= Maximum voltage over armature resistance

$\Omega_{terminal}$ = Terminal resistance

$E_{0\,max} = \omega_{max}/\omega_{const}$

= Maximum back EMF

ω_{const} = Speed constant

ω_{max} = 5000 rpm

= Maximum rotational speed specification

Table B.1: Power consumption of the BLDC motors compared

Motor Data	**Maxon 6 W**	**Faulhaber**	**Maxon 15 W**
N_{const}: Torque Constant [mNm/A]	9.5	6.34	49
I_{NL}: No load current [mA]	110	102	73
I_a: Armature current [mA]	636	891	175
ω_{const}: Speed Constant [rpm/V]	1007	1506	195
$\Omega_{terminal}$: Terminal resistance [Ohm]	4.5	3.4	13.7
V_{Ra}: Armature voltage [V]	2.86	3.03	2.4
E_0 [V]:	4.97	3.32	25.64
Power Consumption [W]:	**4.98**	**5.65**	**4.92**

maxon flat motor

EC 32 Flat motor ∅32 mm, brushless, 6 Watt

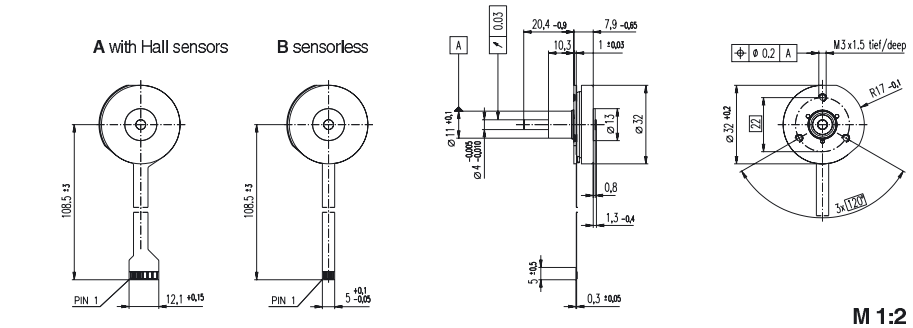

M 1:2

Stock program
Standard program
Special program (on request!)

			Order Number	
		with Hall sensors	200187	
		sensorless		200138
Motor Data				
1	Assigned power rating	W	6	6
2	Nominal voltage	Volt	9.0	9.0
3	No load speed	rpm	8600	8600
4	Stall torque	mNm	20	20
5	Speed / torque gradient	rpm / mNm	479.0	479.0
6	No load current	mA	110	110
7	Terminal resistance phase to phase	Ohm	4.50	4.50
8	Max. permissible speed	rpm	12000	12000
9	Max. continuous current at 5000 rpm	A	1.03	1.03
10	Max. continuous torque at 5000 rpm	mNm	8.70	8.70
11	Max. efficiency	%	60.0	60.0
12	Torque constant	mNm / A	9.5	9.5
13	Speed constant	rpm / V	1007	1007
14	Mechanical time constant	ms	70.0	70.0
15	Rotor inertia	gcm²	13.9	13.9
16	Terminal inductance phase to phase	mH	1.070	1.070
17	Thermal resistance housing-ambient	K / W	6.8	6.8
18	Thermal resistance winding-housing	K / W	7.4	7.4
19	Thermal time constant windings	s	3.7	3.7
20	Thermal time constant stator	s	16.1	16.1

Specifications

- Axial preload > 5 N
- Max. ball bearing loads
  axial (dynamic) 2.8 N
  radial (7.5 mm from flange) 5.5 N
  Force for press fits (static) 50 N
  (static, shaft supported) 1000 N
- Ambient temperature range -40 ... +100°C
- Max. permissible winding temperature +125°C
- Weight of motor 32 g
- Version with and without Hall sensors
- 8 pole permanent magnet
- 3 phased coil stator with 2 pole shoes each
- Values listed in the table are nominal.
- Connection with Hall sensors / sensorless
  Pin 1: 3.5 ... 20 VDC / Motor winding 1
  Pin 2: Hall sensor 3 / Motor winding 2
  Pin 3: Hall sensor 1 / Motor winding 3
  Pin 4: Hall sensor 2 / neutral point
  Pin 5: GND
  Pin 6: Motor winding 3
  Pin 7: Motor winding 2
  Pin 8: Motor winding 1
- Adapter — Order number / Order number
  see p. 275 — 220300 / 220310
- Connector — Article number / Article number
  AMP — 1-487951-1 / 487951-4
  MOLEX — 52207-1190 / 52207-0490
  MOLEX — 52089-1110 / 52089-0410

  Pin for design with Hall sensors:
  FPC, 11 pole, pitch 1.0 mm, top contact style
- For wiring diagram for Hall sensors, see p. 26

Operating Range

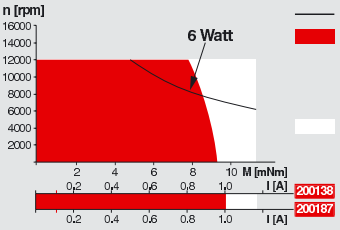

Comments — Details on page 149

Curve of constant assigned power rating

Continuous operation
In observation of above listed thermal resistances (lines 17 and 18) the maximum permissible winding temperature will be reached during continuous operation at 25°C ambient.
= Thermal limit.

Short term operation
The motor may be briefly overloaded (recurring).

Recommended Electronics:

AECS 35/3	page 262
DEC 24/1	263
DEC 50/5	264
DECV 50/5	265
EPOS 24/1	271
Notes	17

April 2005 edition / subject to change

Figure B.2: Maxon EC flat BLDC motor: 6W

FAULHABER

Brushless DC-Servomotors 5,2 mNm

Electronic Commutation

For combination with
Gearheads:
20/1
Encoders:
IE2, 5500, 5540
Drive Electronics:
refer to "Combination Chart", pages 14-15

Series 2036 ... B

		2036 U		012 B	024 B	036 B	048 B	
1	Nominal voltage	U_N		12	24	36	48	Volt
2	Terminal resistance, phase-phase	R		3,4	14,0	26,3	62,2	Ω
3	Output power [1]	$P_{2\,max.}$		20	19	19	18	W
4	Efficiency	$\eta_{max.}$		70	69	70	69	%
5	No-load speed	n_0		17 600	18 000	19 500	17 400	rpm
6	No-load current (with shaft ø 2,0 mm)	I_0		0,102	0,053	0,040	0,025	A
7	Stall torque	M_H		22	21	23	20	mNm
8	Friction torque, static	C_0		0,27	0,27	0,27	0,27	mNm
9	Friction torque, dynamic	C_V		$2{,}14 \cdot 10^{-5}$	$2{,}14 \cdot 10^{-5}$	$2{,}14 \cdot 10^{-5}$	$2{,}14 \cdot 10^{-5}$	mNm/rpm
10	Speed constant	k_n		1 506	773	557	374	rpm/V
11	Back-EMF constant	k_E		0,664	1,294	1,796	2,677	mV/rpm
12	Torque constant	k_M		6,34	12,36	17,15	25,56	mNm/A
13	Current constant	k_I		0,158	0,081	0,058	0,039	A/mNm
14	Slope of n-M curve	$\Delta n/\Delta M$		808	875	854	909	rpm/mNm
15	Terminal inductance, phase-phase	L		148	600	1 160	2 500	µH
16	Mechanical time constant	τ_m		16	18	17	18	ms
17	Rotor inertia	J		1,95	1,95	1,95	1,95	gcm²
18	Angular acceleration	$\alpha_{max.}$		114	107	119	100	$\cdot 10^3$rad/s²
19	Thermal resistance	R_{th1} / R_{th2}	5,7 / 19,9					K/W
20	Thermal time constant	τ_{w1} / τ_{w2}	9 / 577					s
21	Operating temperature range		–30 ... +125					°C
22	Shaft bearings		ball bearings, preloaded					
23	Shaft load max.:							
	– radial at 3 000/20 000 rpm (4,5 mm from mounting flange)		14 / 7					N
	– axial at 3 000/20 000 rpm (push-on only)		8 / 4					N
	– axial at standstill (push-on only)		30					N
24	Shaft play:							
	– radial	≤	0,015					mm
	– axial	=	0					mm
25	Housing material		aluminium, black anodized					
26	Weight		50					g
27	Direction of rotation		electronically reversible					
Recommended values								
28	Speed up to [2]	$n_{e\,max.}$		49 000	49 000	49 000	49 000	rpm
29	Torque up to [1,2]	$M_{e\,max.}$		5,2	4,9	5,0	4,8	mNm
30	Current up to [1,2]	$I_{e\,max.}$		0,98	0,48	0,35	0,23	A

[1] at 36 000 rpm
[2] thermal resistance R_{th2} by 55% reduced

2036 U ... B

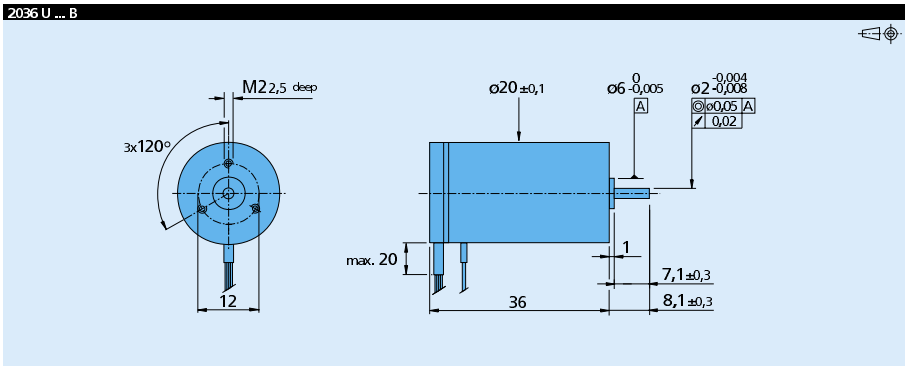

Figure B.3: Faulhaber BLDC motor

EC 32 flat ∅32 mm, brushless, 15 Watt

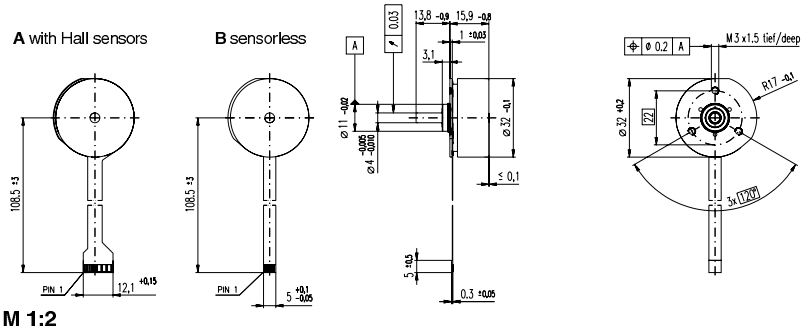

Stock program
Standard program
Special program (on request)

			Order Number	
		with Hall sensors	267121	
		sensorless		226006
Motor Data				
	Values at nominal voltage			
1	Nominal voltage	V	24.0	24.0
2	No load speed	rpm	4390	4390
3	No load current	mA	73.4	73.4
4	Nominal speed	rpm	2740	2740
5	Nominal torque (max. continuous torque)	mNm	24.2	24.2
6	Nominal current (max. continuous current)	A	0.506	0.506
7	Stall torque	mNm	85.8	85.8
8	Starting current	A	1.75	1.75
9	Max. efficiency	%	64	64
	Characteristics			
10	Terminal resistance phase to phase	Ω	13.7	13.7
11	Terminal inductance phase to phase	mH	7.73	7.73
12	Torque constant	mNm / A	49.0	49.0
13	Speed constant	rpm / V	195	195
14	Speed / torque gradient	rpm / mNm	54.5	54.5
15	Mechanical time constant	ms	20.0	20.0
16	Rotor inertia	gcm²	35.0	35.0

Specifications

	Thermal data	
17	Thermal resistance housing-ambient	9.74 K / W
18	Thermal resistance winding-housing	4.63 K / W
19	Thermal time constant windings	8.1 s
20	Thermal time constant motor	108 s
21	Ambient temperature	-40 ... +100°C
22	Max. permissible winding temperature	+125°C
	Mechanical data (preloaded ball bearings)	
23	Max. permissible speed	10000 rpm
24	Axial play at axial load < 5.0 N	0 mm
	> 5.0 N	0.14 mm
25	Radial play	preloaded
26	Max. axial load (dynamic)	4.8 N
27	Max. force for press fits (static)	50 N
	(static, shaft supported)	1000 N
28	Max. radial loading, 7.5 mm from flange	5.5 N
	Other specifications	
29	Number of pole pairs	4
30	Number of phases	3
31	Weight of motor	46 g

Values listed in the table are nominal.

Connection	with Hall sensors	sensorless
Pin 1	3.5 ... 20 VDC	Motor winding 1
Pin 2	Hall sensor 3	Motor winding 2
Pin 3	Hall sensor 1	Motor winding 3
Pin 4	Hall sensor 2	Y neutral point
Pin 5	GND	
Pin 6	Motor winding 3	
Pin 7	Motor winding 2	
Pin 8	Motor winding 1	
Adapter	**Order number**	**Order number**
see p. 283	220300	220310
Connector	**Article number**	**Article number**
AMP	1-487951-1	487951-4
MOLEX	52207-1190	52207-0490
MOLEX	52089-1110	52089-0410

Pin for design with Hall sensors:
FPC, 11-pole, pitch 1.0 mm, top contact style
Wiring diagram for Hall sensors see p. 26

Operating Range

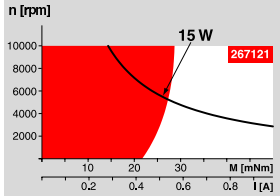

Comments

Continuous operation
In observation of above listed thermal resistance (lines 17 and 18) the maximum permissible winding temperature will be reached during continuous operation at 25°C ambient.
= Thermal limit.

Short term operation
The motor may be briefly overloaded (recurring).

Assigned power rating

Recommended Electronics:

AECS 35/3	page 270
DEC 24/1	270
DEC 50/5	271
DECV 50/5	271
EPOS 24/1	278
Notes	17

Figure B.4: Maxon EC flat BLDC motor: 15W

Appendix C

Rate sensor verification results

The test results which were used to verify the results shown in section 6.5 will be given in this section. Two test results sets were used to verify the results in section 6.5. They will be referred to as rate sensor result set 2 and 3 in this section. It can be seen that the variance of the data in result set 1 is larger that the variance in result set 2. This is due to the fact that the temperature variations during the recording of the data in result set 2 was larger than the temperature variations in result set 3. Both result sets 2 and 3 verify the results in section 6.5 successfully.

C.0.1 Rate sensor result set 2

The covariance matrix of the rate sensor outputs (of result set 2) is shown in equation (C.0.1) (with units of 1×10^{-5} rad^2/s^2).

$$\mathbf{R} = \begin{bmatrix} 0.806 & -0.017 & -0.003 & 0.001 & 0.002 & -0.014 \\ -0.017 & 1.165 & 0.005 & -0.013 & 0.011 & 0.044 \\ -0.003 & 0.005 & 0.885 & -0.004 & 0.003 & 0.008 \\ 0.001 & -0.013 & -0.004 & 2.674 & -0.001 & -0.011 \\ 0.002 & 0.011 & 0.003 & -0.001 & 0.766 & 0.007 \\ -0.014 & 0.044 & 0.008 & -0.011 & 0.007 & 1.029 \end{bmatrix} \tag{C.0.1}$$

The covariance matrix of the derivative taken of the filtered rate sensor outputs of result set 2 (with units of 1×10^{-11} rad^2/s^4) is shown in equation (C.0.2).

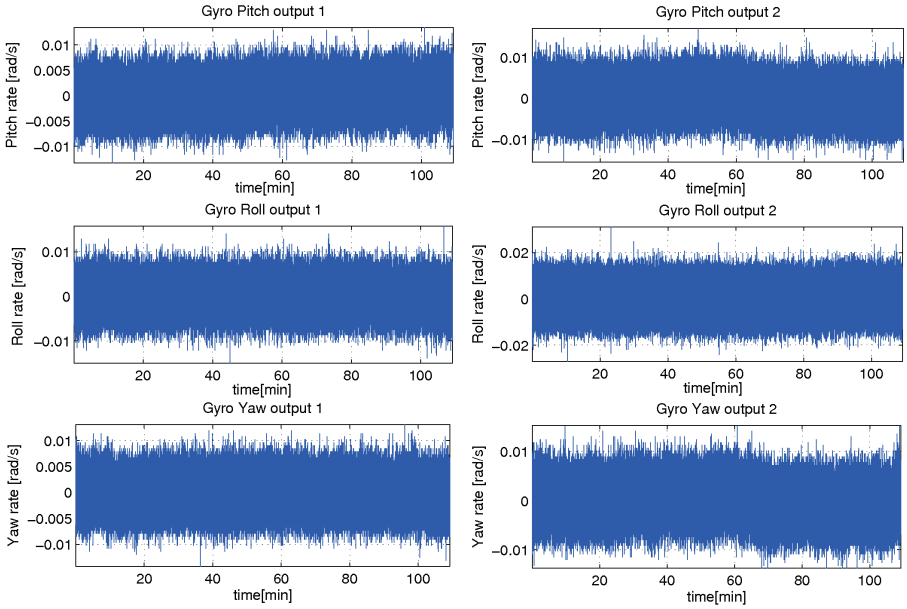

Figure C.1: Rate Sensor outputs over 2 hours (Result set 2)

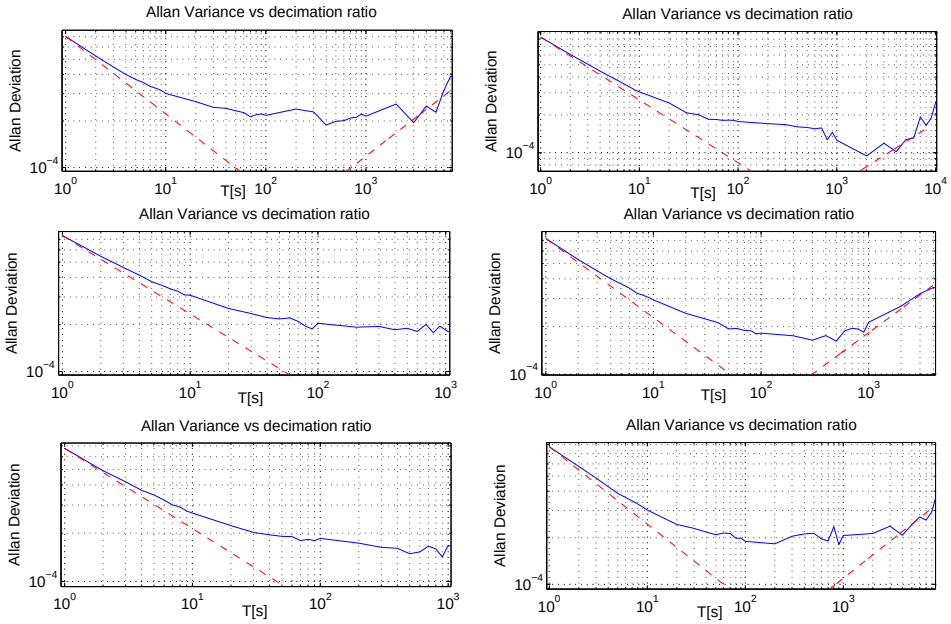

Figure C.2: Allan Variance of the rate sensor outputs (Result set 2)

Table C.1: Angle Random Walk and Rate Random Walk values for the rate sensors (Result set 2)

Rate Sensor	**ARW** $\left(1 \times 10^{-4}\, rad/s/\sqrt{Hz}\right)$	**RRW** $\left(1 \times 10^{-5}\, rad/s^2/\sqrt{Hz}\right)$
Roll 1:	7.03	0.65
Roll 2:	8.32	0.3
Pitch 1:	7.39	-
Pitch 2:	7.19	1
Yaw 1:	6.76	-
Yaw 2:	7.75	0.6

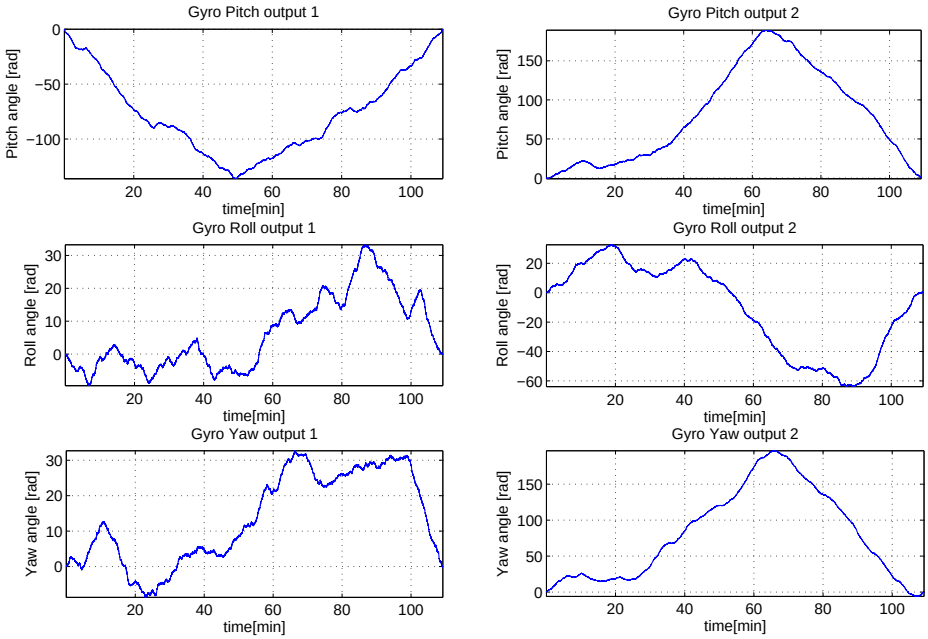

Figure C.3: Integrated rate sensor outputs (Result set 2)

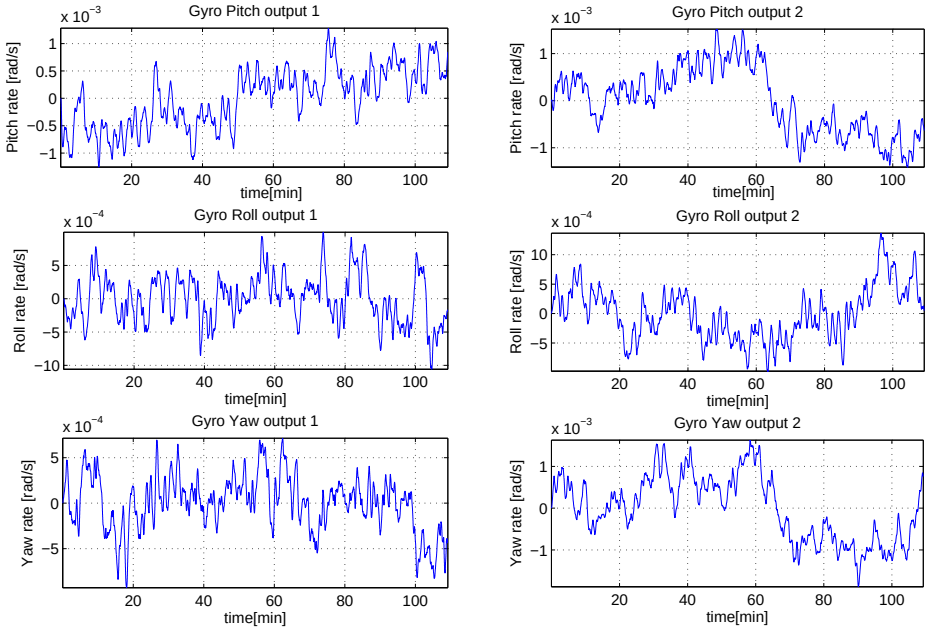

Figure C.4: Filtered rate sensor outputs - cut off frequency 0.01 Hz (Result set 2)

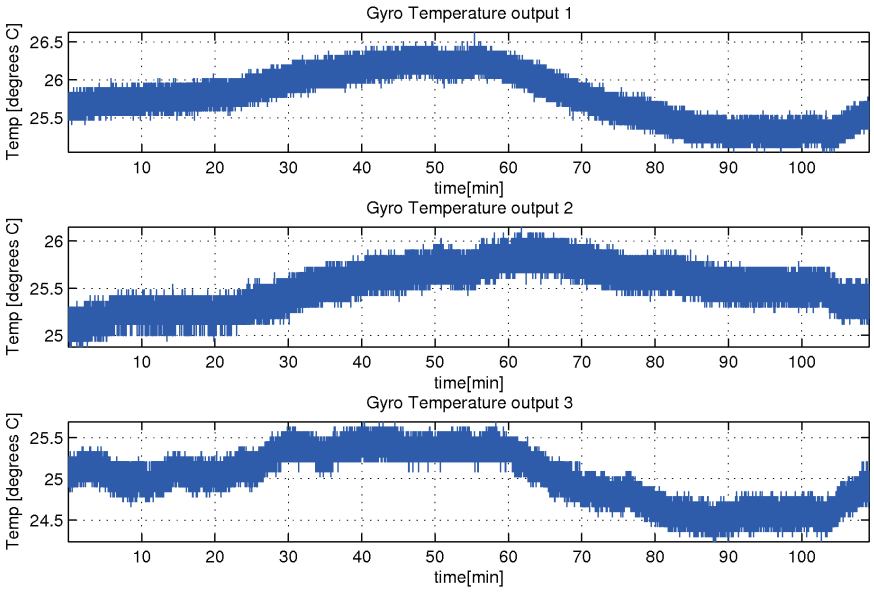

Figure C.5: Temperature outputs of rate sensors (Result set 2)

$$\mathbf{Q} = \begin{bmatrix} 0.1348 & -0.0074 & -0.0046 & 0.0081 & 0.0088 & -0.0032 \\ -0.0074 & 0.1115 & -0.0005 & -0.0024 & 0.0106 & 0.0004 \\ -0.0046 & -0.0005 & 0.1305 & 0.0027 & -0.0003 & 0.0060 \\ 0.0081 & -0.0024 & 0.0027 & 0.1026 & -0.0020 & -0.0052 \\ 0.0088 & 0.0106 & -0.0003 & -0.0020 & 0.0961 & 0.0050 \\ -0.0032 & 0.0004 & 0.0060 & -0.0052 & 0.0050 & 0.1285 \end{bmatrix} \quad \text{(C.0.2)}$$

C.0.2 Rate sensor result set 3

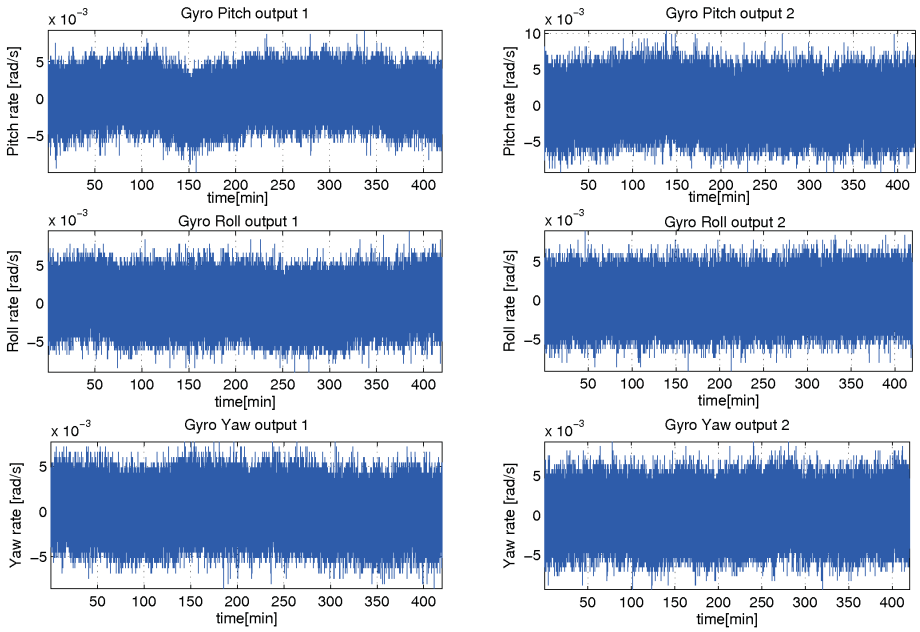

Figure C.6: Rate Sensor outputs over 7 hours (Result set 3)

The covariance matrix of the rate sensor outputs (of result set 3) is shown in equation (C.0.3) (with units of 1×10^{-5} rad^2/s^2).

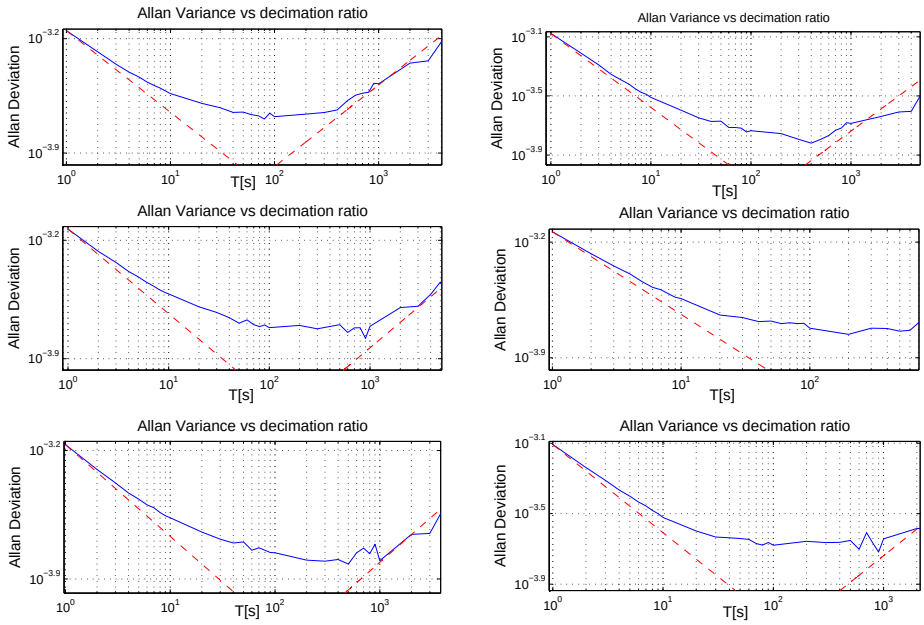

Figure C.7: Allan Variance of the rate sensor outputs (Result set 3)

Table C.2: Angle Random Walk and Rate Random Walk values for the rate sensors (Result set 3)

Rate Sensor	**ARW** $\left(1 \times 10^{-4}\, rad/s/\sqrt{Hz}\right)$	**RRW** $\left(1 \times 10^{-5}\, rad/s^2/\sqrt{Hz}\right)$
Roll 1:	7.07	1.8
Roll 2:	8.36	1
Pitch 1:	7.35	0.8
Pitch 2:	7.29	-
Yaw 1:	6.79	0.85
Yaw 2:	7.8	1

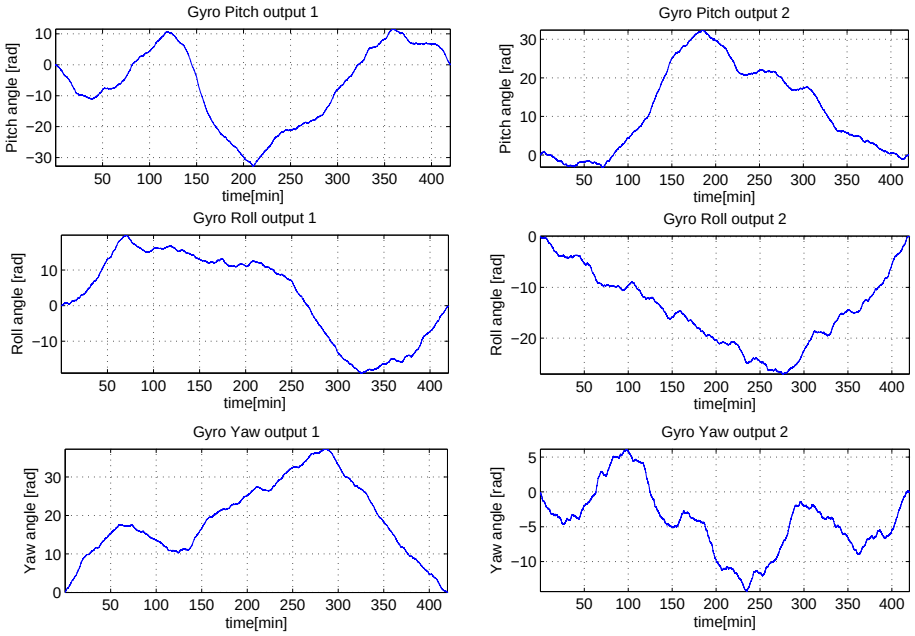

Figure C.8: Integrated rate sensor outputs (Result set 3)

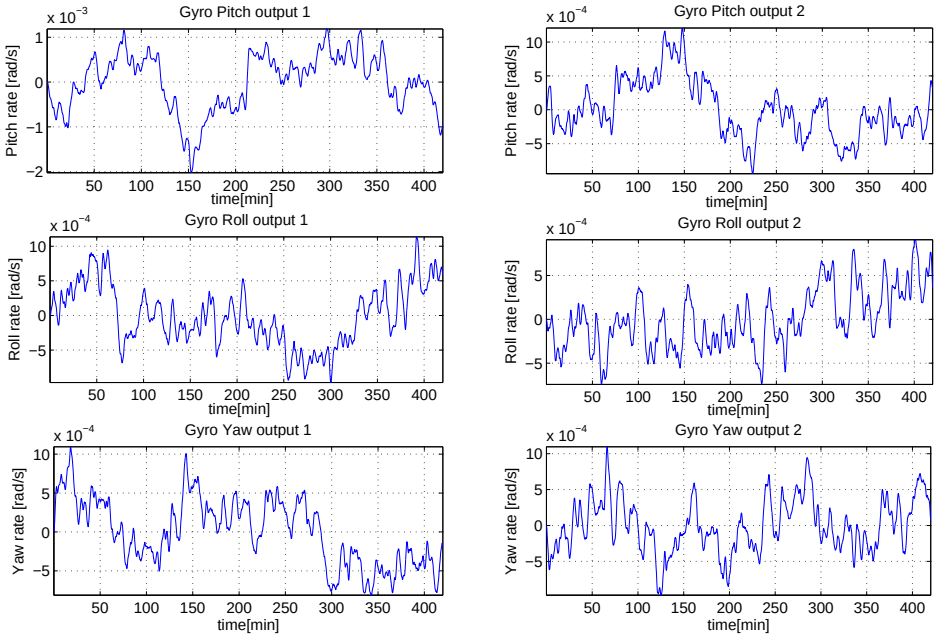

Figure C.9: Filtered rate sensor outputs - cut off frequency 0.002 Hz (Result set 3)

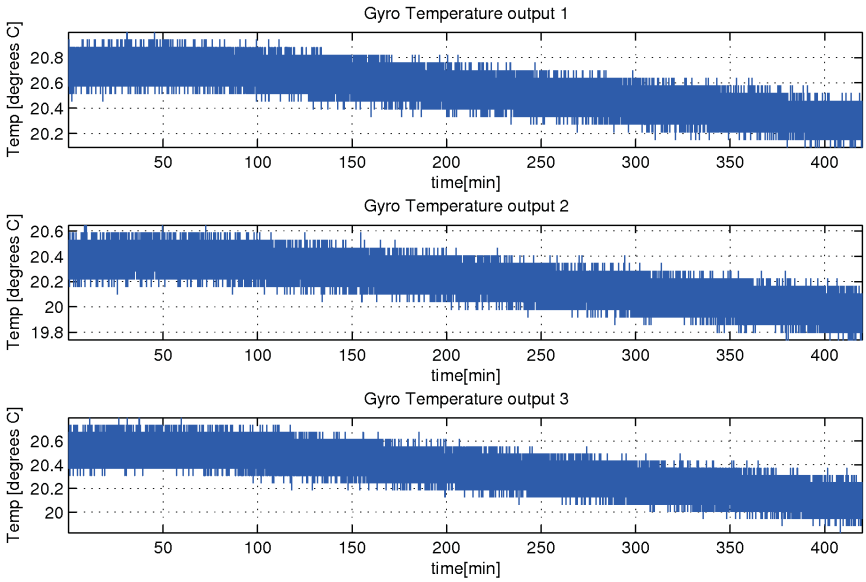

Figure C.10: Temperature outputs of rate sensors (Result set 3)

$$\mathbf{R} = \begin{bmatrix} 0.4006 & -0.0116 & -0.0063 & 0.0024 & -0.0135 & 0.0036 \\ -0.0116 & 0.5476 & -0.0011 & -0.0016 & 0.0032 & -0.0028 \\ -0.0063 & -0.0011 & 0.4223 & 0.0011 & 0.0000 & 0.0014 \\ 0.0024 & -0.0016 & 0.0011 & 0.4006 & -0.0069 & 0.0020 \\ -0.0135 & 0.0032 & 0.0000 & -0.0069 & 0.3556 & -0.0016 \\ 0.0036 & -0.0028 & 0.0014 & 0.0020 & -0.0016 & 0.4655 \end{bmatrix} \tag{C.0.3}$$

The covariance matrix of the derivative taken of the filtered rate sensor outputs of result set 3 (with units of 1×10^{-11} rad^2/s^4) is shown in equation (C.0.4).

$$\mathbf{Q} = \begin{bmatrix} 0.4088 & -0.0096 & 0.0019 & -0.0044 & -0.0369 & 0.0105 \\ -0.0096 & 0.2820 & 0.0287 & 0.0069 & 0.0119 & -0.0043 \\ 0.0019 & 0.0287 & 0.3434 & -0.0065 & 0.0299 & 0.0275 \\ -0.0044 & 0.0069 & -0.0065 & 0.3209 & -0.0036 & -0.0120 \\ -0.0369 & 0.0119 & 0.0299 & -0.0036 & 0.2563 & -0.0516 \\ 0.0105 & -0.0043 & 0.0275 & -0.0120 & -0.0156 & 0.4093 \end{bmatrix} \tag{C.0.4}$$

Appendix D

Moment of inertia determination method

This chapter explaines the string suspension method used to determination the moment of inertia of each reaction wheel rotor, as explained by Peddle [11]. The representation of the setup is given in Figure D.1. Equation (D.0.1) shows the formula for the moment of inertia determination. Table D.1 shows the measured periods of oscillation after the setup was given an initial offset position.

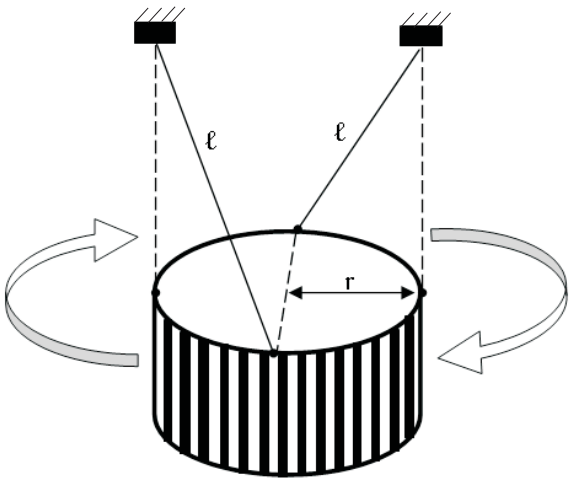

Figure D.1: The string suspension method for moment of inertia determination

Table D.1: Periods of oscillation measured for the reaction wheel rotor

Measured values for 10 periods of oscillation:										
τ [s]	20.77	21.65	21.19	21.52	21.77	21.92	20.99	22	21.66	21.78
Mean period of oscillation [s] : 2.15 s										

$$I = \frac{mgr^2}{4\pi^2 l}\tau^2 \tag{D.0.1}$$

Where,

$$\begin{aligned} I &= 47.08 \times 10^{-6} \\ &= \text{Moment of inertia of the rotor} \\ m &= 85.19\, g \\ &= \text{Mass of each rotor} \\ g &= 9.81\, m/s^2 \\ &= \text{Gravitational acceleration} \\ r &= 25\, mm \\ &= \text{Radius of the rotor} \\ l &= 1.2\, m \\ &= \text{Length of the suspension string} \\ \tau &= 2.15\, s \\ &= \text{Period of oscillation (see Table D.1)} \end{aligned}$$

constraint:

$$l \gg r$$

Bibliography

[1] Baker, E.A. 2006. *The Design of a CMOS Sensor Camera for Space Applications*. Thesis (MScEng). University of Stellenbosch.

[2] Bayard, D.S. et al. 2005. *High Accuracy Inertial Sensors from Inexpensive Components*. United States Patent. California Institute of Technology.

[3] Bijker, J. 2006. *Development of an Attitude Heading Reference System for an Airship*. Thesis (MScEng). University of Stellenbosch.

[4] Bootsma, R. 1997. *Kragstelselondersoek vir die Sunsat Mikrosatelliet*. Thesis (MScEng). University of Stellenbosch.

[5] Chen, X., Steyn, W.H., Hashida, Y. 2000. *Ground-Target Tracking Control of Earth-Pointing Satellites*. AAIA Guidance, Navigation and Control Conference and Exhibit. Surrey Space Centre, University of Surrey, Guildford, UK.

[6] Cropp, A., Collingwood, C. 2006. *The Characterization and Testing of MEMS Gyros for GIOVE-A*. AAIA Guidance, Navigation and Control Conference and Exhibit. Surrey Satellite Technology Ltd, Guildford, UK.

[7] Dussy, S., Durrant, D., Moy, T. 2005. *MEMS gyro for space applications Overview of European activities*. AAIA Guidance, Navigation and Control Conference and Exhibit. August 2005, San Francisco, California, USA.

[8] Greyling, B.C. 1995. *A Charge Coupled Device Star Sensor System for a Low Earth Orbit Microsatellite*. Thesis (MScEng). University of Stellenbosch.

[9] Hou, H. 2004. *Modeling Inertial Sensor Errors Using Allan Variance*. Thesis (MScEng). University of Calgary.

[10] Ntsimane, M.H. 2001. *The Attitude Determination and Control Systems Task Scheduler*. Thesis (MScEng). University of Stellenbosch.

[11] Peddle, I.K. 2005. *Autonomous flight of a model aircraft*. Thesis (MScEng). University of Stellenbosch.

[12] Prezzavento, A.M. 2002. *3-Axis Micro Gyroscope Feasibility Study*. Final Report. Astrium LTD, Stevenage, Herts, England.

[13] Sidi, M.J. 2000. *Spacecraft dynamics and control : a practical engineering approach*. Cambridge University Press.

[14] Stockwell, W. 2003. *Angle Random Walk*. Application note. Crossbow Technology Inc.

[15] Stockwell, W. 2003. *Bias Stability Measurement: Allan Variance*. Application note. Crossbow Technology Inc.

[16] Wertz, J.R. 1999. *Space Mission Analysis and Design*. Space Technology Library.

[17] Steyn, W.H. 1995. *A Multi-mode Attitude Determination and Control System for Small Satellites*. Thesis (PhDEng). University of Stellenbosch.

[18] Wie, B., Weiss, H., Arapostathis, A. 1989. *Quaternion Feedback Regulator for Spacecraft Eigenaxis Rotations*. Journal of Guidance Control and Dynamics, Vol. 12, May-June 1989, pp. 375-379, University of Texas at Austin, Austin, Texas, USA.

[19] Wie, B., Bailey, D., Heiberg, C. 2002. *Rapid Multitarget Acquisition and Pointing Control of Agile Spacecraft*. Journal of Guidance Control and Dynamics, Vol. 25, January-February

2002, pp. 96-104, Arizona State University, Tempe, Arizona, USA.